

**CHAIN EXCHANGE IN AQUEOUS SOLUTIONS OF  
BLOCK POLYMER MICELLES**

by

Ryan P. Murphy

A thesis submitted to the Faculty of the University of Delaware in partial fulfillment of the requirements for the degree of Master of Chemical Engineering

Summer 2014

© 2014 Ryan Murphy  
All Rights Reserved

**CHAIN EXCHANGE IN AQUEOUS SOLUTIONS OF  
BLOCK POLYMER MICELLES**

by

Ryan P. Murphy

Approved: \_\_\_\_\_  
Thomas H. Epps, III, Ph.D.  
Professor in charge of thesis on behalf of the Advisory Committee

Approved: \_\_\_\_\_  
Millicent O. Sullivan, Ph.D.  
Professor in charge of thesis on behalf of the Advisory Committee

Approved: \_\_\_\_\_  
Abraham M. Lenhoff, Ph.D.  
Chair of the Department of Chemical and Biomolecular Engineering

Approved: \_\_\_\_\_  
Babatunde A. Ogunnaike, Ph.D.  
Dean of the College of Engineering

Approved: \_\_\_\_\_  
James G. Richards, Ph.D.  
Vice Provost for Graduate and Professional Education

## ACKNOWLEDGMENTS

This work simply would not have been possible without the support, guidance, curiosity, and insight from several other individuals and collaborations. First and foremost, I thank my advisors for providing their expertise, guidance, and support. I also wish to thank Liz Kelley and Jon Seppala for providing their insight, expertise, training, and inspiration. Paul Butler, Yun Liu, Matthew Wasbrough, and Katie Weigandt kindly offered their expertise and assistance on neutron scattering experiments, as well as engaged in several scientific discussions. Simon Rogers and Colin Cwalina sparked insightful discussions regarding colloidal suspensions and rheology, as well as offered assistance with instrument training and usage. I gratefully acknowledge Chaoying Ni, Frank Kriss, Fei Deng, and Jennifer Sloppy for their assistance and training with transmission electron microscopy. Also, I would like to thank Connor Hodges for his assistance with light scattering experiments. Finally, I thank my parents, brother, extended family, and close friends for all of their support, perspective, and cheerful disposition.

*For Bill Murphy and Jack Crowley*

## TABLE OF CONTENTS

LIST OF TABLES .....	viii
LIST OF FIGURES .....	ix
ABSTRACT .....	xxi

### Chapter

1	INTRODUCTION .....	1
1.1	Block Polymer Solution Assembly .....	4
1.2	Applications of Block Polymer Micelles .....	8
1.3	Chain Exchange Mechanisms .....	10
1.3.1	Single chain exchange .....	11
1.3.2	Micelle fusion and fission .....	13
1.3.3	Shear-induced flocculation .....	14
1.3.4	Interfacial nucleation .....	15
1.4	Experimental Evidence for Micelle Chain Exchange .....	16
1.5	Processing Conditions .....	18
1.6	Thesis Overview .....	20
	REFERENCES .....	22
2	EXPERIMENTAL METHODS .....	27
2.1	Material Properties .....	28
2.2	Solution Preparation .....	31
2.2.1	Controlling cosolvent addition and removal .....	31
2.2.2	Polymer concentration after dialysis .....	33
2.2.3	Contrast-matched polymer solutions for SANS .....	35
2.2.4	Pre-mixed and post-mixed micelle solutions for SANS .....	36
2.3	Complementary Solution Characterization Methods .....	40
2.3.1	Dynamic light scattering (DLS) .....	41
2.3.2	Cryogenic transmission electron microscopy (cryo-TEM) .....	46
2.3.3	Small angle neutron scattering (SANS) .....	57

2.3.4	Flow small angle neutron scattering (flow-SANS) .....	61
2.4	Solution Environment.....	64
2.4.1	Temperature control .....	64
2.4.2	Common mixing methods .....	65
2.4.3	Controlled flow conditions .....	67
	REFERENCES .....	68
3	BLOCK POLYMER MICELLE SIZE EVOLUTION.....	71
3.1	Introduction .....	71
3.2	Consequences of Cosolvent Removal .....	73
3.2.1	Dependence of solution agitation .....	75
3.2.2	Varying initial THF/water content .....	77
3.3	Probing Chain Exchange Mechanisms.....	79
3.3.1	Micelle fusion/fission and single chain exchange .....	80
3.3.2	Chain exchange near equilibrium size.....	81
3.3.3	Bimodal size distribution from cryo-TEM .....	83
3.3.4	Concentration dependence.....	87
3.3.5	Fitting DLS autocorrelation functions.....	92
3.4	Shear-Induced Interfacial Nucleation.....	99
3.5	Chapter Summary.....	101
	REFERENCES .....	102
4	EFFECTS OF MOLECULAR WEIGHT AND TEMPERATURE.....	106
4.1	Introduction .....	106
4.2	Slow Micelle Relaxation Kinetics.....	109
4.2.1	Experimental design .....	109
4.2.2	Core and corona molecular weight dependence .....	111
4.2.3	Temperature dependence.....	118
4.2.4	Morphological transition and aggregation.....	122
4.3	Fast Micelle Relaxation Kinetics .....	124
4.4	Chapter Summary.....	128
	REFERENCES .....	130

5	MICELLE CHAIN EXCHANGE INDUCED BY FLOW .....	132
5.1	Introduction .....	132
5.2	Shear and Interfacial Effects on Chain Exchange .....	134
5.2.1	Cone-plate flow .....	134
5.2.2	Couette flow .....	136
5.2.3	Nitrogen gas sparging.....	140
5.2.4	Rapid vortex mixing.....	141
5.3	Fast Chain Exchange for Rapid Vortex Mixing.....	144
5.3.1	Quantifying micelle chain exchange .....	146
5.3.2	Concentration dependence.....	146
5.3.3	Surface-limited chain exchange kinetics.....	148
5.4	Relevance to Other Amphiphilic Systems and Applications .....	151
5.5	Chapter Summary.....	152
	REFERENCES .....	154
6	CONCLUSIONS AND FUTURE RECOMMENDATIONS .....	157
6.1	Thesis Summary .....	157
6.2	Future Recommendations.....	160
	REFERENCES .....	164
Appendix		
A	SUPPLEMENTARY DATA.....	165
B	ARTIFACTS IN CRYO-TEM .....	175
B.1	Ice Thickness and Size Gradients.....	175
B.2	Particle Packing and Alignment .....	178
B.3	Sample Contamination .....	181
B.4	Sample and Background Degradation.....	182
B.5	Blotting Effects.....	184
C	PERMISSION STATEMENTS .....	185

## LIST OF TABLES

Table 2.1. Block polymer properties and notations. Number average molecular weight ( $M_n$ ), degree of polymerization (N), and dispersity ( $\mathcal{D}$ ) are given for each block polymer used in subsequent experiments. ....	30
Table 2.2. Polymer concentration determined pre- and post-dialysis to pure H <sub>2</sub> O or D <sub>2</sub> O using calibration curves.....	34

## LIST OF FIGURES

- Figure 1.1. Small molecule and macromolecular amphiphiles are found in (a) biological membranes and applications in protein separation, (b) drug delivery vehicles, (c) dispersants and detergents, and (d) aqueous nanoreactors. Chain exchange dynamics play a key role in the surfactant functionality and are typically much faster for small molecule surfactants in comparison to macromolecular surfactants. .... 2
- Figure 1.2. Direct dissolution of PB-PEO in water leads to spontaneous self-assembly of a core-shell sphere with diameters  $\sim 35\text{-}70$  nm in this particular work. The hydrophobic PB core is sterically stabilized and surrounded by a PEO corona or shell. Free energy minimizing dictates aggregation number, morphology, and micelle size, which can be manipulated by block molecular weight or the core-solvent interfacial tension by THF cosolvent addition. Subsequent cosolvent removal *via* dialysis leaves the metastable micelle structure kinetically-frozen in water under quiescent conditions. .... 5
- Figure 1.3. Mechanisms for micelle chain exchange include (a) single chain exchange and (b) micelle fusion/fission that can occur due to diffusive or Brownian motion. With addition of shear flow or hydrophobic-hydrophilic interfaces, other proposed mechanisms for micelle chain exchange may include (c) shear-induced flocculation and (d) interfacial nucleation. .... 11
- Figure 2.1. Experimental topics of (2.1) materials, (2.2) solution preparation, (2.3) complementary solution characterization methods, and (2.4) solution environment are discussed. Material properties, solution preparation, and solution processing environments are important parameters that affect block polymer micelle size, structure, and chain dynamics in solution. Complementary *in situ* methods are required to properly characterize micelle solutions and to provide insight into dynamic processes. .... 28
- Figure 2.2. UV-Vis calibration curve to determine polymer concentration after dialysis. (a)  $B_{59}O_{180}$  in  $H_2O$  (b) Blend of 88 wt%  $B_{59}dO_{163}$  / 12 wt%  $B_{59}O_{180}$  in  $D_2O$ . Figure reproduced in part with permission from *Nature Communications*, 5, 3599 (2014).<sup>10</sup> .... 34

Figure 2.3. Contrast-matching for neutron scattering experiments. An equal volume mixture of PB- <i>h</i> P EO micelles and PB- <i>d</i> P EO micelles will have decreased scattering contrast after chains are exchange between micelles. If chain exchange occurs, the maximum scattered-intensity condition directly after mixing ( $t = 0$ ) will approach the minimum scattered-intensity condition or randomly mixed condition (pre-mixed or $t = \infty$ ). <i>Macromolecules</i> , 46, 6319-6325 (2013). Figure reproduced in part with permission from <i>Nature Communications</i> , 5, 3599 (2014). <sup>10</sup> .....	37
Figure 2.4. Complementary characterization techniques transition from lowest required time and resources and also lowest level of understanding (DLS) to more time consuming yet insightful techniques (cryo-TEM and SANS).....	40
Figure 2.5. Simplified concept of dynamic light scattering. Smaller particles move faster from diffusive motion, which results in faster fluctuations in scattered light intensity. Larger particles move slower from diffusive motion, giving slower fluctuations in scattered light. These intensity fluctuations can be correlated to effective diffusion coefficients, which can in turn be related to particle hydrodynamic diameter. ....	42
Figure 2.6. Schematic of transmission electron microscope (left, not to scale) and picture of FEI Tecnai G2 twin instrument (right). ....	48
Figure 2.7. Cryo-TEM ice thickness gradients can lead to different particle distributions depending on the particle size. (a) Quick screening methods by visual inspection are critical, as impending sample damage due to incident electrons will occur over time. (b) Thick ice leads to low contrast compared to background or (c) significant micelle overlap. (e) Optimal thickness arises for when the ice thickness is comparable to the particle length scale. (f) Thin ice leads to quick melting or no contained sample.....	50
Figure 2.8. Method to extract volume fraction profiles from cryo-TEM images. Cryo-TEM image of micelles distributed in hyperquenched water (left) and the corresponding averaged radial profile of 50 micelles (right, blue circles). The empirical fit to the experimental profile for a star-like micelle (black line) and hard-sphere (red line) are shown for comparison. Scale bar is 100 nm. Figure reproduced with permission from <i>Macromolecules</i> , 46, 6319-6325 (2013). <sup>22</sup> .....	54

- Figure 2.9. Image analysis method for counting the number of micelles with a given projected area. (a) Initial cryo-TEM image. (b) After despeckle and bandpass filtering. (c) After threshold selection to define particle areas. (d) After outlining particle areas using built in particle area routine using ImageJ. Scale bar is 200 nm. Figure reproduced in part with permission from *Nature Communications*, 5, 3599 (2014).<sup>10</sup> ..... 55
- Figure 2.10. Cross-sectional analysis (left and bottom) for determining particle spacing and particle diameter. The Fourier transform of highly ordered arrays can also be used to determine particle spacing (right). The cryo-TEM image was taken 16 d after dialysis into water for PB-PEO micelles initially at 43 vol% THF and 10 mg mL<sup>-1</sup>. Figure reproduced in part with permission from *Nature Communications*, 5, 3599 (2014).<sup>10</sup> ..... 56
- Figure 2.11. Simplified schematic of small angle neutron scattering (SANS). Incident neutrons either scatter once off of nuclei or transmit directly through the sample to the detector. The scattering pattern and angle of the scattered neutrons are related to the positions and compositions of the atomic nuclei within the sample. The difficulty in data fitting arises from the loss of phase information in the detected intensity..... 58
- Figure 2.12. Definition of the elastic scattering wavevector ( $q$ ) in terms of the initial ( $k_i$ ) and final ( $k_f$ ) wavevectors. The magnitude of the scattered wavevector is given in equation 2.21, which is related to the scattering angle ( $\Theta$ ) and neutron wavelength ( $\lambda$ )..... 59
- Figure 2.13. Flow-SANS is the incorporation of small angle neutron scattering within flowing environments. This method allows nanostructures to be probed in response to shear flow. Incident neutrons scatter from a sample (1-3 shear plane) flowing within concentric cylinders (Couette flow). Select features in the sample structure can be probed under flow using contrast-matching methods discussed previously. .... 63
- Figure 3.1. Effect of solution agitation on micelle size evolution. Magnetic stirring (200 rpm) leads to size evolution of block polymer micelles following cosolvent removal, as shown through an increase in the hydrodynamic radius ( $R_h$ ) following dialysis into water (0 to 120 d). Beginning from the same dialyzed stock solution (B<sub>59</sub>O<sub>180</sub>, 43 vol% THF, 10 mg mL<sup>-1</sup>), one sample was magnetically stirred at 200 rpm, while the control was not stirred (i.e. quiescent). No distinct changes in  $R_h$  were measured up to 120 d post dialysis in the absence of agitation. Variability in the fitted  $R_h$  determined from DLS using the quadratic cumulant fit was between 1 to 3 nm. .... 76

Figure 3.2. Varying initial THF cosolvent content prior to dialysis and subsequent solution agitation. DLS data provided the average hydrodynamic radius ( $R_h$ ) of PB-PEO micelles in water, and showed an increase in $R_h$ over several days for samples at THF contents greater than 10 vol% THF. Fitted $R_h$ values (quadratic cumulant method) varied between 1-3 nm. ....	78
Figure 3.3. Determining chain exchange using SANS contrast-matching methods. The lack of change in scattered intensity for mixed PB- <i>h</i> PEO and PB- <i>d</i> PEO micelles (0 vol% THF) suggested negligible chain exchange occurred after 10 d. Error bars represent the standard deviation. ....	82
Figure 3.4. Progression of micelle growth through a bimodal pathway. Cryo-TEM analysis of PB-PEO micelles (43 vol% pre-dialysis, 10 mg mL <sup>-1</sup> ) in pure water following dialysis and stirring for 21 d. A distinct second distribution appears after 1 day and progresses to a monodispersed larger population near 10 d. Scale bars are 100 nm. ....	84
Figure 3.5. Distribution of micelle core radii from Cryo-TEM image analysis. The core distributions determined from Fig. 3.4 are plotted as relative frequency histograms for 21 d following dialysis to pure water. The primary distribution ( $R_c \sim 5-6$ nm) and secondary distribution ( $R_c \sim 10-11$ ) are distinctly separated by a gap in micelles with intermediate core sizes ( $R_c \sim 8$ nm).....	85
Figure 3.6. Aggregation number distributions determined from core radii shown in Fig. 3.5 (43 vol% THF sample). The initial micelles (day 0) were relatively monodispersed with aggregation numbers of $\sim 100$ . The larger micelles had a broader distribution of aggregation numbers that was centered around $\sim 800$ . ....	86
Figure 3.7. Micelle size evolution as a function of concentration. Cryo-TEM images of PB-PEO (43 vol% pre-dialysis) at different initial concentrations qualitatively suggested that lower concentrations led to slower micelle growth rates. This conclusion was supported by the presence of smaller micelles at day 11 and day 16 for the 2 mg mL <sup>-1</sup> and 5 mg mL <sup>-1</sup> samples, and nearly monodispersed larger micelles at day 10 and day 16 for the 10 mg mL <sup>-1</sup> sample. ....	89

- Figure 3.8. Bimodal distribution and concentration dependence determined from SANS. A bimodal Schulz distribution of spheres provided a better fit to corona-matched PB-PEO micelles compared to a fit using a single broader Schulz distribution. Increasing polymer concentration led to a shift toward larger micelle populations after mixing for 11 d (43 vol% THF prior to dialysis). The bimodal distribution and concentration dependence suggested a fusion/fission chain exchange mechanism. .... 90
- Figure 3.9. DLS data probing the concentration dependence of micelle growth. PB-PEO micelles were prepared at various THF contents (10 wt%, 20 wt%, and 40 wt%) and concentrations (1 mg mL<sup>-1</sup> and 10 mg mL<sup>-1</sup>) prior to dialysis. The DLS experiments were not able to distinguish a concentration dependence as cryo-TEM and SANS suggested. Variability in the fitted  $\langle R_h \rangle$  was within 1-3 nm. .... 92
- Figure 3.10. DLS autocorrelation functions and double exponential fits over 90 d of stirring post-dialysis for PB-PEO micelles in water (40 vol% THF pre-dialysis, 2 mg mL<sup>-1</sup>). The double exponential fit (dashed lines) tended to over-predict data (points) at earlier correlation times and under-predict at later correlation times. .... 94
- Figure 3.11. DLS autocorrelation functions and polydisperse double exponential fit over 90 d of stirring post-dialysis for PB-PEO micelles in water (40 vol% THF pre-dialysis, 2 mg mL<sup>-1</sup>). The polydisperse double exponential function (dashed lines) better fit the experimental data (points) at earlier and later correlation times. .... 95
- Figure 3.12. DLS fitting parameters for PB-PEO micelles 40 vol% THF pre-dialysis. (a) Intensity weighting of larger micelle population as a function of days post dialysis for double exponential and polydisperse double exponential fits. (b) Polydispersity parameters for the quadratic cumulant and polydisperse double exponential fits. (c) Experimental autocorrelation function on day 9 and corresponding fit with polydisperse double exponential. Inset shows fitted  $R_h$  and intensity weight ( $A_2$ ). (d) Corresponding fit to the same data shown in (c) but with different fitted  $R_h$  and  $A_2$ . .... 97
- Figure 3.13. Root mean square error (RMSE) for different DLS fitting methods. The polydisperse double exponential fit gave the best fit overall throughout 90 d (PB-PEO 40 vol% THF pre-dialysis 2 mg mL<sup>-1</sup>) followed by the quadratic cumulant and the double exponential fits. .... 99

Figure 4.1. Experimental design variables. The four main variables investigated were temperature, core and corona molecular weight, and THF content before dialysis to water. Each variable was expected to influence micelle chain exchange and to provide insight into the growth mechanism. The polymer concentration before dialysis ( $10 \text{ mg mL}^{-1}$ ) and solution agitation (magnetic stirring at 200 rpm) were fixed. ....	110
Figure 4.2. Micelle hydrodynamic radius without solution agitation in water following dialysis. Solutions of $B_{81}O_{182}$ (left) and $B_{81}O_{257}$ (right) in various THF/water contents (wt% THF) were dialyzed against pure water to produce kinetically-frozen micelles. In the absence of stirring, micelles did not change size over 80 d at room temperature regardless of the THF content. ....	111
Figure 4.3. Molecular weight and temperature dependence of micelle size evolution. Micelles that were magnetically stirred showed either an increase (40 wt% THF, open symbols) or decrease (0% THF, closed symbols) in hydrodynamic radius over time. Both the molecular weight and temperature led to different characteristic relaxation timescales. ....	113
Figure 4.4. Cryo-TEM images of PB-PEO micelles after dialysis (0% THF, 22 °C) samples. Images of $B_{81}O_{182}$ immediately after dialysis on day 0 (top row) and day 112 (middle row) showed a slight decrease in core size from $R_c \sim 14\text{-}16 \text{ nm}$ to $R_c \sim 12 \text{ nm}$ . For comparison, $B_{81}O_{257}$ showed similar core sizes $R_c \sim 15 \text{ nm}$ on day 0 (bottom row). ....	115
Figure 4.5. Bimodal micelle size evolution following dialysis to water (40% THF, 22°C). Agitated solutions of $B_{59}O_{180}$ (top), $B_{81}O_{182}$ (middle), and $B_{81}O_{257}$ (bottom) showed a bimodal distribution of micelle sizes. $B_{81}O_{182}$ and $B_{81}O_{257}$ showed slower micelle growth based the predominance of smaller micelles on day 27 compared to $B_{59}O_{180}$ on day 21. ....	118
Figure 4.6. Temperature and molecular weight dependence of micelle size evolution. Rearranged presentation of data in Figure 4.3 to highlight the effect of temperature. For 0 wt% THF samples, solutions stirred at higher temperature led to faster size decreases and eventually to polymer precipitation. For 40 wt% THF samples, increasing temperature led to slower micelle growth and eventual precipitation...	120

- Figure 4.7. Morphological transitions during micelle size evolution. Cryo-TEM images of  $B_{81}O_{182}$  prepared at 40 wt% THF and  $10 \text{ mg mL}^{-1}$  prior to dialysis. Aqueous micelle solutions were stirred at  $40^\circ\text{C}$  for 19 d (left) and 51 d (right). Distinctly different morphologies such as cylinders and toroids were observed after 51 d at  $40^\circ\text{C}$ . Morphological changes and subsequent polymer precipitation was likely due to cross-linking of the PB cores accelerated by elevated temperatures and aeration from stirring. .... 123
- Figure 4.8. Micelle growth from rapid vortex mixing. (a) Effective hydrodynamic radius increases as a function of vortex mixing time for  $B_{81}O_{182}$  micelles in water (40 wt% THF before dialysis). The relaxation time scale was significantly lower compared to magnetically stirred solutions, showing a trend of decreasing characteristic time with increasing power input. (b) Fitted polydispersity parameters from the quadratic cumulant method showed an increase and subsequent decrease as a function of vortex mixing time. .... 125
- Figure 4.9. Cryo-TEM images of micelle growth from rapid vortex mixing.  $B_{81}O_{182}$  micelle solutions (40 wt% THF before dialysis to water) were imaged after 60 s of rapid vortex mixing. A bimodal distribution of micelle sizes was observed similarly to magnetically stirred micelle solutions. .... 126
- Figure 4.10. Comparison of timescales and final micelle hydrodynamic radii ( $R_f$ ) for micelle solutions after rapid vortex mixing (red, green, blue) and magnetic stirring (purple, orange, gray). The agitation rate and polymer molecular weight for  $B_{59}O_{180}$  (triangles),  $B_{81}O_{182}$  (circles), and  $B_{81}O_{257}$  (squares) led to distinct relaxation timescales and final radii (left). A dimensionless plot followed an exponential relaxation curve from Eq. 4.1 (right). .... 127
- Figure 5.1. DLS autocorrelation function of  $B_{81}O_{182}$  micelle solutions (40 wt% THF pre-dialysis) after shear flow in a cone-plate rheometer. An increase in micelle size after 5 min of shear (shift to larger correlation time) suggested that micelle size evolution could be accelerated with increasing shear rate. .... 136

- Figure 5.2. Flow-SANS results for corona-matched blended PB-*h*PEO/PB-*d*PEO micelles (40 wt% THF pre-dialysis). Scattered intensity from micelle cores did not change significantly under flow (a) or after stopping flow after 60 min at high shear rates (b). The lack of particle interactions or structure factor suggested flocculation and aggregation was not occurring. Furthermore, no changes in micelle core size suggested sufficient air-water interface was necessary for chain exchange. The error bars represent the standard deviation. .... 138
- Figure 5.3. SANS experiment to quantify chain exchange due to Couette flow. The lack of decrease in intensity suggested negligible chain exchange occurred after flowing for 90 min at  $5000 \text{ s}^{-1}$ . The 0 min sample and pre-mixed sample are averaged scattering intensities of three micelle concentrations. The error bars represent the standard deviation. .... 139
- Figure 5.4. SANS experiment to quantify chain exchange due to gas sparging. The lack of decrease in intensity suggested negligible chain exchange occurred after 60 min mixing by nitrogen gas sparging. The 0 min sample and pre-mixed sample are averaged scattering intensities of three micelle concentrations. The error bars represent the standard deviation. .... 140
- Figure 5.5. SANS experiment to quantify chain exchange due rapid vortex mixing. The decrease in intensity over minutes demonstrated that rapid vortex mixing could lead to chain exchange between micelles ( $B_{59}O_{180}$  and  $B_{59}dO_{163}$  in  $D_2O/H_2O$ ,  $2.4 \text{ mg mL}^{-1}$ ). The fraction of chains exchanged could be quantified according to Eq. 5.1. The 0 min sample and pre-mixed sample are averaged scattering intensities of three micelle concentrations. The error bars represent the standard deviation. .... 142
- Figure 5.6. (a) Effect of air headspace on chain exchange due to rapid vortex mixing. Solution volumes of 1 mL and 4 mL were vortex mixed for 15 min in the same vial size. The solution with less possible air-water contact area per unit volume (4 mL solution) was significantly slower than the solution with more air headspace (1 mL solution). (b) The spherical form factor of PB cores did not change significantly as a result of rapid vortex mixing, further validating the use of Eq. 5.1 to quantify chain exchange. .... 145

Figure 5.7. SANS concentration series to determine micelle chain exchange kinetics after rapid vortex mixing in solutions at (a) 5.0 mg mL <sup>-1</sup> , (b) 7.5 mg mL <sup>-1</sup> , (c) 10.0 mg mL <sup>-1</sup> , and (d) 15.0 mg mL <sup>-1</sup> . The 0 min sample and pre-mixed sample are averaged scattering intensities of three micelle concentrations. The error bars represent the standard deviation. ....	147
Figure 5.8. Quantification of micelle chain exchange kinetics. (a) The fraction of chains exchanged and (b) concentration of chains exchanged as a function of mix time. The linear kinetics suggested a surface-limited exchange process. Increasing concentration also led to a decrease in the apparent zero-order rate constants and deviations from linearity. The error bars for R(t <sub>mix</sub> ) and mixed chain concentration were propagated based on the uncertainty in polymer concentration. ....	149
Figure A.1. Polymer concentration and UV-Vis absorbance data for B <sub>59</sub> O <sub>180</sub> in H <sub>2</sub> O (left) and 88 wt% B <sub>59</sub> dO <sub>163</sub> / 12 wt% B <sub>59</sub> O <sub>180</sub> in D <sub>2</sub> O (right) used in the calibration curves shown in Figure 2.2. ....	165
Figure A.2. Q-ranges for SANS sample-to-detector distances at 1 m (green), 4 m (blue), and 13.5 m (violet) produced using SASCALC package in Igor Pro. Neutron wavelength was 6 Å. Scattered intensity for the three overlaid curves (black) show good overlap throughout ~0.003 Å <sup>-1</sup> to ~0.4 Å <sup>-1</sup> .....	166
Figure A.3. SANS data showing negligible chain exchange in H <sub>2</sub> O/D <sub>2</sub> O under quiescent conditions. Negligible chain exchange occurred between PB- <i>h</i> PEO and PB- <i>d</i> PEO micelles up to 19 d (gray circles), as demonstrated by the overlap with the scattering curve immediately after combining equal solution volumes of pure PB- <i>h</i> PEO micelles and pure PB- <i>d</i> PEO micelles (open squares). The scattering curve for micelles containing randomly mixed PB- <i>h</i> PEO and PB- <i>d</i> PEO chains is shown for comparison (black circles). ....	167

- Figure A.4. (a) Image of PS-PEO solutions [ $M_n$  PS = 12.5 kg mol<sup>-1</sup>,  $M_n$  PEO = 35.6 kg mol<sup>-1</sup> PEO, 74 wt% PEO,  $\bar{D} = 1.08$ ] prepared in water/THF mixtures (10 wt% THF, 5 mg mL<sup>-1</sup>). The order in which the solvent was added to the dry polymer made a significant difference in the resulting solution assembly. Adding THF solvent first and then adding water (or adding the THF/water mixture together to the dry polymer) produced a clear micelle solution. Meanwhile, adding water first and then adding THF produced a cloudy solution. (b) DLS data for PS-PEO solutions prepared at various THF compositions (adding THF first and then adding water) prior to dialysis. Solutions were dialyzed into pure water for 24 h to remove THF cosolvent and then were measured using DLS after magnetic stirring at 200 rpm. Hydrodynamic diameters  $D_h$  and polydispersity parameters  $Poly$  were fit using the quadratic cumulant method. For each solution, a significant increase in  $D_h$  was found 2 d post-dialysis. All data was collected by Connor Hodges. .... 168
- Figure A.5. <sup>1</sup>H NMR data of PB-PEO micelle solutions in THF/water mixtures (a) prior to dialysis and (b) after 24 h dialysis to pure water. The disappearance of THF solvent peaks at ~3.6 ppm and ~1.75 ppm confirmed removal of THF cosolvent (60 wt% THF) after 24 h of dialysis to water. Samples of solutions were in deuterated DMSO for <sup>1</sup>H NMR analysis. Data were collected and analyzed by Dr. Tom Smart. .... 169
- Figure A.6. Comparing the SANS data fits using monomodal (left column) and bimodal (right column) Schulz spheres at initial polymer concentrations of (a) 2 mg mL<sup>-1</sup>, (b) 5 mg mL<sup>-1</sup>, and (c) 10 mg mL<sup>-1</sup> (see Figure 3.8). The bimodal core radii distribution consistently provided a better fit (black lines) to the experimental data (points). Insets show the number distribution of core radii. Figure reproduced with permission from *Nature Communications*, 5, 3599 (2014). .... 170
- Figure A.7. Estimated intensity-weighted hydrodynamic diameters  $D_h$  for a bimodal mixture of spherical particles with diameters of (a) 30 nm and 70 nm, or (b) 30 nm and 50 nm. The x-axis represents the fraction of larger particles based on (blue) number fraction, (red) volume fraction, and (green) intensity fraction. The significant increase in the intensity-weighted  $D_h$  is demonstrated with only a relatively small increase in number fraction of larger particles (< 0.1). .... 171

Figure A.8. SANS data (points) and fits (black lines) for PB-PEO micelles in D <sub>2</sub> O. (a) The core-shell sphere fit to B <sub>81</sub> O <sub>182</sub> micelles gave R <sub>c</sub> ~ 14 and R <sub>m</sub> ~ 35. (b) The core-shell sphere fit to B <sub>81</sub> O <sub>257</sub> micelles gave R <sub>c</sub> ~ 15 and R <sub>m</sub> ~ 41. ....	172
Figure A.9. Size evolution of PB-PEO micelles that were stirred at 40 °C after dialysis into water. Open symbols represent 40 wt% THF prior to dialysis. Closed symbols represent 0 wt% THF prior to dialysis. DLS on solutions containing B <sub>59</sub> O <sub>180</sub> (blue squares), B <sub>81</sub> O <sub>182</sub> (red circles), or B <sub>81</sub> O <sub>257</sub> (green triangles) demonstrated fairly consistent trends in micelle size relaxation in water (refer to Figure 4.3). ....	173
Figure A.10. (a) Images of B <sub>81</sub> O <sub>182</sub> polymer redissolved in THF after stirring at 60 °C, 40 °C, 22 °C, and 4 °C (40 wt% THF and 10 mg mL <sup>-1</sup> prior to dialysis into water). After the polymer precipitated in water at the specified temperature (see Figure 4.3), the visible precipitates in both water and THF suggested the PB had cross-linked or degraded to varying degrees at temperatures between 22-60 °C. (b) SEC of the B <sub>81</sub> O <sub>182</sub> redissolved in THF did not show cross-linking after agitation at 4 °C. ....	174
Figure B.1. Ice thickness and particle size gradients. Images at lower magnification (left) and higher magnification (right) of B <sub>59</sub> O <sub>180</sub> in water 4 d after dialysis (40 wt% THF, 10 mg mL <sup>-1</sup> prior to dialysis into water).....	176
Figure B.2. Images overlaid at higher magnification. Images were cropped and overlaid for B <sub>59</sub> O <sub>180</sub> in water 7 d after dialysis (40 wt% THF and 10 mg mL <sup>-1</sup> prior to dialysis into water).....	177
Figure B.3. Micelles clustering on top of TEM grid. Image of B <sub>81</sub> O <sub>182</sub> in water 2 d after dialysis (40 wt% THF and 10 mg mL <sup>-1</sup> prior to dialysis into water).....	178
Figure B.4. Single layer of hexagonal packed B <sub>59</sub> O <sub>180</sub> micelles 16 d after dialysis (40 wt% THF and 10 mg mL <sup>-1</sup> prior to dialysis into water).....	179
Figure B.5. Multiple layers of hexagonal packed B <sub>59</sub> O <sub>180</sub> micelles can occur near the grid edges with thicker ice (16 d after dialysis; 40 wt% THF and 10 mg mL <sup>-1</sup> prior to dialysis into water).....	180

Figure B.6. Two layers of hexagonal packed micelles with spacing offset by 5:6 shown schematically (left) and in a real image (right). B <sub>59</sub> O <sub>180</sub> micelles 16 d after dialysis (40 wt% THF and 10 mg mL <sup>-1</sup> prior to dialysis into water). .....	181
Figure B.7. Sample contamination (darker gray, irregular-shaped particles) on a TEM grid containing vitrified B <sub>59</sub> O <sub>180</sub> micelles 16 d after dialysis (40 wt% THF and 2.4 mg mL <sup>-1</sup> prior to dialysis into water). .....	182
Figure B.8. (a-c) Sample degradation due to interactions with the electron beam and ice sublimation. (d) In rare cases, large black ripples appeared after rapid sublimation of the background ice. Sample solutions consisted of B <sub>59</sub> O <sub>180</sub> micelles 16 d after dialysis (40 wt% THF and 2.4 mg mL <sup>-1</sup> prior to dialysis into water).....	183
Figure B.9. Blotting effects likely caused the transition of spherical micelles into cylinder or lamellar structures (rare occurrence for this particular sample). Sample solutions consisted B <sub>59</sub> O <sub>180</sub> 10 d after dialysis (40 wt% THF and 10 mg mL <sup>-1</sup> prior to dialysis into water). .....	184
Figure C.1. Permission statement for <i>Macromolecules</i> , 46, 6319-6325 (2013).....	185
Figure C.2. Permission statement for <i>Nature Communications</i> , 5, 3599 (2014). .....	186

## ABSTRACT

Amphiphilic block polymers consist of covalently linked hydrophobic and hydrophilic polymer segments. These materials spontaneously assemble into various nanoscale structures in aqueous solution such as spherical micelles, cylindrical micelles, vesicles, and other complex morphologies. Utilizing block polymer micelles as drug delivery vehicles, aqueous nanoreactors, and other dispersant technologies demands the ability to encapsulate hydrophobic molecules within the hydrophobic micelle core, which is typically achieved through organic cosolvent processing methods. While cosolvent processing is known to affect micelle dynamics and chain exchange, processing effects in a highly selective solvent after cosolvent removal are less understood. This work investigates the stability of poly(1,2-butadiene-*b*-ethylene oxide) (PB-PEO) core-shell spherical micelles under various processing conditions after cosolvent removal. Processing conditions such as cosolvent addition and removal, polymer concentration, temperature, solution agitation, and interfacial contact were found to influence the stability of block polymer micelles in aqueous solutions. Complementary *in situ* characterization methods, including dynamic light scattering, cryogenic transmission electron microscopy, and small angle neutron scattering, were used to monitor the resulting micelle size evolution and chain exchange following dialysis into water. Despite highly unfavorable PB-water interactions, micelle size relaxation was discovered in aqueous solutions when the micelles were significantly perturbed. Notably, coupled shear and interfacial effects were found to be a key driving force for chain exchange and micelle growth, which

parallels findings for other macromolecular solution assemblies such as proteins. Key findings demonstrated that micelle relaxation timescales were sensitive to the agitation method, agitation rate, temperature, molecular weight, and polymer concentration. Comprehending the interplay between various processing parameters is necessary to better control the kinetic pathways for micelle chain exchange and to further develop materials for emerging applications that hinge on the stability of macromolecular assemblies in aqueous solutions.

## Chapter 1

### INTRODUCTION

The solution assembly of amphiphilic molecules, which are molecules composed of both hydrophilic and hydrophobic domains, has been the focus of a rich variety of fundamental and application-driven investigations over the past several decades.<sup>1</sup> The tunable self-assembly of amphiphilic molecules into aggregates, or micelles, has played a key role in bottom-up strategies for designing various structures in solution with unique properties and functions. Amphiphilic molecules are found naturally in biological systems as well as within a diverse range of applications including protein separations,<sup>2</sup> consumer products such as cosmetics,<sup>3,4</sup> detergents,<sup>3,4</sup> dispersants,<sup>3,4</sup> and emulsifiers,<sup>3,4</sup> emerging technologies such as nanoreactors,<sup>5-7</sup> and other medical applications such as diagnostic agents and drug delivery vehicles.<sup>7,8</sup>

Amphiphilic block polymers are a promising material for many of these applications. Analogous to small molecule surfactants, macromolecular amphiphiles assemble into various nanostructures in solution including spherical micelles, cylindrical micelles, and vesicle bilayers.<sup>9</sup> Unique design features of block polymer solution assemblies such as the size scale, morphology, mechanical properties, and surface functionality can be tuned synthetically by controlling the relative polymer composition, molecular weight, and block chemistry.

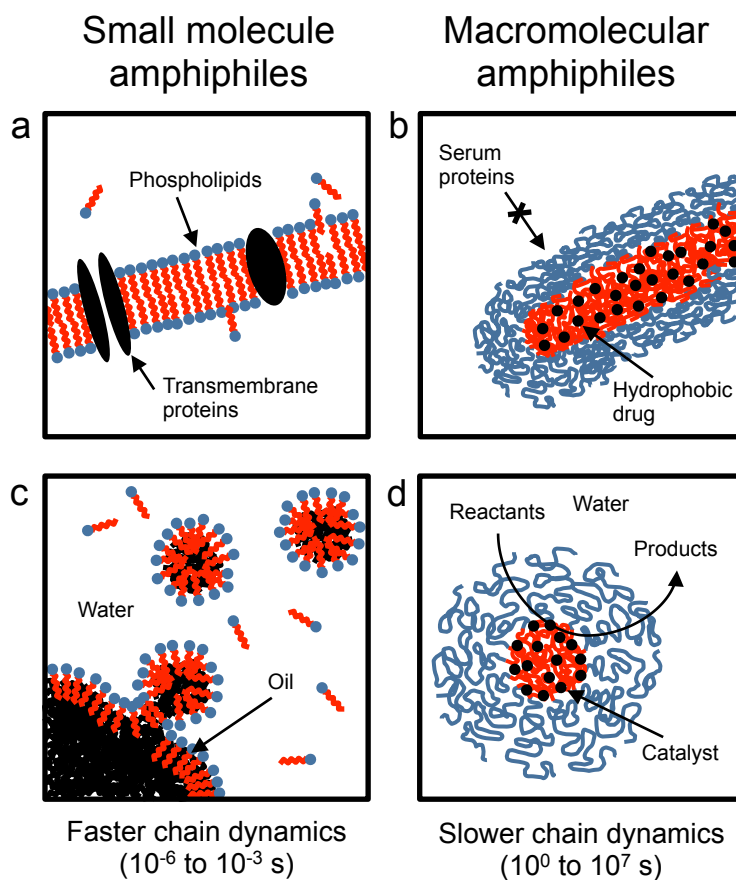


Figure 1.1. Small molecule and macromolecular amphiphiles are found in (a) biological membranes and applications in protein separation, (b) drug delivery vehicles, (c) dispersants and detergents, and (d) aqueous nanoreactors. Chain exchange dynamics play a key role in the surfactant functionality and are typically much faster for small molecule surfactants in comparison to macromolecular surfactants.

The chain exchange dynamics and lifetime of a chain within a solution assembly can be vastly different for small molecule and macromolecular amphiphiles. In general, the lifetime of small molecule amphiphile within a micelle is on the order of microseconds to milliseconds.<sup>1</sup> Meanwhile, the lifetime of a macromolecular amphiphile within a micelle can range drastically from milliseconds to years

depending on the interfacial tension, molecular weight, solvent quality, and temperature.<sup>10</sup> Due to these slow exchange kinetics, macromolecular solution assemblies are typically non-ergodic and path-dependent. This inherent non-ergodicity implies that the aggregate structure and corresponding function can be affected by various solution processing conditions. While this feature can be problematic for product control and formulation, it can be advantageous in some emerging applications that require kinetically-trapped aggregates and hindered mass transport of encapsulated hydrophobic cargoes.

Understanding the kinetic pathways that lead to chain exchange of block polymer solution assemblies is critical to tune these materials for their desired applications and to establish novel capabilities and features. With the advancement of characterization methods such as cryogenic transmission electron microscopy (cryo-TEM) and small angle neutron scattering (SANS), new insights into self-assembled structures and dynamics can be obtained by direct visualization in a vitrified state, or through deuterium contrast-matching methods that probe individual structural components to quantify molecular exchange between aggregates.

The main goal of this work was to incorporate these complementary characterization methods (Chapter 2) to probe the chain exchange kinetics of amphiphilic block polymer micelles in response to effects of cosolvent addition and removal (Chapter 3), molecular weight and temperature (Chapter 4), and flow (Chapter 5). Explorations of these fundamental topics provide insight into micelle chain exchange kinetics in aqueous solutions and emphasize the importance of processing conditions in the preparation of macromolecular solution assemblies. This introduction provides background information on fundamental driving forces, key

system parameters and variables, and scaling relationships for the self-assembly and chain exchange dynamics of block polymer solution assemblies. Specifically, this chapter includes (1.1) fundamentals of block polymer solution assembly, (1.2) applications of block polymer micelles, (1.3) mechanisms of chain exchange, (1.4) effects of processing conditions, and finally (1.5) an overview of the contributions from this work.

## 1.1 Block Polymer Solution Assembly

Analogous to small molecule surfactants, amphiphilic block polymers spontaneously aggregate in water due to the hydrophobic effect.<sup>11</sup> The hydrophobic effect is mainly driven by the entropically unfavorable (more ordered) water structure that is imposed by a non-polar molecule or chain. The gain in water entropy from minimizing interaction with hydrophobic chain outweighs the loss in configurational entropy from the confinement of hydrophobic chain segments. This self-assembly process occurs above a polymer concentration called the critical aggregation concentration (CAC). Aggregation of freely dissolved polymer chains becomes energetically favorable above the CAC upon further addition of polymer, whereas only free chains exist below the CAC. For high molecular weight amphiphilic polymers in water, the CACs are generally much smaller ( $< 10^{-5}$  M) compared to single-chained C<sub>12</sub> to C<sub>16</sub> surfactants ( $10^{-2}$  M to  $10^{-5}$  M).<sup>1</sup>

Free energy analyses through mean-field or scaling methods have established relationships between micelle and polymer properties, such as the CAC, core and corona degree of polymerization, statistical segment length, and aggregation number.<sup>10,12-14</sup> Under the conditions of large aggregation number ( $Q \gg 1$ ), dilute solutions with low polymer volume fraction ( $\phi < 0.01$ ), and large interfacial tension

such that the CAC is low, the polymer-solvent mixing free energy and micelle translational entropy become negligible. These simplifications enable the total free energy for micellization to be approximated as the micelle free energy, otherwise referred to as the “pseudo-phase” approximation, in which the micelle is treated as a separate phase..

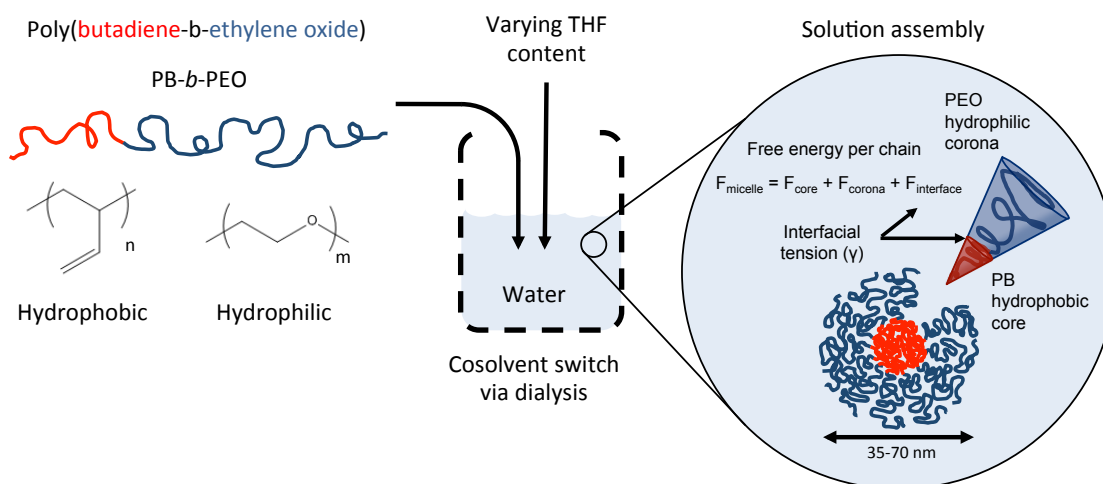


Figure 1.2. Direct dissolution of PB-PEO in water leads to spontaneous self-assembly of a core-shell sphere with diameters  $\sim 35-70$  nm in this particular work. The hydrophobic PB core is sterically stabilized and surrounded by a PEO corona or shell. Free energy minimizing dictates aggregation number, morphology, and micelle size, which can be manipulated by block molecular weight or the core-solvent interfacial tension by THF cosolvent addition. Subsequent cosolvent removal *via* dialysis leaves the metastable micelle structure kinetically-frozen in water under quiescent conditions.

The free energy of a micelle can be decomposed into the sum of three contributions pertaining to the insoluble core block, the interfacial energy between the insoluble core and the solvent, and the soluble corona block, which is written as

$$F_{micelle} = F_{core} + F_{int} + F_{corona} \quad (1.1)$$

in which the free energy is written in dimensionless form (per  $k_B T$  per chain).

For spherical micelles, the free energy from elastic chain stretching within the micelle core beyond the end-to-end distance can be expressed as<sup>10</sup>

$$F_{core} = \frac{\pi^2 R_c^2}{16 N_B l_B^2} \sim Q^{2/3} \quad (1.2)$$

in which  $R_c$  is the core radius,  $N_B$  is the number of segment repeat units, and  $l_B$  is the statistical segment length. Subscript  $B$  denotes the insoluble polymer block while subscript  $A$  denotes the soluble polymer block.

Interfacial contributions can be expressed simply as the surface energy of the micelle core per chain as

$$F_{int} = \frac{4\pi R_c^2 \gamma}{Q} \sim \gamma Q^{-1/3} \quad (1.3)$$

in which  $\gamma$  is the core-solvent interfacial tension, also linked to the Flory-Huggins interaction parameter. The aggregation number is the number of polymer chains in a given micelle, which for a non-swollen micelle core is given as  $Q = 4/3 \pi R_c^3 v_c^{-1}$ , in which  $v_c$  is the core chain volume. This scaling immediately shows that increasing  $R_c$  or  $Q$  lowers the energy, which would drive macroscopic phase separation were it not for the existence of balancing forces arising from the chain stretching within the core and corona. Another implication is that the core-solvent interfacial tension can be adjusted by the addition of a miscible cosolvent, thus changing the micelle free energy and corresponding equilibrium core radius or aggregation number.

Zhulina *et al.* derived an analytical expression in which the corona free energy could be expressed in terms of surface area per chain  $s$ , which is a function of the

distance from the core-interface.<sup>13</sup> The expression for spherical star-like micelles can be approximated as<sup>10,14</sup>

$$F_{corona} \cong \frac{R_c}{\sqrt{s}} \ln \left( 1 + \frac{H}{R_c} \right) \quad (1.4)$$

in which  $H$  is the corona thickness, and numerical coefficients have been dropped. The corona free energy also decreases with core radius, providing another driving force against macroscopic phase separation by favoring smaller aggregation number or micelle core radius.

Minimizing the total micelle free energy in Eq. 1.1 with respect to  $R_c$  or  $Q$  describes the core radius or aggregation number with the lowest energy, which is considered to be the equilibrium size or equilibrium aggregation number. Due to the large kinetic constraints, especially in highly selective solvent systems such as water, it remains difficult to determine if the lowest energy aggregate is truly achieved in reality. This complication is compounded when considering the inherent dispersity in chain molecular weight, chain volumes, and available chain surface areas. While not exact, free energy analysis provides useful scaling relations for important parameters such as<sup>14,15</sup>

$$Q_{eq} \sim \gamma^{6/5} N_B^{4/5} l_B^{12/5} \quad (1.5)$$

in which  $Q_{eq}$  is the aggregation number such that the free energy is minimized for star-like spherical micelles. These relationships are useful to predict changes in aggregation number with solvent and polymer properties, namely core-solvent interfacial tension, degree of polymerization, and segment length.

Changes in the interfacial curvature based on the dimensionless packing parameter can also lead to transitions between morphologies, such as spherical

micelles, cylindrical micelles, and vesicles.<sup>7</sup> In systems with lower interfacial energies and lower timescales for chain exchange, free energy analysis was in good agreement with experimental data that described morphological transitions between spherical and cylindrical micelles for poly(ethylene-*alt*-propylene)-*b*-poly(ethylene oxide) or PEP-PEO block polymers in water/DMF mixtures.<sup>16</sup> Other studies on PB-PEO micelles in THF/water mixtures showed good agreement with star-like micelle scaling relationships.<sup>17</sup>

## 1.2 Applications of Block Polymer Micelles

Surface active agents (surfactants) are used in various applications due to their spontaneous assembly at interfaces. Pluronics are one example of widely used and commercially available non-ionic, water soluble, block polymer surfactant. Pluronics are composed of poly(ethylene oxide) (PEO) and poly(propylene oxide) (PPO) in the form of PEO-PPO-PEO. Owing to the temperature-sensitive solubility of PEO and PPO blocks and the tunable properties with varying block molecular weights, these polymers are widely used in emulsification, lubrication, detergency, and various other product formulation.<sup>3</sup> The relatively low hydrophobicity of PPO typically leads to chain exchange dynamics on the order of minutes to hours, depending on the molecular weight and temperature.<sup>18,19</sup>

Emerging technologies in imaging diagnostics, drug delivery, aqueous nanoreactors, and other dispersant technologies require the ability of amphiphilic block polymers to encapsulate hydrophobic cargoes. For example, one particular goal may be to solubilize and protect a hydrophobic drug within the blood stream, elicit a therapeutic response in a particular location within the body, and limit side effects in other locations. While many of these emerging applications currently employ small

molecule surfactants, micelles formed from higher molecular weight building blocks such as amphiphilic block polymers have several unique properties that can be advantageous and address concerns in translation of these technologies.

One key advantage for block polymers is that both the aggregate length scale (~10-100 nm) and the morphology can be tuned by controlling the relative molecular weights of the hydrophilic and hydrophobic blocks. Size and morphology dictate performance in many applications, including the ability of small particles (< 100 nm) to accumulate in tumors<sup>20</sup> and the ability of soft, cylindrical nanostructures to evade macrophage-mediated immune clearance and thereby prolong blood circulation times.<sup>21</sup> Polymeric materials also exhibit synthetic versatility to allow attachment of functional side-groups (e.g. cleavable moieties, small molecules, targeting peptides, and proteins). This unique tailorability has been heavily researched for a wide range of stimuli-responsive materials.<sup>8</sup> The low CAC, imparted by the high molecular weight of the hydrophobic block, is necessary for applications that require dilute conditions. Due to the high hydrophobic molecular weight and low CAC, the ability for macromolecular amphiphiles to remain aggregated under dilute conditions is very advantageous for drug delivery applications, for example, when the aggregates experience a large dilution effect upon injection.

Another unique property of block polymer micelles is the extremely hindered chain exchange kinetics for sufficiently high molecular weight and hydrophobic polymer components. This feature often leads to kinetically-trapped assemblies that can exhibit more complex structures such as patchy spheres,<sup>22</sup> toroids,<sup>23</sup> and striped cylinders<sup>22,24</sup> which may provide unique structure-function properties. Slow exchange times ( $\sim 10^0$  to  $10^7$  s) can also produce aggregated assemblies with longer lifetimes in

order to prolong and control the release of encapsulated cargoes. The timescale for chain exchange can be tuned by varying the molecular weight and composition of the hydrophobic block, as well as by incorporating stimuli-responsive moieties.

The use of amphiphilic block polymers as drug delivery vehicles has been the focus of numerous investigations, with some materials reaching Phase 2 clinical status. One example (BIND-014, Bind Biosciences) consists of hydrophobic polylactide and hydrophilic polyethylene glycol components. These polymeric drug delivery vehicles take advantage of the sustained and controlled release of docetaxel and incorporate small molecules to target antigens that are overexpressed in solid tumors.<sup>25</sup>

The applicability of amphiphilic macromolecular assemblies is highly dependent on the mechanism and timescale of chain exchange, as well as processing conditions that can affect their structure and function. While only a few examples are highlighted here, the tunable functionality, structure, size, and exchange kinetics of block polymer micelles have proven useful in various industrial, commercial, and emerging technologies.

### **1.3 Chain Exchange Mechanisms**

The chain exchange kinetics of macromolecular assemblies are critical given the propensity for the formation of metastable or trapped structures. Due to the exceptionally slow chain exchange under quiescent conditions in highly selective solvents (e.g. water), the processing conditions play a dominant role in the resulting size and structure of the solution assemblies. Hence, probing the underlying chain exchange mechanism leads to both useful quantitative evaluation and additional insight in controlling the hierarchical assembly of amphiphilic macromolecules.

The chain exchange mechanisms investigated for quiescent solutions are single chain exchange (Fig. 1.3a) and micelle fusion/fission (Fig. 1.3b). Other diffusion-based mechanisms, for instance nucleation and growth processes, may occur for initial micellization from free chains in solution.<sup>26</sup> With incorporation of shear and interfacial effects, other mechanisms become feasible such as shear-induced flocculation (Fig. 1.3c) or interfacial nucleation (Fig. 1.3d). These mechanisms were proposed to occur for the growth of PB-PEO micelles investigated in this work, and thus a brief background on the concepts and theory are discussed below.

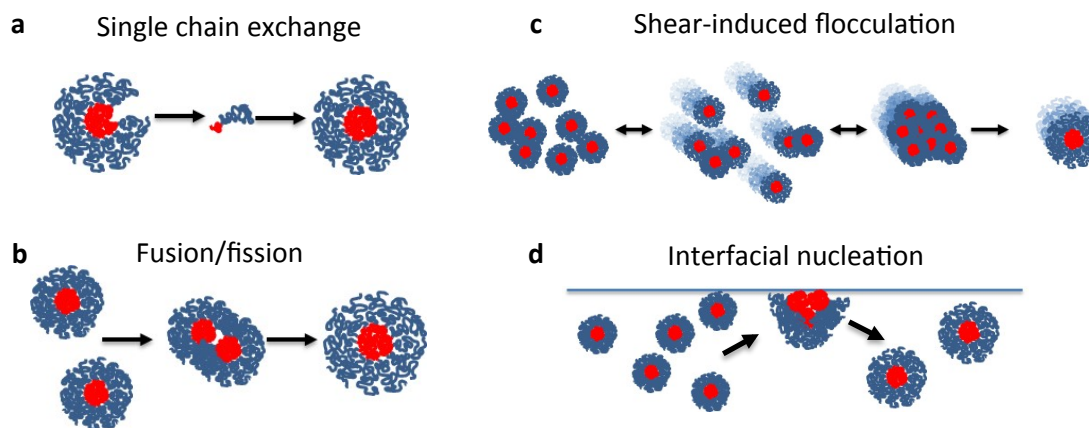


Figure 1.3. Mechanisms for micelle chain exchange include (a) single chain exchange and (b) micelle fusion/fission that can occur due to diffusive or Brownian motion. With addition of shear flow or hydrophobic-hydrophilic interfaces, other proposed mechanisms for micelle chain exchange may include (c) shear-induced flocculation and (d) interfacial nucleation.

### 1.3.1 Single chain exchange

Single chain exchange between micelles can be rationalized into three main stages, namely expulsion of the hydrophobic segment from the core, diffusion of the chain through solution, and insertion of the chain into the core of a separate micelle. It

is generally assumed that exchange kinetics are reaction-limited and not diffusion-limited, as the rate of polymer chain diffusion or rate of collisions between aggregates is much faster than the timescale for expulsion or insertion.

Single chain exchange theory was pioneered by Halperin and Alexander<sup>27</sup> and later was modified by several others.<sup>28</sup> The assumed rate-limiting step is dominated by chain expulsion from the core, and the characteristic “event” frequency is related to the longest relaxation time for unentangled polymer,  $\tau = (l_B^2 N_B^2 \zeta) / (6\pi^2 k_B T)$ , in which  $\tau$  is known as the Rouse time and  $\zeta$  is the monomeric friction coefficient.<sup>29</sup> The probability that an “event” attempt leads to an expelled chain is related to the largest energetic penalty for creating unfavorable core-solvent contact, given as the  $\exp(-\alpha\chi N_B)$ , in which  $\alpha$  is a numerical coefficient of  $O(1)$ , and  $\chi$  is the core-solvent Flory-Huggins interaction parameter ( $\chi \sim 3.5$  for PB-water). Writing these two contributions together as the rate constant in the first-order kinetic rate expression  $K(t)$  according to Halperin and Alexander theory gives<sup>28</sup>

$$K(t) = \exp\left(-\frac{t}{\tau} \exp(-\alpha\chi N_B)\right) \quad (1.6)$$

The double exponential dependence on  $\chi$  (related to the core-solvent interfacial tension) and  $N_B$  demonstrates hypersensitivity to these parameters and predicts extremely slow single chain exchange when the product of  $N_B$  and interfacial tension (or  $\chi$ ) is even modestly large. Note that the hypersensitivity to the core block degree of polymerization suggests a significant broadening in the kinetics due to dispersity, even for monodispersed polymers with  $M_w/M_n < 1.1$ .

### 1.3.2 Micelle fusion and fission

Micelle fusion process involves the contact of two or more collective micelles, followed by the compression of the corona chains and subsequent coalescence of the micelle cores. The largest energy barrier for fusion through coalescence of star-like micelles ( $N_A > N_B$ ) occurs from the compression of the corona chains, which scales with aggregation number as<sup>15</sup>

$$\frac{E_{fusion}}{k_B T} \sim Q_1 Q_2^{1/2} \quad (1.7)$$

in which the aggregation numbers for two micelles follow for  $Q_1 \ll Q_2$ , or the fusion of two dissimilar sized micelles. This scaling relationship assumes compression of chains from their end-to-end distance, and the energy is order  $\sim 1 k_B T$  per chain for a Gaussian coil. The energy barrier for fusion of micelles with thin coronas (crew-cut micelles) is expected to scale as  $\sim Q^2$  for  $Q_1 \sim Q_2$ .<sup>10</sup>

Micelle fission or breakage is essentially the reverse process of fusion, where the micelle core splits into two sections followed by rearrangement of corona chains to surround the newly generated core surface area. The energy barrier for fission of micelles into two smaller micelles is based on the significant energy to generate surface area, which scales with the aggregation number as<sup>15</sup>

$$\frac{E_{fission}}{k_B T} \sim Q_{eq}^{5/6} [Q_1^{2/3} + Q_2^{2/3} - (Q_1 + Q_2)^{2/3}] \quad (1.8)$$

in which  $Q_{eq}$  represents the equilibrium aggregation number.

The scaling relationships for micelle fusion and fission suggest relatively large energetic barriers, especially for micelles with appreciable aggregation numbers. The limit of these scaling relationships with the lowest predicted energy barrier is for  $Q = 1$ , which corresponds to single chain insertion or expulsion. Seminov *et al.*

argued that the energy barrier for fusion/fission would always be larger than single chain exchange based on this rationale.<sup>30</sup> However, Dormidontova posited that fusion/fission processes could occur for micelles far from the equilibrium aggregation number, in which fusion or fission becomes the most efficient method to minimize the micelle free energy.<sup>15,31</sup>

### **1.3.3 Shear-induced flocculation**

Shear-induced (orthokinetic) flocculation occurs when two or more destabilized colloidal particles come in close contact and aggregate or coagulate as a result of collisions from bulk fluid flow, accomplished through stirring or mixing the suspension. The contact of multiple primary particles due to additional attractive interparticle interactions (or a reduction of repulsive interactions) drives agglomeration into a larger particle. This process is distinguished from perikinetic flocculation, in which aggregation of particles is driven by Brownian motion or diffusive motion.<sup>32</sup> Most importantly, flocculation of smaller primary particles leads to bimodal distribution of particle sizes, which remains as one hypothesis for explaining data presented in this work (Chapter 3-5).

High shear rates bring destabilized particles together more quickly and tend to densify flocs.<sup>33</sup> Hence, convection can accelerate the aggregation and coagulation kinetics. However, flow also can break apart flocs, generally producing a balanced steady-state floc size that is dependent on the shear rate. Given the presence of amphiphilic polymer micelle solution, it was hypothesized that metastable PB-PEO micelles, existing in an unfavorable size, could flocculate with increased particle collisions due to flow and additional attractive interactions, for instance, through depletion or polymer bridging interactions. Flow-SANS techniques were employed to

explore the possibility of shear-induced flocculation of perturbed micelles in water (2.3.4 and 5.2.2).

### **1.3.4 Interfacial nucleation**

Amphiphilic molecules adsorb at unfavorable hydrophobic-hydrophilic interfaces, such as an air-water interface, in order to lower the surface energy. Thus, one hypothesized route for micelle chain exchange is through interfacial nucleation, in which micelles adsorb to an interface, aggregate or exchange chains, and subsequently desorb from the interface back into the bulk. In general, desorption energies of surface active particles can be quite large, ranging up to  $\sim 10^3 k_B T$ , which for realistic temperatures can be considered irreversibly adsorbed to the interface.<sup>34</sup> However, particle destabilization and desorption from an interface becomes easily accessible with sufficiently high pressures or deformations of the interface.

Even under dilute concentrations, only a small fraction of micelles exist at or near an interface compared to the number of micelles in the bulk fluid. However, given sufficient time or high surface turnover rates, kinetic processes coupled to the deformation of a fluid interface could become dominant, particularly if particles within the bulk fluid are effectively frozen. For example, one recent investigation showed that the mechanical rupturing of the air-water interface led to aggregated immunoglobulin G proteins, in which the number of aggregates over time was proportional to the number of rupturing events.<sup>35</sup> If surface rupturing were the limiting step in the kinetic pathway for micelle rearrangement, then the rate of chain exchange between micelles should remain constant (i.e. zero-order dependence on polymer concentration or chain length). Furthermore, zero-order rate constants should relate to the saturated surface concentration and surface turnover rate. Presumably,

the route to interfacial aggregation and subsequent dissolution into the bulk fluid would depend on the particle properties, rheological properties of the bulk fluid (e.g. density or viscosity), interfacial properties, and the method of agitation or surface rupturing.

#### **1.4 Experimental Evidence for Micelle Chain Exchange**

Several experimental works have validated proposed mechanisms of chain exchange in solution. Key system parameters generally include core-solvent interfacial tension, core and corona block molecular weight, temperature, and polymer concentration. Highlighted experimental findings are summarized below.

Investigations on micelle chain exchange of non-ionic block polymers in aqueous solutions have generally focused on materials containing poly(ethyl ethylene) (PEE), PEP, PB, or poly(styrene) (PS) as the hydrophobic component, with the majority containing PEO as the hydrophilic component. In pure water, micelles consisting of PEP-PEO or PB-PEO diblock copolymers were found to be effectively frozen under quiescent conditions, with no chain exchange using SANS was measured over long periods (months).<sup>36,37</sup> Both of these highly amphiphilic block polymers become kinetically-trapped upon dissolution in water based on the large interfacial tension between the core block and water.

One route to induce chain exchange of kinetically frozen block polymer micelles was accomplished by lowering the core-solvent interfacial tension through addition of organic cosolvent. Several works examined PEP-PEO micelles in water/DMF mixtures, using solvent compositions within 0% to 50% DMF to tune and subsequently quantify chain exchange using time resolved SANS (TR-SANS).<sup>36,38,39</sup> A time-temperature superposition principle could be employed to broaden the

explored relaxation timescales, which could range from seconds to days depending on various properties. Equilibrium kinetics showed a broad logarithmic relaxation, which was initially perceived as uncertain consequence of multiple hierarchical processes.<sup>10</sup> Later, Choi *et al.* used PS-PEP diblock polymers in squalane to demonstrate that the experimental data could be rationalized as a double exponential dependence (Eq. 1.6) by taking into account exponential prefactors, temperature-dependent diffusion coefficients, and core block polydispersity.<sup>28</sup> This result was confirmed further by intentionally broadening the molar mass dispersity using a bimodal distribution of core block lengths, showing that the timescale for chain exchange could be tuned by molecular weight, core-solvent interaction, and temperature.<sup>40,41</sup>

The hypersensitivity to core block molecular weight and polydispersity was demonstrated using truly monodispersed (i.e.  $\mathcal{D} = 1$ ) n-alkyl-PEO molecules in pure water.<sup>42</sup> Small changes in core molecular weight from C<sub>30</sub>H<sub>61</sub>-PEO<sub>5</sub> to C<sub>18</sub>H<sub>37</sub>-PEO<sub>5</sub> resulted in no measurable chain exchange up to 10<sup>3</sup> s to full equilibration within 10<sup>-3</sup> s (subscripts define number of repeat units). TR-SANS measurements of micelles (C<sub>24</sub>H<sub>49</sub>-PEO<sub>5</sub>) with intermediate relaxation timescales of  $\tau \sim 44$  s was in excellent agreement with a single exponential decay predicted from theory by Halperin and Alexander on single chain exchange (Eq. 1.6 with the second exponential term being constant). Furthermore, the single exponential relaxation was not dependent on polymer concentration within a range of 0.25 vol% to 1 vol%, suggesting that fusion/fission mechanisms did not play a dominant role.

Several studies have found concentration dependent rates, which suggests micelle fusion/fission mechanism may be feasible despite the predicted large energetic barrier. Relaxation kinetics of PB-PEO micelles in ionic liquids at elevated

temperatures (120-170 °C) were shown to be concentration dependent, suggesting the measured decrease in micelle size was due to a fusion/fission mechanisms.<sup>43</sup> In particular, the characteristic timescale was reduced from  $10^4$  s to  $10^3$  s with increasing concentration from 0.05 wt% to 1 wt%. The estimated energetic barrier for the relaxation process was between  $\sim 60$  kJ mol<sup>-1</sup> and  $\sim 140$  kJ mol<sup>-1</sup>, depending on the solvent quality for the core block. Other work by Rharbi on PEO<sub>17</sub>PPO<sub>60</sub>PEO<sub>17</sub> triblock copolymers in water also demonstrated a concentration-dependent rate constant for chain exchange, further suggesting a second order process that was likely a fusion/fission-controlled mechanism.<sup>19</sup> However, unlike PB-PEO in water or ionic liquids, single chain exchange of PEO-PPO-PEO could occur independently of polymer concentration, which was estimated to be a factor of  $\sim 10^6$  faster than the rate for micelle fusion/fission. Computational evidence for fusion/fission has also been shown using dissipative particle dynamic simulations. Using short oligomers as a model system (A<sub>2</sub>B<sub>3</sub> to A<sub>4</sub>B<sub>8</sub>), micelle fusion contributed significantly in the micellization and growth process, leading to an apparent concentration dependent rate as well as multimodal micelle distributions.<sup>31</sup>

## 1.5 Processing Conditions

Contrary to small molecule surfactants with aggregate lifetimes on the order of microseconds to milliseconds, macromolecular amphiphiles experience kinetically-trapped states that may require months, years, or even longer to exchange between micelles. With slow exchange processes that are hypersensitive to interfacial tension and molecular weight, it is not surprising that macromolecular solution assemblies are entirely path dependent. As a result, processing variables such as solvent quality, rate

of dissolution, temperature, and solution agitation will dictate the self-assembled structures.

The morphology, size, and cargo loading of polymeric micelles are known to depend on the sample preparation process and the method for dissolution of polymer.<sup>44</sup> For example, the direct dissolution of PB-PEO into a selective ionic liquid solvent produced distinctly larger spherical micelles than cosolvent-aided dissolution of the same polymer.<sup>43,45</sup> Other dissolution methods, such as flash precipitation or gradual cosolvent addition, can produce different aggregate structures that either contain or release intended hydrophobic cargo.<sup>46</sup> By applying flow and confinement effects, such as the extrusion of polymeric micelles through a thin tube, spherical micelles were shown to fuse together and form metastable cylindrical micelles.<sup>47</sup> These few examples highlight the intricate dependence of processing conditions and demonstrate the ability to tailor unique kinetically-trapped aggregated states.

Quantitative experiments on micelle chain exchange are generally explored under quiescent conditions (i.e. molecular motion due only to thermal energy) to investigate equilibrium kinetics and to compare with corresponding theoretical predictions. However, many envisioned applications involve flowing environments and interfacial effects that may lead to different micelle behavior compared to quiescent conditions. Previous work on block polymer self-assembly has explored effects of shear flow in gas-liquid microfluidic devices, which showed coalescence or breakup of high molecular weight poly(styrene)-*b*-poly(acrylic acid) (PS<sub>665</sub>-PAA<sub>68</sub>) micelles.<sup>48,49</sup> More rigorous Rheo-SANS techniques were used to investigate the nanoscale structure and rheology of kinetically frozen PEP-PEO micelles in water under the influence of shear flow.<sup>50</sup> Depending on the volume fraction of polymer and

the relative PEP or PEO block molecular weight (i.e. star-like or crew-cut micelles), high shear rates were found to affect micelle interactions and lead to shear thinning behavior, which was rationalized by an elongation of the micelles with respect to the flow lines. These examples among other investigations of soft-colloidal systems demonstrate that shear flow can enable unique aggregate assemblies and interactions compared to quiescent conditions.

The influence of processing conditions on block polymer micelles parallels the effects found in dilute protein solutions. Exposure to shear flow and interfacial contact are known to cause protein unfolding and aggregation.<sup>35,51-57</sup> For example, the rotation of aqueous solutions containing monoclonal antibodies resulted in protein aggregation that was proportional to the agitation time.<sup>57</sup> Shear flow effects, interfacial effects, and the relevance to other amphiphilic systems are discussed further in Ch. 5.

## **1.6 Thesis Overview**

This thesis expands the use of complementary solution characterization methods to explore the size evolution of block polymer micelles in aqueous solutions. Various processing conditions that induce micelle chain exchange in aqueous solutions are central in the development of emerging applications that hinge on the stability of block polymer solution assemblies. Furthermore, the results are more broadly relevant to understanding the stability and aggregation of other amphiphilic systems, such as protein, peptide, and other nanoparticle solutions, which have exhibited comparable dependence on processing conditions.

Chapter 2 introduces polymer properties, solution preparation, complementary solution characterization methods, and methods to control the solution environment.

Chapter 3 investigates the size evolution of PB-PEO micelles in aqueous solutions following perturbation of micelle size from their near equilibrium size in THF/water cosolvent mixtures. Dynamic light scattering, cryogenic transmission electron microscopy, and small angle neutron scattering techniques probed the micelle growth, which progressed through a bimodal size distribution and critically depended on solution agitation. These findings suggested that the growth process in a selective solvent (water) was a shear and/or interfacial fusion-controlled process, prompting further investigation into the underlying chain exchange process. Chapter 4 explores the dependence of molecular weight and temperature on the micelle growth process. Notably, temperature and the molecular weight of the core and corona block led to distinct relaxation timescales and steady-state sizes following a cosolvent switch to water. Chapter 5 investigates shear and interfacial effects on micelle size evolution and chain exchange. The exchange kinetics were quantified using SANS and occurred over minutes after rapid vortex mixing. Finally, Chapter 6 provides an overall summary and recommendations for future improvements and investigations.

## REFERENCES

- 1 Israelachvili, J. *Intermolecular & Surface Forces*. 2nd edn, (Elsevier, 1991).
- 2 Ospinal-Jiménez, M. & Pozzo, D. C. Anionic Branched Surfactants as Alternative Denaturing Agents for Protein Separations. *Langmuir* **30**, 1351-1360 (2014).
- 3 Alexandridis, P. & Hatton, T. A. Poly(ethylene oxide)-poly(propylene oxide)-poly(ethylene oxide) block copolymer surfactants in aqueous solutions and at interfaces: thermodynamics, structure, dynamics, and modeling. *Colloids and Surfaces A: Physicochemical and Engineering Aspects* **96**, 1-46 (1995).
- 4 Alexandridis, P. & Lindman, B. *Amphiphilic block copolymers: self assembly and applications*. (Elsevier, 2000).
- 5 Patterson, J. P. *et al.* Catalytic Y-tailed amphiphilic homopolymers - aqueous nanoreactors for high activity, low loading SCS pincer catalysts. *Polymer Chemistry* **4**, 2033-2039 (2013).
- 6 Vriezema, D. M. *et al.* Self-Assembled Nanoreactors. *Chemical Reviews* **105**, 1445-1490 (2005).
- 7 Blanz, A., Armes, S. P. & Ryan, A. J. Self-assembled block copolymer aggregates: from micelles to vesicles and their biological applications. *Macromolecular Rapid Communications* **30**, 267-277 (2009).
- 8 Kelley, E. G., Albert, J. N. L., Sullivan, M. O. & Epps, T. H. Stimuli-responsive copolymer solution and surface assemblies for biomedical applications. *Chemical Society Reviews* **42**, 7057-7071 (2013).
- 9 Jain, S. & Bates, F. S. On the origins of morphological complexity in block copolymer surfactants. *Science* **300**, 460-464 (2003).
- 10 Lund, R., Willner, L. & Richter, D. Kinetics of Block Copolymer Micelles Studied by Small-Angle Scattering Methods. *Advances in Polymer Science* **259**, 51-158 (2013).
- 11 Tanford, C. *The Hydrophobic Effect: Formation of Micelles and Biological Membranes*. 2nd edn, (Wiley-Interscience, 1979).

- 12 Nagarajan, R. & Ganesh, K. Block copolymer self-assembly in selective solvents - Spherical micelles with segregated cores. *Journal of Chemical Physics* **90**, 5843-5856 (1989).
- 13 Zhulina, E. B., Adam, M., LaRue, I., Sheiko, S. S. & Rubinstein, M. Diblock copolymer micelles in a dilute solution. *Macromolecules* **38**, 5330-5351 (2005).
- 14 Zhulina, E. B. & Borisov, O. V. Theory of Block Polymer Micelles: Recent Advances and Current Challenges. *Macromolecules* **45**, 4429-4440 (2012).
- 15 Dormidontova, E. E. Micellization kinetics in block copolymer solutions: Scaling model. *Macromolecules* **32**, 7630-7644 (1999).
- 16 Lund, R. *et al.* Structural and thermodynamic aspects of the cylinder-to-sphere transition in amphiphilic diblock copolymer micelles. *Soft Matter* **7**, 1491-1500 (2011).
- 17 Kelley, E. G., Smart, T. P., Jackson, A. J., Sullivan, M. O. & Epps, T. H. Structural changes in block copolymer micelles induced by cosolvent mixtures. *Soft Matter* **7**, 7094-7102 (2011).
- 18 Landazuri, G., Fernandez, V. V. A., Soltero, J. F. A. & Rharbi, Y. Kinetics of the Sphere-to-Rod like Micelle Transition in a Pluronic Triblock Copolymer. *Journal of Physical Chemistry B* **116**, 11720-11727 (2012).
- 19 Rharbi, Y. Fusion and fragmentation dynamics at equilibrium in triblock copolymer micelles. *Macromolecules* **45**, 9823-9826 (2012).
- 20 Maeda, H. Macromolecular therapeutics in cancer treatment: The EPR effect and beyond. *Journal of Controlled Release* **164**, 138-144 (2012).
- 21 Geng, Y. *et al.* Shape effects of filaments versus spherical particles in flow and drug delivery. *Nat Nano* **2**, 249-255 (2007).
- 22 Groschel, A. H. *et al.* Precise hierarchical self-assembly of multicompart ment micelles. *Nat. Commun.* **3**, 10 (2012).
- 23 Pochan, D. J. *et al.* Toroidal triblock copolymer assemblies. *Science* **306**, 94-97 (2004).
- 24 Cui, H. G., Chen, Z. Y., Zhong, S., Wooley, K. L. & Pochan, D. J. Block copolymer assembly via kinetic control. *Science* **317**, 647-650 (2007).

- 25 Sheridan, C. Proof of concept for next-generation nanoparticle drugs in humans. *Nat Biotech* **30**, 471-473 (2012).
- 26 Lund, R. *et al.* Structural Observation and Kinetic Pathway in the Formation of Polymeric Micelles. *Physical Review Letters* **102**, 188301 (2009).
- 27 Halperin, A. & Alexander, S. Polymeric micelles - their relaxation kinetics. *Macromolecules* **22**, 2403-2412 (1989).
- 28 Choi, S. H., Lodge, T. P. & Bates, F. S. Mechanism of molecular exchange in diblock copolymer micelles: hypersensitivity to core chain length. *Physical Review Letters* **104**, 047802 (2010).
- 29 Choi, S. H., Bates, F. S. & Lodge, T. P. Molecular Exchange in Ordered Diblock Copolymer Micelles. *Macromolecules* **44**, 3594-3604 (2011).
- 30 Nyrkova, I. A. & Semenov, A. N. On the theory of micellization kinetics. *Macromolecular Theory and Simulations* **14**, 569-585 (2005).
- 31 Dormidontova, E. E. & Li, Z. L. Dissipative particle dynamic simulations of kinetics of block copolymer self-assembly. *Abstracts of Papers of the American Chemical Society* **240** (2010).
- 32 Hiemenz, P. C. & Rajagopalan, R. *Principles of Colloid and Surface Chemistry*. Third edn, (CRC Press, 1997).
- 33 Mewis, J. & Wagner, N. J. *Colloidal Suspension Rheology*. 1-393 (Cambridge University Press, 2012).
- 34 Zell, Z. A., Isa, L., Ilg, P., Leal, L. G. & Squires, T. M. Adsorption Energies of Poly(ethylene oxide)-Based Surfactants and Nanoparticles on an Air–Water Surface. *Langmuir* **30**, 110-119 (2013).
- 35 Rudiuk, S., Cohen-Tannoudji, L., Huille, S. & Tribet, C. Importance of the dynamics of adsorption and of a transient interfacial stress on the formation of aggregates of IgG antibodies. *Soft Matter* **8**, 2651-2661 (2012).
- 36 Willner, L., Poppe, A., Allgaier, J., Monkenbusch, M. & Richter, D. Time-resolved SANS for the determination of unimer exchange kinetics in block copolymer micelles. *Europhysics Letters* **55**, 667-673 (2001).
- 37 Won, Y. Y., Davis, H. T. & Bates, F. S. Molecular exchange in PEO-PB micelles in water. *Macromolecules* **36**, 953-955 (2003).

- 38 Lund, R., Willner, L., Richter, D. & Dormidontova, E. E. Equilibrium chain exchange kinetics of diblock copolymer micelles: Tuning and logarithmic relaxation. *Macromolecules* **39**, 4566-4575 (2006).
- 39 Lund, R., Willner, L., Stellbrink, J., Lindner, P. & Richter, D. Logarithmic chain-exchange kinetics of diblock copolymer micelles. *Physical Review Letters* **96**, 068302 (2006).
- 40 Lu, J., Bates, F. S. & Lodge, T. P. Chain Exchange in Binary Copolymer Micelles at Equilibrium: Confirmation of the Independent Chain Hypothesis. *ACS Macro Letters* **2**, 451-455 (2013).
- 41 Lu, J., Choi, S., Bates, F. S. & Lodge, T. P. Molecular Exchange in Diblock Copolymer Micelles: Bimodal Distribution in Core-Block Molecular Weights. *ACS Macro Letters* **1**, 982-985 (2012).
- 42 Zinn, T., Willner, L., Lund, R., Pipich, V. & Richter, D. Equilibrium exchange kinetics in n-alkyl-PEO polymeric micelles: single exponential relaxation and chain length dependence. *Soft Matter* **8**, 623-626 (2012).
- 43 Meli, L., Santiago, J. M. & Lodge, T. P. Path-dependent morphology and relaxation kinetics of highly amphiphilic diblock copolymer micelles in ionic liquids. *Macromolecules* **43**, 2018-2027 (2010).
- 44 Hayward, R. C. & Pochan, D. J. Tailored assemblies of block copolymers in solution: It is all about the process. *Macromolecules* **43**, 3577-3584 (2010).
- 45 Meli, L. & Lodge, T. P. Equilibrium vs metastability: High-temperature annealing of spherical block copolymer micelles in an ionic liquid. *Macromolecules* **42**, 580-583 (2009).
- 46 Gindy, M. E., Panagiotopoulos, A. Z. & Prud'homme, R. K. Composite Block Copolymer Stabilized Nanoparticles: Simultaneous Encapsulation of Organic Actives and Inorganic Nanostructures. *Langmuir* **24**, 83-90 (2007).
- 47 Chen, Q., Zhao, H., Ming, T., Wang, J. & Wu, C. Nanopore Extrusion-Induced Transition from Spherical to Cylindrical Block Copolymer Micelles. *Journal of the American Chemical Society* **131**, 16650-16651 (2009).
- 48 Wang, C.-W., Sinton, D. & Moffitt, M. G. Flow-Directed Block Copolymer Micelle Morphologies via Microfluidic Self-Assembly. *Journal of the American Chemical Society* **133**, 18853-18864 (2011).

- 49 Wang, C.-W., Sinton, D. & Moffitt, M. G. Morphological Control via Chemical and Shear Forces in Block Copolymer Self-Assembly in the Lab-on-Chip. *ACS Nano* **7**, 1424-1436 (2013).
- 50 Stellbrink, J., Lonetti, B., Rother, G., Willner, L. & Richter, D. Shear induced structures of soft colloids: Rheo-SANS experiments on kinetically frozen PEP-PEO diblock copolymer micelles. *Journal of Physics-Condensed Matter* **20** (2008).
- 51 Bai, G., Bee, J. S., Biddlecombe, J. G., Chen, Q. & Leach, W. T. Computational fluid dynamics (CFD) insights into agitation stress methods in biopharmaceutical development. *International Journal of Pharmaceutics* **423**, 264-280 (2012).
- 52 Kiese, S., Pappenger, A., Friess, W. & Mahler, H.-C. Shaken, not stirred: Mechanical stress testing of an IgG1 antibody. *Journal of Pharmaceutical Sciences* **97**, 4347-4366 (2008).
- 53 Thomas, C. R. & Geer, D. Effects of shear on proteins in solution. *Biotechnology Letters* **33**, 443-456 (2011).
- 54 Roberts, C. J. *Nucleation, Aggregation, and Conformational Distortion*. 125-149 (John Wiley & Sons, Inc., 2014).
- 55 Sluzky, V., Tamada, J. A., Klibanov, A. M. & Langer, R. Kinetics of insulin aggregation in aqueous solutions upon agitation in the presence of hydrophobic surfaces. *Proceedings of the National Academy of Sciences* **88**, 9377-9381 (1991).
- 56 Wiesbauer, J., Prassl, R. & Nidetzky, B. Renewal of the Air–Water Interface as a Critical System Parameter of Protein Stability: Aggregation of the Human Growth Hormone and Its Prevention by Surface-Active Compounds. *Langmuir* **29**, 15240-15250 (2013).
- 57 Bee, J. S. *et al.* Production of particles of therapeutic proteins at the air-water interface during compression/dilation cycles. *Soft Matter* **8**, 10329-10335 (2012).

## **Chapter 2**

### **EXPERIMENTAL METHODS**

This chapter describes the experimental methods for investigating chain exchange in block polymer solution assemblies. Figure 2.1 shows the general topics of discussion, namely material properties, solution preparation conditions, complementary solution characterization methods, and solution environment. Some figures and text are reproduced in part with permission from *Macromolecules*, 46, 6319-6325 (2013). Copyright 2013 American Chemical Society. Some of the figures and text are reproduced in part with permission from *Nature Communications*, 5, 3599 (2014). Copyright 2014 Nature Publishing Group.

Section 2.1 briefly describes the polymer properties. Characteristics such as molecular weight of the core [poly(butadiene), PB] and corona [poly(ethylene oxide), PEO] blocks are an important distinguishing factor explored later in Ch. 4. Section 2.2 describes solution preparation conditions for adding and removing cosolvent, as well as determining polymer concentration after dialysis and mixing procedures for contrast-matching experiments. Section 2.3 focuses on solution characterization methods, namely dynamic light scattering (DLS), cryogenic transmission electron microscopy (cryo-TEM), and small angle neutron scattering (SANS). These methods are complementary in terms of balancing the challenges necessary to perform the experiments and the obtained sample information. Section 2.4 describes the methods for controlling the solution environment, specifically temperature and solution agitation.

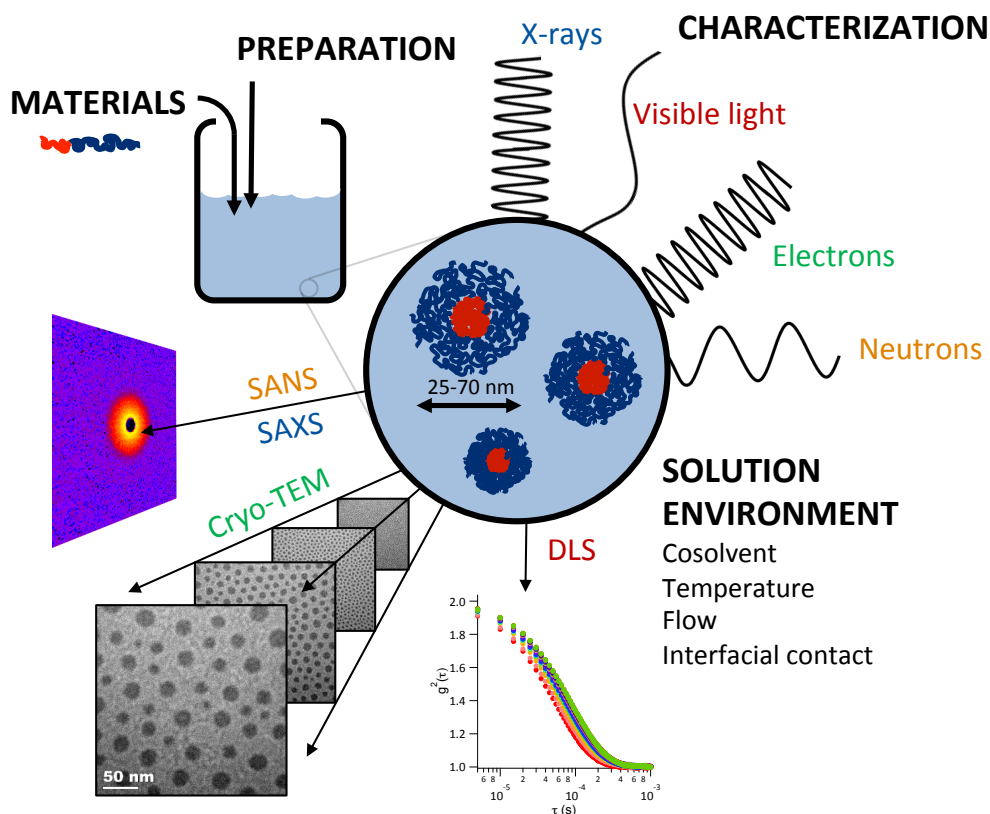


Figure 2.1. Experimental topics of (2.1) materials, (2.2) solution preparation, (2.3) complementary solution characterization methods, and (2.4) solution environment are discussed. Material properties, solution preparation, and solution processing environments are important parameters that affect block polymer micelle size, structure, and chain dynamics in solution. Complementary *in situ* methods are required to properly characterize micelle solutions and to provide insight into dynamic processes.

## 2.1 Material Properties

The amphiphilic block polymer chosen to explore the chain exchange in aqueous solutions was poly(butadiene-*b*-ethylene oxide) or PB-PEO (Table 1.1). It is important to note some characteristics of PB-PEO compared to other polymer systems. One important characteristic of PB (1,2-PB isomer) is its low glass transition temperature ( $T_g = -12\text{ }^\circ\text{C}$ ), which allows it to form a dense core in water that is not

hindered by glassy dynamics.<sup>1</sup> For example, previous experiments examining poly(styrene-*b*-ethylene oxide) in ionic liquids found arrested kinetics unless the temperature was increased above the core  $T_g$  of polystyrene (70 °C)<sup>2</sup>, which demonstrated the strong influence of glassy core dynamics on the timescale for chain exchange. A second important aspect is the relatively low number of predicted entanglements of 1,2-PB ( $M_e = 2 \text{ kg mol}^{-1}$ ).<sup>1</sup> The lower PB molecular weight allowed examination of chain exchange with minimal complications of core entanglements, which will affect the core chain mobility and hence relaxation kinetics. Thus, it is important to account for these important aspects when relating trends and timescales of the chain exchange kinetics presented in this work.

Detailed procedures to synthesize PB-PEO via anionic polymerization are described elsewhere.<sup>3</sup> Using the same methods, deuterated polymer analogs (PB-*d*PEO) with matching molecular weight were synthesized for SANS contrast-matching experiments. All polymers in subsequent studies were synthesized by Dr. Elizabeth G. Kelley.

Polymer properties were characterized with size exclusion chromatography (SEC), matrix-assisted laser desorption/ionization time of flight mass spectrometry (MALDI-TOF), and proton nuclear magnetic resonance (<sup>1</sup>H NMR) spectroscopy. Table 2.1 shows the number average molar mass ( $M_n$ ) determined through a combination of MALDI-TOF and <sup>1</sup>H-NMR analysis. The PB-OH precursor polymers consisted of  $92 \pm 1\%$  of 1,2-PB content (8% 1,4-PB), determined by <sup>1</sup>H NMR. Degree of polymerization ( $N$ ) was based on the monomer repeat unit masses for PB ( $54 \text{ g mol}^{-1}$ ), PEO ( $44 \text{ g mol}^{-1}$ ), and *d*PEO ( $48 \text{ g mol}^{-1}$ ). Polymer dispersities ( $M_w/M_n$ ) were determined with SEC based on polystyrene standards. Achieving low polymer

molecular weight dispersity ( $\mathfrak{D} < 1.1$ ) was important for producing narrow micelle size distributions and uniform solution morphologies (spheres).<sup>4,5</sup>

Table 2.1. Block polymer properties and notations. Number average molecular weight ( $M_n$ ), degree of polymerization (N), and dispersity ( $\mathfrak{D}$ ) are given for each block polymer used in subsequent experiments.

Notation	PB $M_n$ [kg mol <sup>-1</sup> ]	$N_{PB}$	PEO $M_n$ [kg mol <sup>-1</sup> ]	$N_{PEO}$	PEO wt%	$\mathfrak{D}$ ( $M_w/M_n$ )
B <sub>59</sub> O <sub>180</sub> PB- <i>h</i> PEO	3.2	59	7.9	180	71%	1.08
B <sub>59</sub> <i>d</i> O <sub>163</sub> PB- <i>d</i> PEO	3.2	59	7.8 <sup>(1)</sup>	163 <sup>(1)</sup>	71% <sup>(1)</sup>	1.09
B <sub>81</sub> O <sub>182</sub>	4.4	81	8.0	182	65%	1.05
B <sub>81</sub> O <sub>257</sub>	4.4	81	11.3	257	72%	1.06

(1) Deuterated poly(ethylene oxide-*d*<sub>4</sub>) or *d*PEO

Creating PB-PEO polymers with different molecular weights was important for examining the effects of core molecular weight (PB  $M_n$ ) on the subsequent chain exchange kinetics (B<sub>59</sub>O<sub>180</sub> vs. B<sub>81</sub>O<sub>182</sub>) with constant corona molecular weight (PEO  $M_n$ ). Likewise, it was also interesting to compare the effects of different corona molecular weights on chain exchange kinetics (B<sub>81</sub>O<sub>182</sub> vs. B<sub>81</sub>O<sub>257</sub>). Lastly, the effect of increasing molecular weight of both blocks with the same PEO wt% could be examined (B<sub>59</sub>O<sub>180</sub> vs. B<sub>81</sub>O<sub>257</sub>). Polymers with deuterated PEO (PB-*d*PEO, B<sub>59</sub>*d*O<sub>163</sub>) but similar molecular weight and dispersity (PB-*h*PEO, B<sub>59</sub>O<sub>180</sub>) were used for contrast-matched SANS experiments.

Deionized water ( $\text{H}_2\text{O}$ , 18.2 M $\Omega$  resistance) was obtained by purification using a Milli-Q Biocel system (Millipore). Tetrahydrofuran without additives (THF optima, 99.9%, Fisher Scientific) was used as received. Deuterated water ( $\text{D}_2\text{O}$ , 99.9% D, Cambridge Isotopes) for SANS experiments was used as received.

## **2.2 Solution Preparation**

The following sections focus on solution preparation conditions. These sections include (2.2.1) the method for adding and removal THF cosolvent, (2.2.2) determining polymer concentration after dialysis, and (2.2.3 – 2.2.4) preparing contrast-matched solutions for SANS experiments.

### **2.2.1 Controlling cosolvent addition and removal**

The method used to dissolve bulk polymer is an important determinant for path-dependent solution assemblies. The simplest method involves directly adding a selective solvent to polymer with stirring (direct dissolution). Other more involved methods use miscible solvents (cosolvent method)<sup>6</sup>, immiscible solvents (emulsion methods)<sup>7</sup>, or thin-film rehydration to lower energetic barriers for chain exchange processes and thereby aid dissolution of amphiphilic molecules. As noted before, the low  $T_g$  and low entanglements of PB-PEO polymers allowed for reproducible sizes and structures with direct dissolution in pure water. This direct dissolution in water produced similar sized PB-PEO aggregates even with the very high interaction parameter of PB and water ( $\chi \sim 3.5$ ).<sup>8</sup> The polymer solutions were not filtered after direct dissolution to prevent changes in polymer concentration and to avoid disrupting micelle structure. Consequently, care was taken to remove dust from all vials and pipettes for subsequent characterization. To speed up the breakage of bulk PB-PEO

powder and allow for equilibration, polymer solutions were allowed to magnetically stir at 200 rpm for 3 d in water. All micelle solutions were covered during mixing and storage to limit the light-initiated cross-linking of PB.

After 3 d of stirring, the desired THF mass was added dropwise to the aqueous polymer solution (THF density =  $0.889 \text{ g cm}^{-3}$  and water =  $0.998 \text{ g cm}^{-3}$  at  $20 \text{ }^{\circ}\text{C}$ ). After THF cosolvent addition, the solutions were sealed in a glass vial with a Teflon cap, covered with parafilm, and magnetically stirred for 3 d (200 rpm with a Teflon-coated stir bar).

THF cosolvent was subsequently removed through a dialysis method. Dialysis tubing (Spectra/Por Regenerated Cellulose Dialysis Tubing, 12 to 14  $\text{kg mol}^{-1}$  MWCO) was soaked and hydrated with water for  $\sim 30$  min prior to loading the water/THF/polymer solutions. A 200-fold volume excess of  $\text{H}_2\text{O}$  was used as the reservoir to exchange THF with water within the dialysis bag. Fresh reservoir water was exchanged after 4 h and 8 h to ensure all of the THF was removed from the dialysis bag. Total dialysis time was 24 h to ensure THF did not remain dissolved within the hydrophobic PB core, which would lead to swelling of the PB core. (The core size determined from cryo-TEM and model fits to SANS data suggested a non-swollen PB core). Time immediately prior to dialysis was designated as “Day -1”. The time point 24 h after dialysis was designated as “Day 0”. Subsequent time thereafter was “Day 1,” “Day 2,” etc. After dialysis, solutions were mixed as described (e.g. magnetic stirring, rapid vortex mixing, concentric cylinder Couette flow, or gas sparging) or examined under quiescent conditions as a control.

### 2.2.2 Polymer concentration after dialysis

The polymer concentration in  $\text{mg mL}^{-1}$  (mass of polymer per volume of solvent) before dialysis was determined by measuring the mass of polymer and mass of water or THF added to the vial. However, after the removal of THF cosolvent from the micelle solution, the dialysis bag swelled due to osmotic pressure. Consequently, the polymer solution inside the dialysis bag was diluted, and the polymer concentration was lowered (generally a two-fold dilution). One method to determine dilute polymer concentration post-dialysis involved measuring the UV-Vis absorbance and comparing to a known absorbance-concentration calibration. The calibration for PB-PEO in  $\text{H}_2\text{O}$  or blended PB-*d*PEO/PB-*h*PEO polymers in  $\text{D}_2\text{O}$  is shown in Figure 2.2. The linear relationship between light absorbance and concentration in the dilute concentration limit was expected from the Beer-Lambert relation (assuming constant absorption coefficients).<sup>9</sup> The absorbance measurements and polymer concentrations for the calibration curves are listed in Appendix A (Figure A.1).

The corresponding polymer concentrations determined before and after dialysis using the UV-Vis calibration are listed in Table 2.2 for the two polymer blends. The choice of absorbance characterization at 259 nm was arbitrary, but the particular choice in wavelength provided good signal to noise ratio for the particular polymer materials (other wavelengths also showed a linear trend). The uncertainties in initial concentrations were from the error in measured masses. All other uncertainties represented the 95% confidence interval based on at least three replicate absorbance measurements for each concentration and the propagation of error from estimating the corresponding concentration from the linear best-fit line.

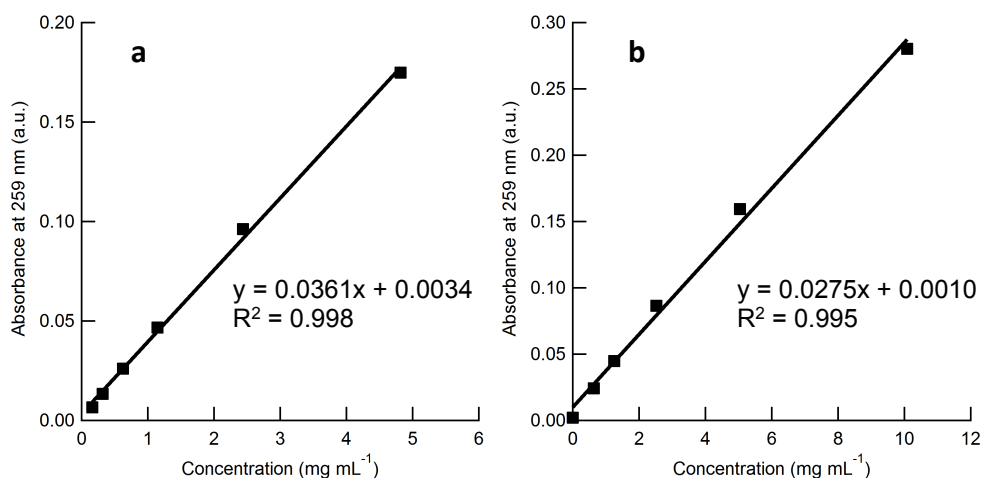


Figure 2.2. UV-Vis calibration curve to determine polymer concentration after dialysis. (a) B<sub>59</sub>O<sub>180</sub> in H<sub>2</sub>O (b) Blend of 88 wt% B<sub>59</sub>dO<sub>163</sub> / 12 wt% B<sub>59</sub>O<sub>180</sub> in D<sub>2</sub>O. Figure reproduced in part with permission from *Nature Communications*, 5, 3599 (2014).<sup>10</sup>

Table 2.2. Polymer concentration determined pre- and post-dialysis to pure H<sub>2</sub>O or D<sub>2</sub>O using calibration curves.

Polymer blend composition	Concentration before dialysis [mg mL <sup>-1</sup> ]	Absorbance at 259 nm after dialysis [a.u.]	Concentration after dialysis [mg mL <sup>-1</sup> ]
100 wt% B <sub>59</sub> O <sub>180</sub>	10.0 ± 0.1	0.200 ± 0.003	5.5 ± 0.1
	5.0 ± 0.1	0.097 ± 0.007	2.6 ± 0.1
	2.4 ± 0.1	0.053 ± 0.010	1.4 ± 0.1
88 wt% B <sub>59</sub> dO <sub>163</sub> 12 wt% B <sub>59</sub> O <sub>180</sub>	10.1 ± 0.1	0.166 ± 0.003	5.6 ± 0.3
	5.0 ± 0.1	0.086 ± 0.001	2.7 ± 0.3
	2.4 ± 0.1	0.070 ± 0.004	2.1 ± 0.3

In the future, the swelling of the dialysis bag could be avoided by using commercially available rigid dialysis tubing (typically made of cellulose). However, caution should be taken to ensure that cellulose tubing does not dissolve or degrade in THF and cause sample contamination.

### 2.2.3 Contrast-matched polymer solutions for SANS

One major advantage of using neutron scattering is the large inherent contrast between hydrogen and deuterium, which enables unique contrast-matching experiments to explore specific structural components. Consequently, deuterated water ( $D_2O$ ) and hydrogenated water ( $H_2O$ ) have drastically different neutron scattering cross-sections and can be mixed in specified proportions to control the overall solvent contrast, assuming the solution is homogeneous. Likewise, PB-*h*PEO and PB-*d*PEO contain coronas with significantly different scattering contrast in a given solvent composition. A match point exists such that the micelle core, micelle corona, or both can be contrast-matched to the solvent such that specific micelle segments do not contribute to the measured scattered intensity. The technique of hydrogen/deuterium contrast-matching in SANS has been widely utilized as it has significant advantages for elucidating complex structures by selectively highlighting individual components in macromolecular assemblies.<sup>11</sup>

The contrast-match point of the PEO corona to the surrounding pure  $D_2O$  solvent for PB-*h*PEO / PB-*d*PEO was measured to be a blend of 88 wt% PB-*d*PEO / 12 wt% PB-*h*PEO. (Note that all PB-*h*PEO or PB-*d*PEO polymers correspond to  $B_{59}O_{180}$  and  $B_{59}dO_{163}$  for neutron scattering experiments). This match point mixture produced a minimum intensity condition with scattering contrast only between the PB core and solvent background. All other polymer mixtures in pure  $D_2O$  would have residual corona-solvent and core-corona contrast, leading to higher scattered intensity. This corona-solvent matched condition was used to probe the micelle core size distribution following cosolvent removal with SANS.

Following this same concept, a micelle with randomly mixed chains of 50 wt% PB-*h*PEO / 50 wt% PB-*d*PEO required a solvent composition of 64 vol%  $D_2O$  / 36

vol% H<sub>2</sub>O to contrast-match the corona. This condition (zero-average contrast) was used to investigate the rate of chain exchange between micelles in aqueous solutions following mixing, which is discussed further in the following section.

#### **2.2.4 Pre-mixed and post-mixed micelle solutions for SANS**

The “pre-mixed” micelle solution corresponds to the condition where PB-*h*PEO and PB-*d*PEO were blended, dried, and then re-dissolved in solution to ensure that all micelles would contain both *h*PEO and *d*PEO. Pre-mixed samples for chain exchange experiments were prepared as follows. First, the 50 wt% PB-*h*PEO and 50 wt% PB-*d*PEO polymers were blended in benzene, stirred overnight, and freeze-dried to remove solvent. Then, the polymer blend was dissolved in a D<sub>2</sub>O/H<sub>2</sub>O mixture (64 vol% D<sub>2</sub>O) at a concentration of 2 mg mL<sup>-1</sup> polymer in solvent and stirred for 3 d. The pre-mixed samples for determining the core size distribution following dialysis were prepared in the same manner only with 12 wt% PB-*h*PEO / 88 wt% PB-*d*PEO in pure D<sub>2</sub>O.

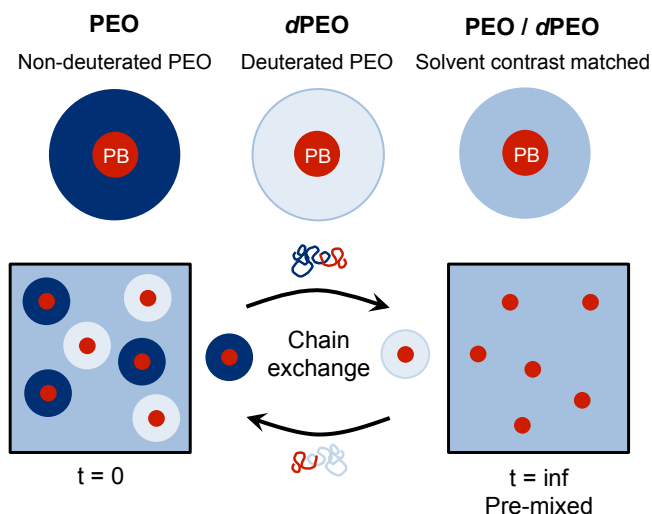


Figure 2.3. Contrast-matching for neutron scattering experiments. An equal volume mixture of PB-*h*PEO micelles and PB-*d*PEO micelles will have decreased scattering contrast after chains are exchanged between micelles. If chain exchange occurs, the maximum scattered-intensity condition directly after mixing ( $t = 0$ ) will approach the minimum scattered-intensity condition or randomly mixed condition (pre-mixed or  $t = \infty$ ). *Macromolecules*, 46, 6319-6325 (2013). Figure reproduced in part with permission from *Nature Communications*, 5, 3599 (2014).<sup>10</sup>

The “post-mixed” micelle solutions correspond to the condition where separate micelle solutions containing either pure PB-*h*PEO micelles or pure PB-*d*PEO micelles were mixed with each other. Individual PB-*h*PEO micelles were prepared by dissolving dry polymer powder in a 64 vol% D<sub>2</sub>O / 36 vol% H<sub>2</sub>O solvent mixture followed by stirring for 3 d. PB-*d*PEO micelles were prepared in an identical manner. Both solutions had a final concentration of 2 mg mL<sup>-1</sup> polymer in solvent. For samples at time  $t = 0$  d, equal volumes of the PB-*h*PEO and PB-*d*PEO micelle solutions were mixed using a calibrated pipette, and the mixed was analyzed with SANS. For samples at time  $t = 10$  d, equal volumes of the PB-*h*PEO and PB-*d*PEO

solutions were mixed, magnetically stirred (200 rpm) at room temperature for 10 d, and analyzed with SANS.

With both pre-mixed or post-mixed solutions, the integrated scattered intensity  $I(t)$  after a given mixing time  $t$  can be found by numerically integrating the  $q$ -dependent scattered intensity  $I(q, t)$  over reasonable  $q$ -range:

$$I(t) = \int I(q, t) dq \quad (2.1)$$

As will be shown below, the integrated  $q$ -range for estimating  $I(t)$  must be low enough to avoid residual core-corona contrast.

Integral intensity for a micelle having a volume fraction of protonated chains  $f$  and deuterated chains  $[1 - f]$  in a solvent that has zero-average contrast conditions can be written as<sup>12</sup>

$$I^h(t) \sim \left( \{f(t)\rho_h - [1 - f(t)]\rho_d\} - \left\{ \frac{\rho_h + \rho_d}{2} \right\} \right)^2 \quad (2.2)$$

in which the first term in curly brackets represents the scattering contrast from a micelle and the second term represents the scattering contrast from the solvent (written in the imposed zero-average contrast conditions by definition). Reducing Eq. 2.2 leads to

$$\sqrt{I^h(t)} \sim (\rho_h - \rho_d)f(t) - \frac{1}{2}(\rho_h - \rho_d) \quad (2.3)$$

which shows that the square root of the intensity scales linearly with the volume fraction of chains exchanged. Using the method to obtain zero-average contrast condition at infinite time, the exchange kinetics can be quantified by the function<sup>12</sup>

$$R(t) = \left( \frac{I(t) - I(\infty)}{I(0) - I(\infty)} \right)^{1/2} \quad (2.4)$$

in which  $I(\infty)$  represents the integrated intensity of the pre-mixed sample,  $I(0)$  represents the integrated intensity at time  $t = 0$ , and  $I(t)$  represents the integrated intensity at time  $t$ .

For the case when residual contrast between the core and corona exists, such as the case when the core block is always protonated (*hPB*), the average intensity in a mixture of *h*-micelles and *d*-micelles can be written as<sup>12</sup>

$$I(q, t) \sim \frac{1}{2} \left( I^h(q, t) + I^d(q, t) \right) + B \quad (2.5)$$

in which  $I^h(q, t)$  and  $I^d(q, t)$  incorporate a time dependent core-shell model, and  $B$  relates to the incoherent background scattering. This background scattering is constant and relates to the incoherent scattering cross-section (i.e. the scattering is isotropic and does not contain a phase factor).<sup>12</sup>

Analogous to Eq. 2.4, the fraction of exchanged chains as a function of time for this condition is given as<sup>12</sup>

$$f_{ex}(t) = \frac{f(t) - f(\infty)}{f(0) - f(\infty)} \quad (2.6)$$

which is dependent on the initial and final homogeneously mixed fraction of exchanged chains. Importantly, at low  $q$ -range it has been shown experimentally that  $f_{ex}(t)$  and  $R(t)$  are equivalent due to minimal scattering from local domains of *h*-chains or *d*-chains and minimal core-corona contrast.<sup>13</sup> To bypass modeling the scattering of a time-dependent core-shell micelle, Eq. 2.4 was used to quantify the exchange kinetics by integrating the measured absolute intensity over a low  $q$ -range ( $q < 0.02 \text{ \AA}^{-1}$ ) to avoid residual local domains that can affect the integrated intensity. Experimental data exploring these concepts and quantifications of exchanged chains are presented in Ch. 3 and Ch. 5.

### 2.3 Complementary Solution Characterization Methods

The focus of this thesis centers on the ability to characterize the size, morphology, and other properties of block polymer solution assemblies. While there are many experimental techniques available for particle characterization, only a select number of techniques have the ability to (1) provide nanometer size resolution and (2) examine the assemblies in solution without drying. Arguably, one single technique cannot confidently characterize a system without additional congruent information from another technique. Each technique has its own advantages and disadvantages, and therefore complementary information is necessary to fill the gaps of uncertainty for each approach.

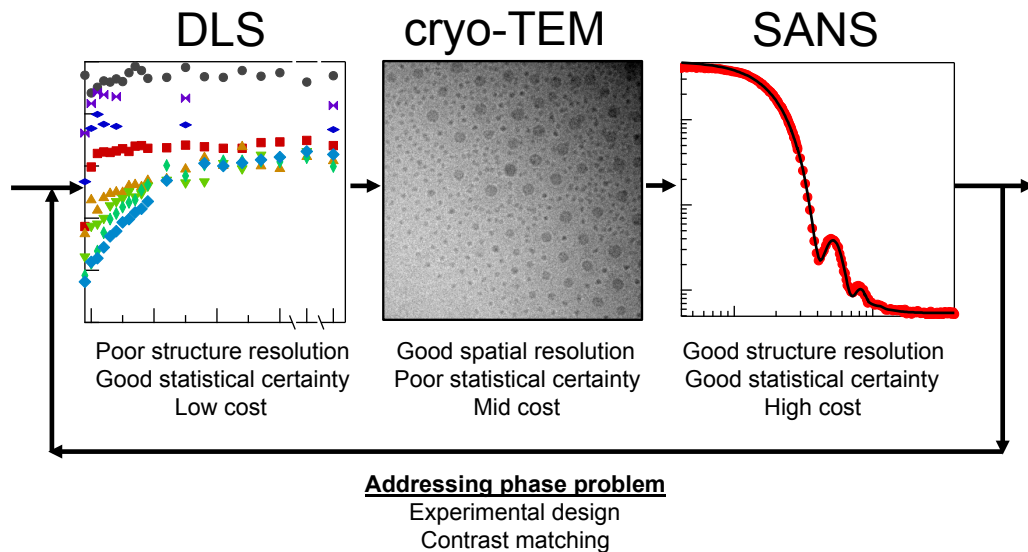


Figure 2.4. Complementary characterization techniques transition from lowest required time and resources and also lowest level of understanding (DLS) to more time consuming yet insightful techniques (cryo-TEM and SANS).

Three complementary techniques are addressed here for the characterization of block polymer micelles, namely dynamic light scattering (DLS), cryogenic transmission electron microscopy (cryo-TEM), and small angle neutron scattering (SANS). Figure 2.4 illustrates the methodology and rationale behind the use of these three techniques to study changes in the size and structure of block polymer solution assemblies. The following sections compare advantages and disadvantages of DLS (2.3.1), cryo-TEM (2.3.2), and SANS (2.3.3) techniques, summarizing the necessary theory, experimental background, and main information obtained from each method. Overall, the approach in methodology aims to optimize the trade-off between required time and obtained insight by using accessible methods (DLS) to establish trends and reproducibility before introducing more demanding and expensive techniques (cryo-TEM and especially SANS).

### **2.3.1 Dynamic light scattering (DLS)**

Particle size distributions in dilute solutions can be probed with dynamic light scattering methods. DLS instruments are widely available, require little experiment time (< 5 minutes per sample), use inexpensive resources (light), and provide good sampling statistics by scattering off a large portion of the solution. These characteristics have made DLS a popular technique for characterizing dilute colloidal suspensions. Major drawbacks of the technique include poor structural resolution and potentially misleading intensity-weighted size distributions. The underlying size distributions are skewed toward larger particles due to intensity weighting, which renders smaller particles nearly undetectable in the presence of much larger particles. Moreover, this effect is complicated further with polydisperse sizes and structures. As a consequence of these drawbacks, DLS can present several problems quantifying

particle size or particle growth kinetics. Nevertheless, the technique provides a quick and reliable metric to approximate size scales, to distinguish changes in size, and to establish general trends.

The fundamental basis for DLS arises from the physical phenomenon that intensity fluctuations in scattered light can be related to the density fluctuations or diffusion of particles within a defined volume. Figure 2.5 illustrates the concept that smaller particles with larger diffusivities lead to faster fluctuations in light intensity, and conversely larger particles lead to slower fluctuations.

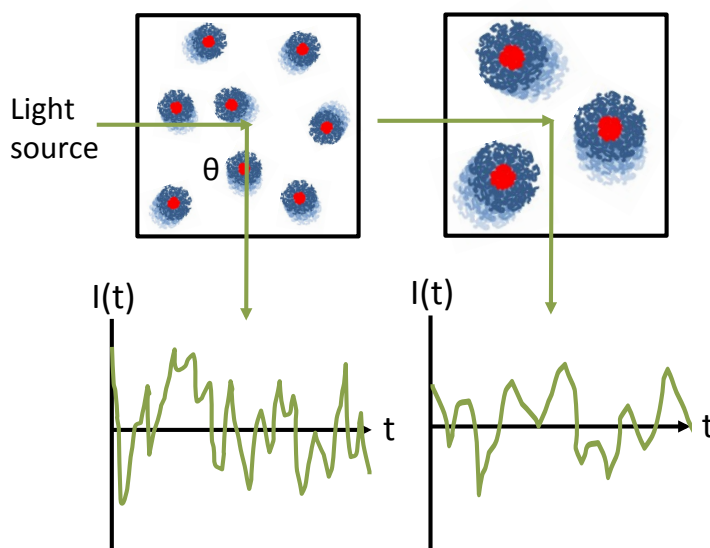


Figure 2.5. Simplified concept of dynamic light scattering. Smaller particles move faster from diffusive motion, which results in faster fluctuations in scattered light intensity. Larger particles move slower from diffusive motion, giving slower fluctuations in scattered light. These intensity fluctuations can be correlated to effective diffusion coefficients, which can in turn be related to particle hydrodynamic diameter.

To describe these concepts mathematically, the wavevector magnitude  $q$  for scattered light intensity is defined as

$$q = \frac{4\pi n}{\lambda} \sin\left(\frac{\theta}{2}\right) \quad (2.7)$$

in which  $n$  is the solvent refractive index,  $\lambda$  is the light wavelength, and  $\theta$  is the scattering angle. For reference, a scattering angle of  $90^\circ$ , pure water  $n = 1.336$ , and 488 nm wavelength gives  $q \sim 0.0024 \text{ \AA}^{-1}$ .

For a given  $q$ , a time autocorrelation function  $g^2$  can be used to relate the intensity between time  $t$  and some arbitrary later time  $t + \tau$ , written as

$$g^2(\tau) = \lim_{T \rightarrow \infty} \frac{1}{T} \int_0^T I(t)I(t + \tau)dt \quad (2.8)$$

Note that the signal is independent of the initial time since the system is assumed to be ergodic, meaning that the time average is assumed to be equivalent to the ensemble average. The limits of the autocorrelation function are useful to consider. In the limit of small  $\tau$ , the autocorrelation function is at a maximum as the intensity becomes highly correlated. In the limit of large  $\tau$ , the intensity becomes uncorrelated (independent), and the autocorrelation function decays to a constant minimum. This decay in the autocorrelation function contains information about the diffusivities of particles in a solvent, which in turn contains information about the particle hydrodynamic size.<sup>14</sup>

The normalized autocorrelation function  $g^2$  is some function that decays from perfect correlation (i.e. a particle correlated with itself at a given instant) to no correlation at much later times. For a given light scattering setup, the autocorrelation function can be written in terms of the Siegert relationship as

$$g^2(q, \tau) = A + B|g^1(q, \tau)|^2 \quad (2.9)$$

in which  $A$  and  $B$  are fitting constants that are related to the baseline intensity as well as properties of the laser beam and detector optics. For general purposes, as is done here, each experimental correlation data are normalized between the baseline intensity value (large  $\tau$ ) and the maximum intensity value (small  $\tau$ ) such that  $A$  and  $B$  are unity for ease of comparison between samples. The important component of Eq. 2.10 is the constitutive relationship that describes the decay rate of the scattered intensity correlation ( $g^1$ ).

One common method to describe intensity decay rate is the cumulant method, or method of moments, that defines both an average decay rate and some variance in the decay rate. Using the relationship for the decay rate as  $\Gamma = q^2 D$ , in which  $D$  is the translational diffusion coefficient, the cumulant method gives

$$|g^1(q, \tau)| = \exp(-q^2 D \tau) \left( 1 + \frac{\mu}{2} \tau^2 + \dots \right) \quad (2.10)$$

in which the moments beyond the second have been neglected. This expression is referred to as the quadratic cumulant (QC) fit, and it contains both the average translational diffusivity as well as some polydispersity coefficient, defined as  $\sigma = \mu/(q^2 D)^2$ , that describes the width of the diffusivity distribution.

A second method is referred to as the double exponential (DE) fit. It can be written as the sum of two single exponential relationships as:

$$g^1(q, \tau) = A_1 \exp(-q^2 D_1 \tau) + A_2 \exp(-q^2 D_2 \tau) \quad (2.11)$$

in which the relative intensity weight coefficient  $A_i$  and diffusivity  $D_i$  are written for two separate particles. Here, the subscripts correspond to the smaller particle (1) and larger particle (2). In this case, the distribution is assumed to be two discrete sizes with no polydispersity coefficient or width to each distribution. Note that the weighting coefficients  $A_1$  and  $A_2$  are nonlinear functions of their respective decay rate,

but here their sum is equal to unity based on the normalized data. In other words, the weighting coefficients do not reliably account for the true shape of the distribution.

The third method investigated here is the polydisperse double exponential (PDE) fit, which is essentially a combination of the QC and DE fits, such that there are two distributions each with an average and variance. The PDE fit is written as

$$g^1(q, \tau) = A_1 \exp(-q^2 D_1 \tau) \left(1 + \frac{\mu_1}{2} \tau^2\right) + A_2 \exp(-q^2 D_2 \tau) \left(1 + \frac{\mu_2}{2} \tau^2\right) \quad (2.12)$$

in which any higher moments have been neglected.

The three methods described above provide a way to fit the decay rate and the relation to particle diffusivity. For small particles in dilute solution (non-interacting particles), the tracer and mutual diffusion coefficient approach the same limit, given by the Stokes-Einstein relation

$$D_i = \frac{k_B T}{6\pi\eta_0 R_{h,i}} \quad (2.13)$$

in which the solution temperature  $T$  and solvent viscosity  $\eta_0$  are known. Thus, by fitting the intensity-weighted distribution of diffusion coefficients  $D_i$ , the effective hydrodynamic diameter  $D_h$  or radius  $R_h$  can be related to the measured intensity fluctuations. Note that the effective hydrodynamic radius is determined from an intensity-weighted decay constant (i.e.  $R_h$  is related to the z-average that follows as  $\sim R^6/R^5$ ), demonstrating that even a small number of larger particles or contaminants can significantly shift the effective  $R_h$ .<sup>15</sup>

For solutions containing dilute, non-interacting spherical particles, DLS provides a quick and accurate method to determine an effective particle size. In particular, DLS provided a useful method to track micelle growth or decay as a function of agitation time.

DLS experiments were performed using a Brookhaven Instruments Light Scattering System (BI-200SM, Brookhaven Instruments Corporation, BIC) equipped with either a Lexel Laser (488 nm) or a CNI Laser (532 nm). Angle was controlled with a goniometer, and for all data presented here the scattering angle was 90°. All DLS experiments were performed at  $25.0 \pm 0.1^\circ\text{C}$ . Polymer solutions were pipetted into a 1 mL Wattman glass vial, sealed with a Teflon cap and parafilm, and placed into the temperature controlled decalin bath (matched refractive index of glass). The decalin bath was filtered for 5 min prior to experiments to remove dust, and polymer solutions were equilibrated within the temperature bath ( $\sim 3$  min) prior to recording data. Depending on the laser and the power input, the typical count rate was set between  $\sim 100$  and 400 kcps, with the measured and calculated baseline ratio within  $\pm 0.1\%$ . Data were analyzed and fit with the instrument software supplied by BIC. Analysis and fitting can be accomplished through MATLAB or procedures in IGOR Pro.<sup>16</sup>

### **2.3.2 Cryogenic transmission electron microscopy (cryo-TEM)**

Cryo-TEM techniques provide unique structural information of solution assemblies that have been vitrified as opposed to particles that have been dried out and deformed on a surface. In general, electron microscopy instruments are comparably much more expensive, scarce, and challenging to operate than DLS instruments. Experiments require considerable time, more expensive resources, and technical training. Despite these setbacks, cryogenic electron microscopy currently is the primary method to provide detailed real-space information of particles in a hyper-quenched solution environment. Other techniques such as liquid-cell electron microscopy are currently unable to deliver sufficient contrast and time resolution to

provide comparable structural detail of soft materials.<sup>17</sup> While cryo-TEM can provide high-resolution 2D projections of solution assemblies and 3D reconstructions, the technique has poor sampling statistics compared to scattering methods. Sample preparation can bias particle distributions and even alter the resulting solution assembly, for example, by rupturing vesicle structures with the blotting process. Therefore, microscopy and scattering methods become more powerful when used in combination.

Figure 2.6 shows a labeled schematic of an electron microscope as well as the actual instrument used in subsequent experiments. In general, a sample is composed of some spatial distribution of atoms or molecules and will scatter incident electrons to a varying degree based on the inherent electronic cross-sections. Electrons that do not scatter will transmit through the sample to produce an array of detector counts or “gray values” that together produce an image. Particular sections of the sample with higher electronic cross-sections scatter more of the incident electrons (e.g. heavy metal atoms, crystalline, or dense materials) and thus appear “darker” in a particular image because lower collected counts in that x-y position. Certain apertures can provide better contrast by physically blocking some scattered electrons. Note that the schematic is a gross simplification and only highlights basic user-end features.

Imaging was performed on a Tecnai G2 12 Twin TEM operating at 120 kV. Images were recorded using a Gatan CCD camera at a nominal underfocus (defocus typically  $\sim 1\text{-}10\ \mu\text{m}$ ) to enhance phase contrast, unless the gray value profile was desired (defocus  $\sim 0\ \text{nm}$ ). The temperature of the sample probe was maintained between  $-176\ ^\circ\text{C}$  and  $-180\ ^\circ\text{C}$  using liquid nitrogen. With a given beam spot size (2)

and low electron dose, noticeable sample damage due to interactions of the electron beam was observed after ~ 30-60 min.

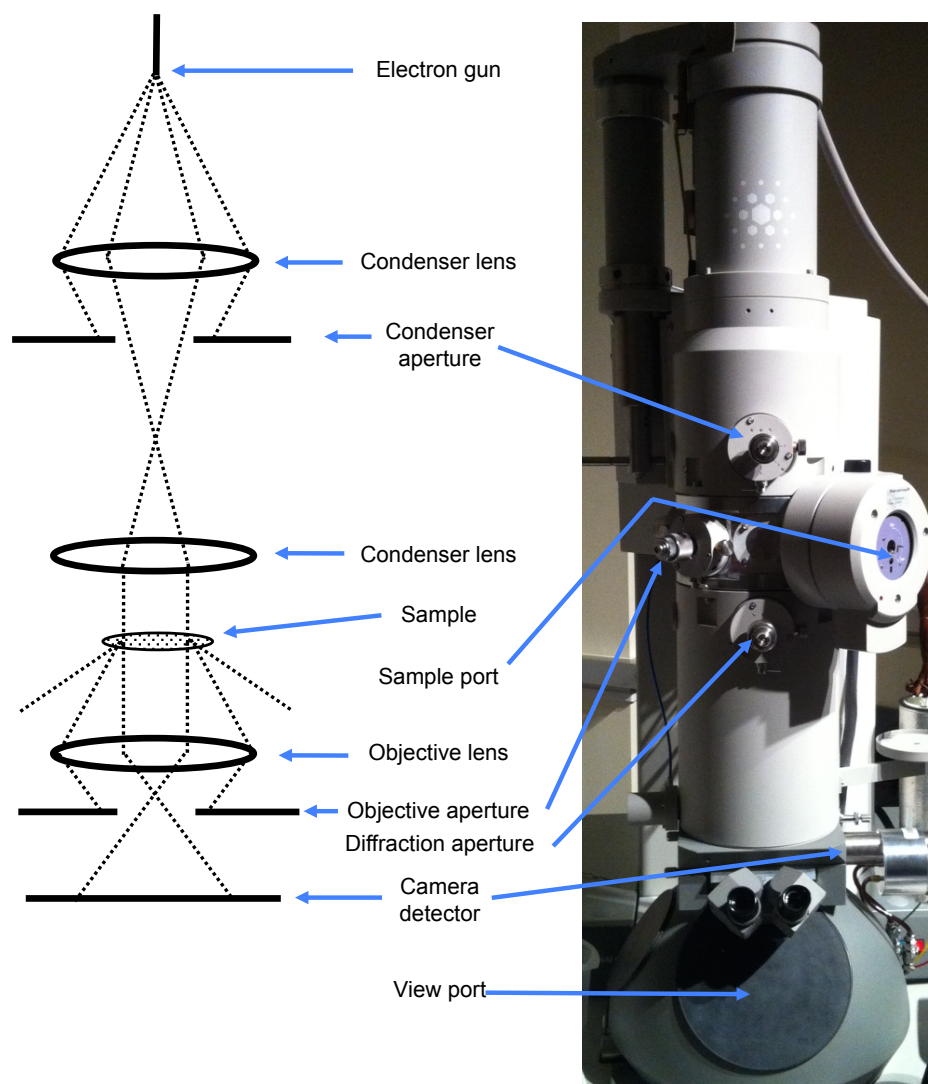


Figure 2.6. Schematic of transmission electron microscope (left, not to scale) and picture of FEI Tecnai G2 twin instrument (right).

In brief, samples were prepared using an FEI Vitrobot at 22 °C and relative humidity of 100% to control sample evaporation within the chamber. Prior to sample loading, carbon-coated copper TEM grids (Quantifoil R 2/1 or Quantifoil S 7/2) were plasma cleaned for 60 s. A 3  $\mu$ L drop of micelle solution was pipetted onto the grid inside the sample chamber. Using an automated system, the grid was blotted with filter paper twice to remove the excess solution. The number of blots (2), blot offset or force (0), blot time (3 s), wait time (1 s), and drain time (1 s) were consistent for each sample. In general, a longer blot time, greater number of blots, or longer drain time will lead to thinner ice thickness and vice versa. The listed conditions were found to work for dilute polymer solutions in water, but other solvents with varying viscosities would require adjustments. After blotting, grids were submerged in liquid ethane to vitrify the sample. Liquid ethane near its freezing point (-183 °C) is commonly used for good heat transfer and to avoid the formation of an insulating gas layer around the grid (Leidenfrost effect).<sup>18</sup> Vitrified samples were stored in liquid nitrogen for less than 3 h prior to imaging. A detailed step-by-step sample preparation protocol can be found elsewhere.<sup>19</sup> Common artifacts of sample preparation are highlighted and discussed in Appendix B.

Sample layers with varying thickness of water-ice (i.e. hyperquenched, amorphous ice) occur as a result of sample preparation, as shown in Fig. 2.7. This thickness gradient can be advantageous depending on the length scale of the solution assembled material. Thicker layers provide more space for larger structures but also give lower contrast and potentially overlapping of structures. There is an optimal film thickness where a single layer of solution structures will pack together and provide a non-overlapping profile. A gradient in ice thickness occurs often within a single grid

section, leading to multiple layers of micelles that stack up near the thicker edge of the grid. Very thin layers of ice may be beneficial for very small or low contrast samples, but these very thin layers are more susceptible to damage and breaking during the process. The ability to visually and quickly distinguish the desired film thickness on a phosphorescent screen, shown in Fig. 2.7a, is critical given the time sensitivity.

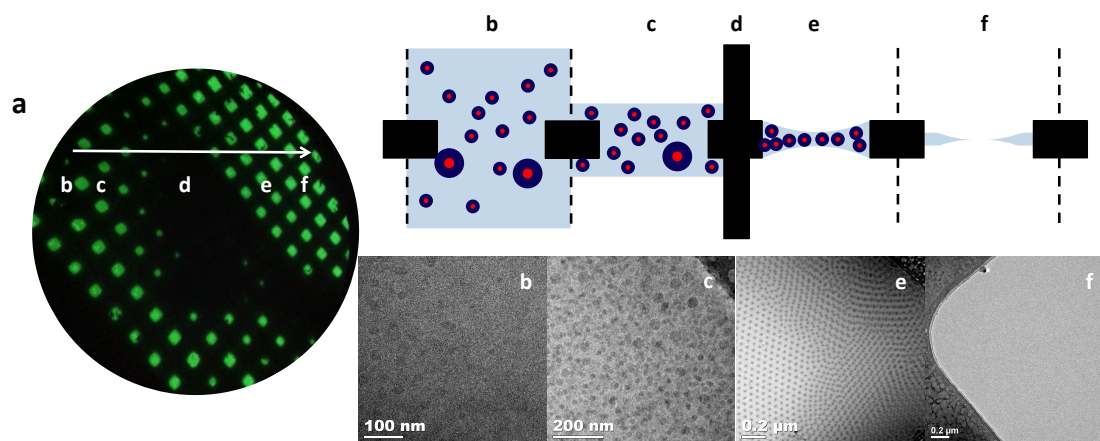


Figure 2.7. Cryo-TEM ice thickness gradients can lead to different particle distributions depending on the particle size. (a) Quick screening methods by visual inspection are critical, as impending sample damage due to incident electrons will occur over time. (b) Thick ice leads to low contrast compared to background or (c) significant micelle overlap. (e) Optimal thickness arises for when the ice thickness is comparable to the particle length scale. (f) Thin ice leads to quick melting or no contained sample.

Once a particular micrograph or image is captured, there are several methods to further analyze the image in order to extract additional information about contrast profiles and to quantify size scales. The subsequent sections describe methods to

extract gray value (contrast) profiles from an image, methods to count and bin multiple particles in an image, and methods for cross-sectional and FFT analysis.

Phase contrast can be neglected if images are taken in focus in which corrections to the contrast transfer function are negligible.<sup>20</sup> The enhancement of phase contrast through imaging at a nominal underfocus can be beneficial when high resolution is not necessary and when radial profiles are not of interest. For the amplitude contrast, the total electron scattering cross-section can be written as the sum of the elastic and inelastic cross-sections. The total transmission of electrons through the sample depends on the objective aperture, sample thickness, sample density, sample atomic number and weight, and the electron energy. In general, the image intensity as a function of the penetration depth distance ( $z$ ) passing through the sample can be given as<sup>20,21</sup>

$$\frac{I(z)}{I_0} = \exp\left(-\frac{z}{\lambda_z}\right) \quad (2.14)$$

in which  $I_0$  is the incident electron beam intensity and  $\lambda_z$  represents the mean free path length of the material. The mean free path is related to the total electron scattering cross-section of each atom (or sum of atoms that form a molecule) and the density. Intuitively, as the electron cross-section or the density increases, the mean free path decreases and the relative intensity decays faster with increasing penetration distance into the sample.

Written in terms of the distance parallel to the incident electron beam, the depth  $z$  can be related to a sphere of radius  $R$  as

$$z(r) = 2\sqrt{R^2 - r^2} \quad (2.15)$$

in terms of the distance  $r$  to the center of the particle ( $r = 0$ ).

The radial density for a hydrated corona layer  $\rho$  can be written as a linear combination of 2  $b$ -spline functions given as<sup>22</sup>

$$\rho(r) = \frac{\rho_1(r) + a\rho_2(r)}{1 + a} \quad (2.16)$$

in which  $a$  is a fitting constant and  $\rho_l$  is given as

$$\rho_1(r) = \frac{4(r - R_c - s)^3 - (r - R_c - 2s)^3}{4s^3} \quad \text{for } R_c \leq r < R_c + s$$

$$\rho_1(r) = \frac{-(r - R_c - 2s)^3}{4s^3} \quad \text{for } R_c + s \leq r < R_c + 2s \quad (2.17)$$

$$\rho_1(r) = 0 \quad \text{for } R_c + 2s \leq r$$

and  $\rho_2$  given as

$$\rho_2(r) = \frac{-(r - R_c - s)^3}{4s^3} \quad \text{for } R_c \leq r < R_c + s$$

$$\rho_2(r) = 0 \quad \text{for } R_c + s \leq r$$

in which  $R_c$  is the core radius and  $s$  is a fitting parameter that defines the profile width. These functions have been used previously to describe corona profiles for SAXS and SANS data analysis.<sup>23-27</sup>

The gray value  $G(r)$  is normalized with respect to the reduced transmittance due to scattering from surrounding hyperquenched water  $G_0$ . The gray value decreases with increasing  $r$  from (1) spherical geometry in a 2D projected plane and (2) the radial decay of the corona density. Combining Eqs. 2.14 - 2.17 gives

$$\frac{G(r)}{G_0} = \exp\left(-2K\rho(r)\sqrt{R^2 - r^2}\right) \quad (2.18)$$

in which the fitting constant  $K$  relates to the difference in the mean free path from the polymer and the surrounding vitrified water. Gray value profiles of micelles in different ice thicknesses can be normalized and scaled to one-another by assuming constant chain volume, equivalent density profile of the corona, and constant aggregation number  $Q$ , which together is written as

$$\int_0^R 4\pi \frac{G_0 - G(r)}{G_0} r^2 dr = Qv_c \quad (2.19)$$

in which  $v_c$  is the chain volume.

While the fit is rather involved and flexible through the incorporation of five fitting constants ( $K$ ,  $R$ ,  $R_c$ ,  $s$ , and  $a$ ), the function is able to provide profiles that are in good agreement with experimental data determined using SANS and cryo-TEM.<sup>22</sup> Figure 2.8 shows one example of experimental and fitted micelle profiles extracted from a cryo-TEM image (Fig. 2.8a) of amphiphilic poly(N-isopropylacrylamide) (PNIPAM) homopolymers in water. Assuming spherical symmetry from the particle center, individual particles were azimuthally integrated to provide better statistics using ImageJ software. The experimental corona profile (blue circles) agreed well with the profile fit in Eq. 2.19 (black line). For comparison, the profile for a homogeneous hard sphere of constant density is shown (red line). More elaborate core-shell models have also been validated using the same analysis on polystyrene-

PNIPAM particles, and these model predictions were in good agreement with profiles determined from small angle X-ray scattering.<sup>20</sup>

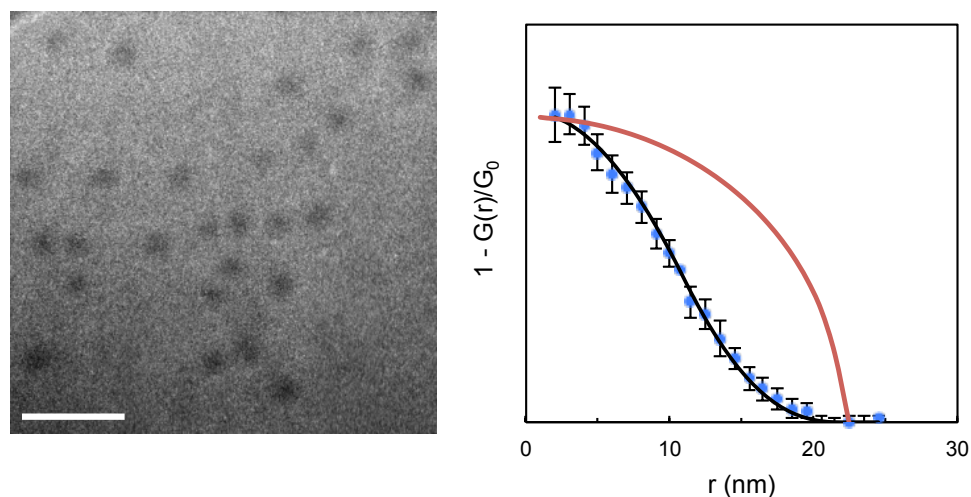


Figure 2.8. Method to extract volume fraction profiles from cryo-TEM images. Cryo-TEM image of micelles distributed in hyperquenched water (left) and the corresponding averaged radial profile of 50 micelles (right, blue circles). The empirical fit to the experimental profile for a star-like micelle (black line) and hard-sphere (red line) are shown for comparison. Scale bar is 100 nm. Figure reproduced with permission from *Macromolecules*, 46, 6319-6325 (2013).<sup>22</sup>

An alternative image analysis method was used to extract size distributions for multiple particles in a given image. For a distribution of particles in a flat ice layer, ImageJ software<sup>28</sup> was used to extract and bin particle cross-sectional areas, which were converted to particle radii or diameters by assuming that the particles were spherical. Image filters (Process > Noise > Despeckle and Process > FFT > Bandpass Filter) and thresholds (Image > Adjust > Threshold) were used to extract the particle areas (Analyze > Analyze Particles). A representative image analysis of PB-PEO

micelles (Day 4,  $10 \text{ mg mL}^{-1}$ , 40 wt% THF [equivalent to 43 vol% THF]) is shown in Figure 2.9.

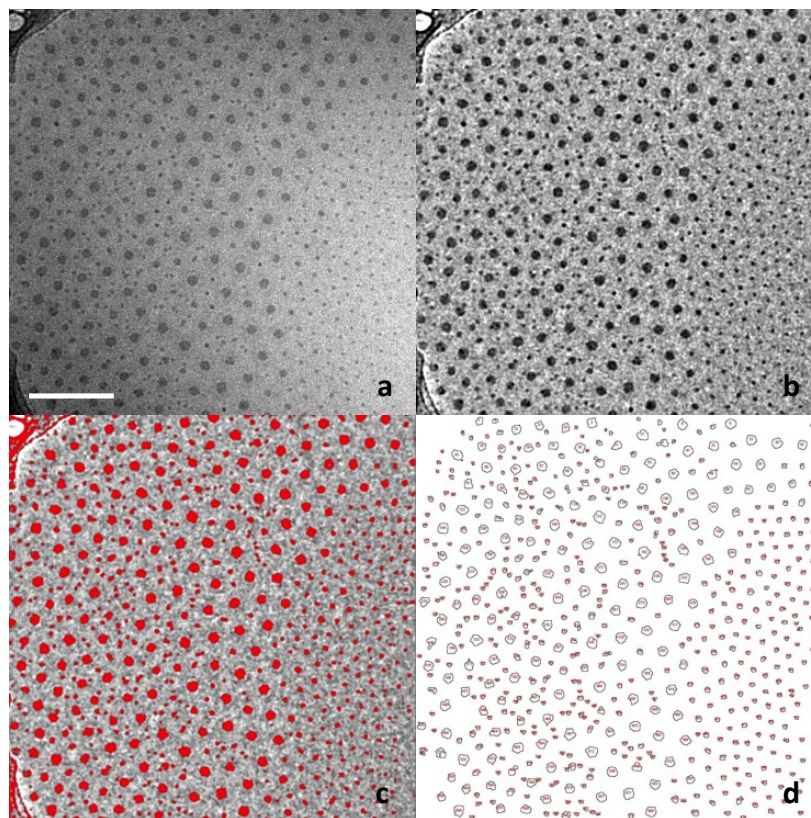


Figure 2.9. Image analysis method for counting the number of micelles with a given projected area. (a) Initial cryo-TEM image. (b) After despeckle and bandpass filtering. (c) After threshold selection to define particle areas. (d) After outlining particle areas using built in particle area routine using ImageJ. Scale bar is 200 nm. Figure reproduced in part with permission from *Nature Communications*, 5, 3599 (2014).<sup>10</sup>

An alternative method to approximate particle size is through line cross-sections or image Fourier transforms. These methods work best with highly ordered arrays, as demonstrated in Figure 2.10. Line cross-sections or transform tools are readily available within ImageJ software by using the straight-line tool (Analyze > Plot Profile) or fast Fourier transform tool (Process > FFT).

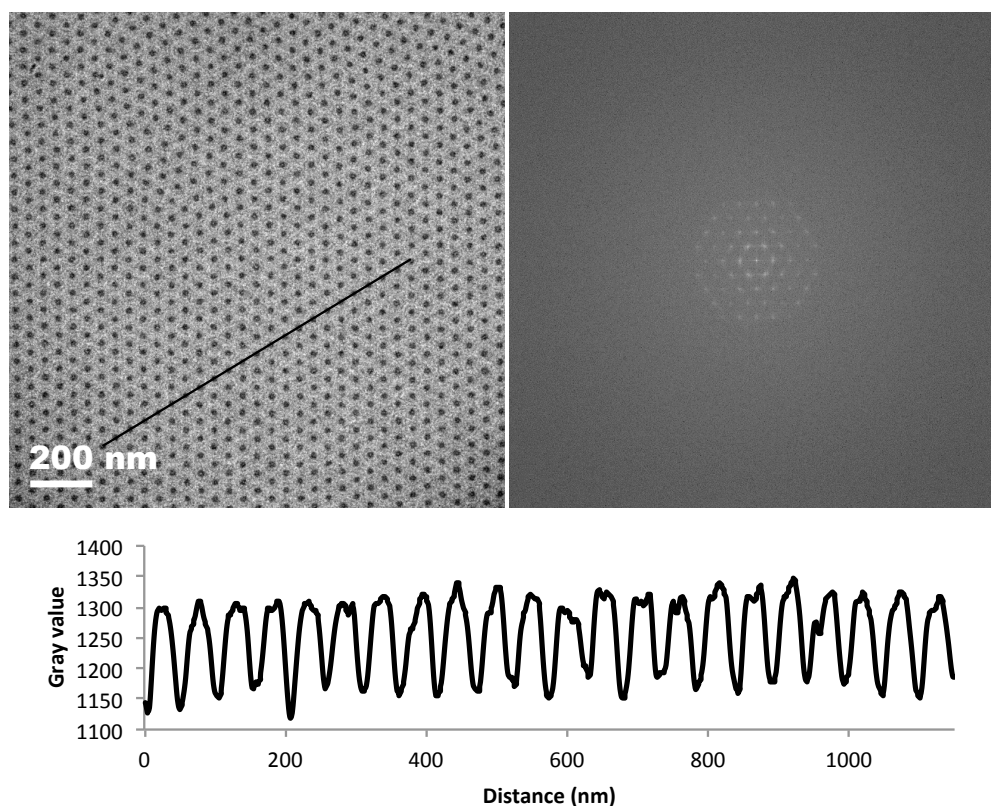


Figure 2.10. Cross-sectional analysis (left and bottom) for determining particle spacing and particle diameter. The Fourier transform of highly ordered arrays can also be used to determine particle spacing (right). The cryo-TEM image was taken 16 d after dialysis into water for PB-PEO micelles initially at 43 vol% THF and  $10 \text{ mg mL}^{-1}$ . Figure reproduced in part with permission from *Nature Communications*, 5, 3599 (2014).<sup>10</sup>

As shown in Figure 2.10, sample preparation for cryo-TEM can produce very thin layers of hyperquenched ice ( $< 100$  nm) and often induces hexagonal packing of micelles as an artifact of the preparation process. The center-to-center spacing determined by line cross-sectioning (black line, Fig. 2.10) was  $\sim 52$  nm, and the spacing determined from FFT was  $\sim 53$  nm. Both results are in agreement with the expected spacing based on the  $D_h \sim 50$  nm determined from DLS. However, the packing distance can be affected by grid preparation and other artifacts, as demonstrated in Appendix B.

### 2.3.3 Small angle neutron scattering (SANS)

SANS is regarded often as the “definitive” method for solution characterization, as it can provide quantitative structural information over multiple length scales. The flexibility to probe multiple length scales ( $\sim 10^{-2}$  to  $10^3$  nm), the excellent statistics that can be obtained by probing the entire sample volume, and the unique ability to selectively contrast-match structural components without intrusive labeling are currently unrivalled by other techniques. However, this increased level of understanding does not come without a significant cost. Few facilities exist with capable neutron sources, and access is competitive due to high demand. Another disadvantage is the inherent loss in phase information that presents an ill-posed problem for fitting experimental data with predicted real-space structures. This loss can lead to structural ambiguity that requires additional experimental designs and contrast-matching methods to distinguish between possible real-space structures (2.2.4).

SANS requires a well-aligned, coherent beam of neutrons to interact with a sample. Incident neutrons that interact and scatter from the sample produce an

intensity pattern that depends on the spatial arrangement of molecules within the sample. The basic premise in Figure 2.11 shows that incident neutrons can interact with the atomic nuclei within a sample of interest and scatter at a particular angle  $\Theta$ , or more commonly transmit directly through the sample with no interaction. In addition to the unique contrast-matching capabilities, neutrons are good probes for soft materials as they are highly penetrative and generally non-destructive as compared to X-rays techniques.

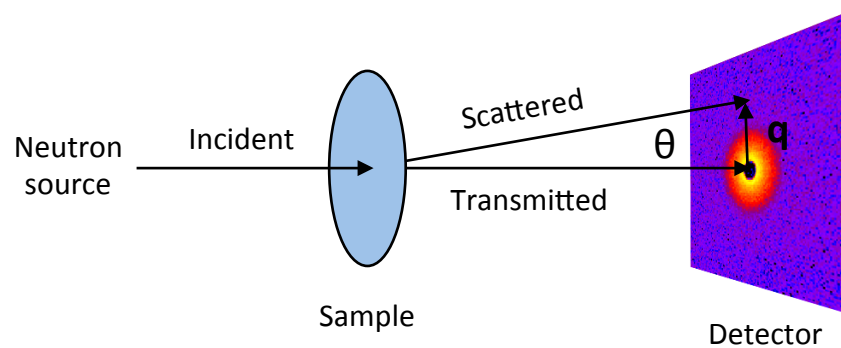


Figure 2.11. Simplified schematic of small angle neutron scattering (SANS). Incident neutrons either scatter once off of nuclei or transmit directly through the sample to the detector. The scattering pattern and angle of the scattered neutrons are related to the positions and compositions of the atomic nuclei within the sample. The difficulty in data fitting arises from the loss of phase information in the detected intensity.

To describe the measured intensity of scattered neutrons, the magnitude of scattered wavevector ( $q$ ) is defined as

$$q = \frac{4\pi}{\lambda} \sin\left(\frac{\theta}{2}\right) \quad (2.20)$$

in which  $\lambda$  is the neutron wavelength [ $\text{\AA}$ ], and  $\theta$  is the scattering angle. The wavevector  $q$  can be graphically shown in terms of the initial or incident wavevector  $k_i$  and the final or scattered wavevector  $k_f$ , as shown in Figure 2.12.

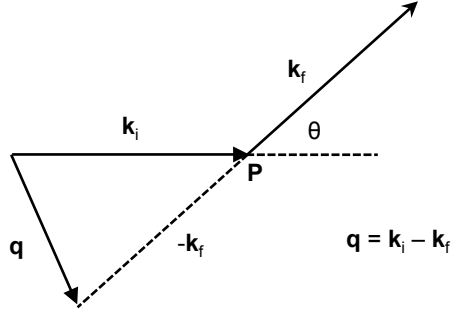


Figure 2.12. Definition of the elastic scattering wavevector ( $q$ ) in terms of the initial ( $k_i$ ) and final ( $k_f$ ) wavevectors. The magnitude of the scattered wavevector is given in equation 2.21, which is related to the scattering angle ( $\theta$ ) and neutron wavelength ( $\lambda$ ).

In elastic scattering experiments (i.e.  $|k_i| = |k_f|$ ), the measured intensity signal ( $I_{el}$  with units of  $\text{cm}^{-1}$ ) can be written as

$$I_{el}(q) = I_0(\lambda) \eta(\lambda) T(\lambda) \Delta\Omega \left( \frac{d\sigma}{d\Omega} \right)_{el} \otimes R(q) + B(q) \quad (2.21)$$

in which the incident beam intensity  $I_0$ , detector efficiency  $\eta$ , and transmission function  $T$  depend on the neutron wavelength. The subtended solid angle of a detector element is given as  $\Delta\Omega$ , while the convolution of instrument resolution function  $R$  and additional scattering from the background  $B$  can depend on the scattering vector.

Aside from the dependence of the overall sample composition on the transmission, the

important structure information of the sample is contained with the differential cross-section  $(d\sigma/d\Omega)_{el}$ .

The differential cross-section can be decomposed into two contributions, with one part relating to the form or shape characteristics of a scattering particle, referred to as the form factor  $A(q)$ , and the other part relating to the correlations in particle positions, referred to as the structure factor  $S(q)$ . Together, the differential cross-section can be written as

$$\left(\frac{d\sigma}{d\Omega}\right)_{el} \propto |A(q)|^2 S(q) \quad (2.22)$$

The structure factor approaches unity for dilute solutions, where the particle positions do not correlate with each other, leaving only the scattering contributions of form factor.

For  $N$  spherical particles of radius  $r_i$  per unit volume having a scattering length density (SLD) of  $\beta$  within a solvent having an SLD of  $\beta_0$ , the differential scattering cross-section per unit sample volume per solid angle is given as<sup>29</sup>

$$\left(\frac{d\sigma}{d\Omega}\right)_{el} = N \left(\frac{4\pi}{3}\right)^2 (\beta - \beta_0)^2 \int_0^\infty f(r_i) r_i^6 \left\{ \frac{3[\sin(qr_i) - qr_i \cos(qr_i)]}{(qr_i)^3} \right\}^2 dr \quad (2.23)$$

in which the term in curly brackets represents the form factor for a sphere, and  $f(r)$  is a function that describes the size distribution of spheres.

One commonly used model for polydispersity is the Schulz distribution, as it can be evaluated analytically. The normalized form used here for spheres of radius  $r$  is written as<sup>29</sup>

$$f(r) = \frac{1}{R_{avg}} \frac{(z+1)^{1+z}}{\Gamma(z+1)} \left(\frac{r}{R_{avg}}\right)^z e^{-(z+1)\frac{r}{R_{avg}}} \quad (2.24)$$

Notice that  $f(r)$  has units of inverse length, as it is normalized by the differential radius (i.e. the number density of particles having size  $r$  between  $R$  and  $R + dR$ ). The fit parameters are the average radius  $R_{avg}$  and the polydispersity term  $z$ , which is related to the variance of the distribution.

Equations 2.24 and 2.25 together describe a single distribution of spheres with an average radius and variance. For a bimodal distribution of spheres, which is used to describe micelle distributions later in Ch. 3, the equation can be written for two distributions ( $i = 1$  and  $2$ ) with their respective average radii, variances, SLDs, and numbers of spheres. To avoid the additional complexity of having to fit a core-shell form factor model, the micelle coronas were contrast-matched to the solvent. This was important to instill greater reliability in the fit using a bimodal Schulz distribution.

SANS experiments were performed on the NG-7 30 m SANS instrument at the National Institute of Standards and Technology, Center for Neutron Research (NCNR). An incident wavelength of 6.0 Å was used with sample-to-detector distances of 1 m, 4 m, and 13.5 m to cover a  $q$ -range from  $0.004 \text{ \AA}^{-1} < q < 0.4 \text{ \AA}^{-1}$ . Example  $q$ -ranges at various sample-to-detector distances are given in Appendix A (Figure A.2) as determined using SASCALC.<sup>29</sup> Measurements were performed at ambient temperature or at 25 °C. The data were reduced and analyzed in IGOR Pro using the standard procedures provided by NIST.<sup>29</sup>

#### **2.3.4 Flow small angle neutron scattering (flow-SANS)**

Neutron scattering can be performed on a flowing sample to probe the effects of shear on the particle structure, particle alignment with the flow fields, and spatial correlations.<sup>30</sup> The influence of shear flow micelle stability was important in

understanding the size evolution and chain exchange mechanisms of highly amphiphilic block polymers in aqueous solutions (Ch. 3-5).

The same scattering principles described for neutron scattering experiments on quiescent samples (2.3.3) can be applied to a flowing sample within a Couette device as shown in Figure 2.13. The Couette cell consists of a cup-and-bob geometry with a thin gap of fluid sample between the cup and bob (0.5 mm gap, 1.0 mm sample pathlength) that is aligned within the neutron beam. The titanium inner bob (OD = 29 mm) rotates at a defined rate using a stress-controlled rheometer (Anton Paar MCR 501), while the titanium outer cup (ID = 30 mm) remains stationary. In this particular case, the incident neutron beam is normal to the 1-3 shear plane, which is perpendicular to the velocity and vorticity direction (parallel to the velocity gradient).

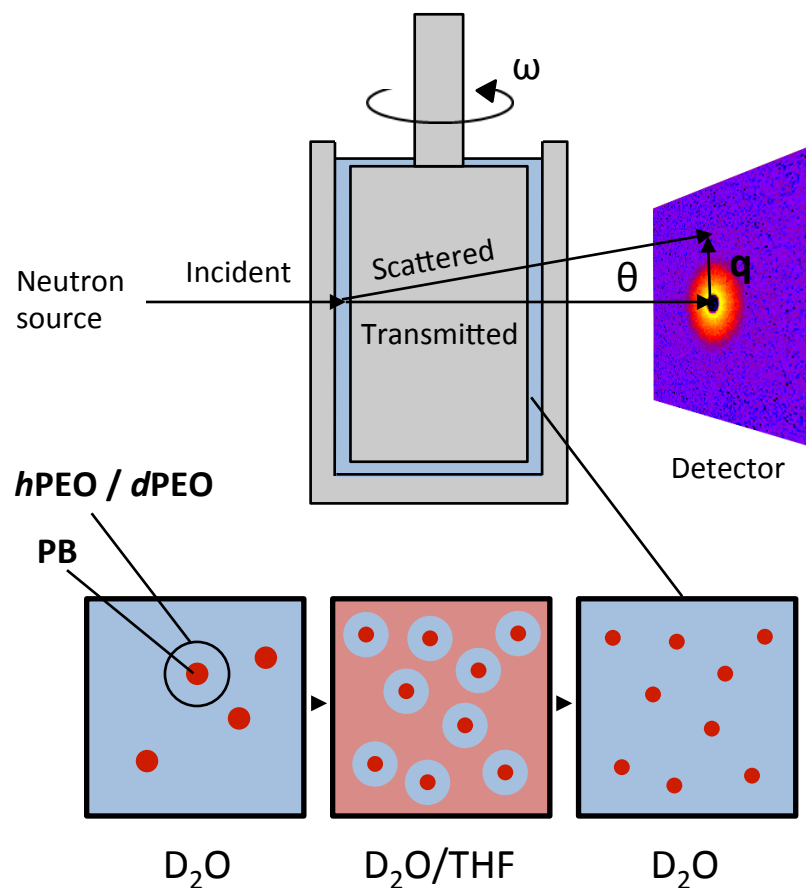


Figure 2.13. Flow-SANS is the incorporation of small angle neutron scattering within flowing environments. This method allows nanostructures to be probed in response to shear flow. Incident neutrons scatter from a sample (1-3 shear plane) flowing within concentric cylinders (Couette flow). Select features in the sample structure can be probed under flow using contrast-matching methods discussed previously.

Scattering data were collected both under steady shear (shear rates of  $3000 \text{ s}^{-1}$  to  $7000 \text{ s}^{-1}$ ) with a  $q$ -range  $0.007 \text{ \AA}^{-1} < q < 0.04 \text{ \AA}^{-1}$  and under static conditions ( $0 \text{ s}^{-1}$ ) with a  $q$ -range  $0.004 \text{ \AA}^{-1} < q < 0.4 \text{ \AA}^{-1}$ . To probe micelle growth under flow, blended corona samples (PB-*h*PEO/*d*PEO) were perturbed in THF cosolvent mixtures, prior to dialysis into pure  $\text{D}_2\text{O}$ , as shown in Figure 2.13. Additionally, a post-mixed solution

of PB-*h*PEO micelles and PB-*d*PEO micelles was sheared to investigate chain exchange between equal-sized micelles (Ch. 5). Scattering was isotropic (i.e. no particle alignment under flow was observed that would lead to anisotropic scattering), and thus the scattered intensity was azimuthally integrated and analyzed as described previously for quiescent samples. Sample temperature was controlled at 25 °C under steady shear and static conditions.

## **2.4 Solution Environment**

Methods to control the solution environment included adding and removing organic cosolvent, controlling temperature, and varying the type and rate of solution agitation. The previous section on solution preparation (2.2) described the methods to add and subsequently remove THF cosolvent using dialysis, which served as a way to perturb micelles from their favorable size in water in order to study relaxation kinetics. This section focuses on the other solution conditions, namely methods that controlled temperature (2.4.1), common mixing methods (2.4.2), and conditions for controlled flow (2.4.3). As will be shown in subsequent chapters, both the temperature and flow (agitation) of micelle solutions can have a significant impact on micelle chain exchange in aqueous solutions.

### **2.4.1 Temperature control**

Solutions were mixed or stored at ambient room temperature, which fluctuated between 20-25 °C ( $T_{\text{avg}} \sim 22$  °C). For micelle relaxation kinetics at specified temperatures, more controlled conditions were employed. Cold micelle solutions were magnetically stirred and maintained within a cold room (4 °C). Sealed vials containing micelle solutions were magnetically stirred in a sealed water bath, which

was surrounded by a temperature-controlled silicone oil bath. The concentric water and oil bath setup prevented oil contact on the glass sample vials, and the sealed water bath prevented water evaporation throughout prolonged experiments. The temperatures of the oil bath and water bath were controlled at 40 °C or 60 °C ( $\pm 1$  °C) using thermocouple feedback control (IKA RET Basic Magnetic Stirrer).

Continuous rapid vortex mixing for long periods caused frictional heating and a significant increase in solution temperature. Thus, rapid vortex mixing was performed in 2 min intervals with periodic equilibration ( $\sim 1$  min) using room temperature air or water between each 2 minute mixing interval (e.g. 5 min mix duration = 2 min mixing + 1 min equilibration + 2 min mixing + 1 min equilibration + 1 min mixing). The sample temperature fluctuated as a result of agitation and equilibration cycles but did not exceed 30 °C.

#### **2.4.2 Common mixing methods**

Micelle solutions were sealed with a Teflon-coated cap in a 2 dram vial (Kimble Chase, 17 x 60 mm, borosilicate glass) or 1 mL ampule (Wheaton, borosilicate glass). Magnetic stirring was performed using a Fisher Scientific Isotemp Stir Plate set at  $200 \pm 10$  rpm. For magnetically stirred solutions, 2 dram vials and 1 mL ampules contained Teflon-coated stirbars with dimensions 3 x 13 mm and 2 x 7 mm, respectively.

For nitrogen gas sparging, a 22-gauge needle was connected to a gas flow controller ( $10 \text{ mL min}^{-1}$ ) and the needle was inserted into the bottom of a micelle solution (2 mL in 20 mL glass vial) to induce gas bubbling for up to 60 min. The vial top was covered with parafilm to limit solvent evaporation. Solution mass was recorded before and after gas sparging such that the initial polymer concentration

could be restored, as needed, by the addition of fresh solvent (there was a small amount of solvent loss of  $\sim 24 \mu\text{L}$  over 60 min).

Rapid vortex mixing was performed with a Fisher Scientific Analog Vortex Mixer with cup head accessory [300-3200 rpm, 150V, 50/60Hz, 1.2A, 150 W, 4.9 mm orbit, and analog control dial settings range from 1 (low) to 10 (high)]. Unless otherwise stated, rapid vortex mixing was performed at the highest speed setting (dial setting 10,  $\sim 3200$  rpm). Micelle solutions (1 mL) were sealed in glass vials (Kimble Chase, 1 dram, 15 x 50 mm, rubber lined cap) and subsequently clamped and stabilized onto the mixer cup head. Mixing was performed over 2 min intervals to avoid significant frictional heating. The total mixing time was the sum of periodic intervals, as negligible chain exchange occurred over at least 19 d without mixing (Appendix A, Figure A.3). As a result of vortex mixing (and sparging), a foam was produced above the liquid surface, which was allowed to settle before transferring the sample to the SANS sample holder.

The mixing methods defined above are routine laboratory methods to induce flow. Due to the poorly defined geometry and presence of chaotic flow (e.g. eddies), the use of system volume average flow properties (e.g. shear rate, air-water regeneration rate, etc.) must be used for comparison. For example, the instantaneous shear rates near an air-water interface or near the tip of the stir bar can be significantly different compared to the shear rates near the vial wall. The volume averaged properties have been previously estimated using computational fluid dynamic models for common mixing procedures used in pharmaceutical research, such as magnetic stirring, orbital mixer, and vortex mixing.<sup>31</sup> While the experimental setup used in the literature reference is not identical to the mixing conditions presented in this work (i.e.

there were differences in vial diameter, stir bar diameter, air headspace, etc.), these simulated flow properties are useful for order-of-magnitude estimations (5.2.4).

### **2.4.3 Controlled flow conditions**

A rheometer with concentric-cylinder (Couette) or cone-plate flow geometries was utilized to produce more defined flows. Dilute micelle solutions ( $5 \text{ mg mL}^{-1}$  to  $10 \text{ mg mL}^{-1}$ ) were perturbed far from their near-equilibrium micelle size in water using the cosolvent addition/removal methods described previously. Use of an Anton Paar MCR series rheometer provided by NIST included a Couette geometry used for flow-SANS (2.3.4) as well as a cone-plate flow geometry ( $1^\circ$  angle between cone surface and plate) to determine feasible shear rates and timescales by using subsequent DLS analysis. Approximate loaded sample volume was  $\sim 3.5 \text{ mL}$  and  $\sim 0.5 \text{ mL}$  for the Couette geometry and cone-plate setup, respectively. Accessible shear rates between  $3000 \text{ s}^{-1}$  to  $7000 \text{ s}^{-1}$  for both geometries were expected to be on the same order as volume averaged shear rate obtained by rapid vortex mixing ( $\sim 10^3 \text{ s}^{-1}$ ).<sup>31</sup>

## REFERENCES

- 1 Won, Y.-Y., Brannan, A. K., Davis, H. T. & Bates, F. S. Cryogenic Transmission Electron Microscopy (Cryo-TEM) of Micelles and Vesicles Formed in Water by Poly(ethylene oxide)-Based Block Copolymers. *The Journal of Physical Chemistry B* **106**, 3354-3364 (2002).
- 2 Lu, J., Choi, S., Bates, F. S. & Lodge, T. P. Molecular Exchange in Diblock Copolymer Micelles: Bimodal Distribution in Core-Block Molecular Weights. *ACS Macro Letters* **1**, 982-985 (2012).
- 3 Hillmyer, M. A. & Bates, F. S. Synthesis and characterization of model polyalkane-poly(ethylene oxide) block copolymers. *Macromolecules* **29**, 6994-7002 (1996).
- 4 Terreau, O., Luo, L. & Eisenberg, A. Effect of Poly(acrylic acid) Block Length Distribution on Polystyrene-b-Poly(acrylic acid) Aggregates in Solution. 1. Vesicles. *Langmuir* **19**, 5601-5607 (2003).
- 5 Mai, Y. Y. & Eisenberg, A. Self-assembly of block copolymers. *Chemical Society Reviews* **41**, 5969-5985 (2012).
- 6 Meli, L. & Lodge, T. P. Equilibrium vs metastability: High-temperature annealing of spherical block copolymer micelles in an ionic liquid. *Macromolecules* **42**, 580-583 (2009).
- 7 Zhu, J. & Hayward, R. C. Spontaneous Generation of Amphiphilic Block Copolymer Micelles with Multiple Morphologies through Interfacial Instabilities. *Journal of the American Chemical Society* **130**, 7496-7502 (2008).
- 8 Meli, L., Santiago, J. M. & Lodge, T. P. Path-dependent morphology and relaxation kinetics of highly amphiphilic diblock copolymer micelles in ionic liquids. *Macromolecules* **43**, 2018-2027 (2010).
- 9 Peter Atkins, J. d. P., Ronald Friedman. *Quanta, Matter, and Change: A molecular approach to physical chemistry*. 339-340 (W. H. Freeman and Company, 2009).

- 10 Kelley, E. G. *et al.* Size evolution of highly amphiphilic macromolecular solution assemblies via a distinct bimodal pathway. *Nat. Commun.* **5**, 4599 (2014).
- 11 Roe, R. J. *Methods of X-Ray and Neutron Scattering in Polymer Science*. (Oxford University Press, 2000).
- 12 Lund, R., Willner, L. & Richter, D. Kinetics of Block Copolymer Micelles Studied by Small-Angle Scattering Methods. *Advances in Polymer Science* **259**, 51-158 (2013).
- 13 Zinn, T., Willner, L., Lund, R., Pipich, V. & Richter, D. Equilibrium exchange kinetics in n-alkyl-PEO polymeric micelles: single exponential relaxation and chain length dependence. *Soft Matter* **8**, 623-626 (2012).
- 14 Hiemenz, P. C. & Rajagopalan, R. *Principles of Colloid and Surface Chemistry*. Third edn, (CRC Press, 1997).
- 15 Thomas, J. C. The determination of log normal particle size distributions by dynamic light scattering. *Journal of Colloid and Interface Science* **117**, 187-192 (1987).
- 16 Schmitt, A. & Mahanthappa, M. Computer Code for Materials Scientists: Igor Pro Procedures for Analyzing Dynamic Light Scattering, Rheology, and Synchrotron X-ray Scattering Data. *figshare* (2013).
- 17 Proetto, M. T. *et al.* Dynamics of Soft Nanomaterials Captured by Transmission Electron Microscopy in Liquid Water. *Journal of the American Chemical Society* **136**, 1162-1165 (2014).
- 18 Danino, D. Cryo-TEM of soft molecular assemblies. *Current Opinion in Colloid & Interface Science* **17**, 316-329 (2012).
- 19 Grassucci, R. A., Taylor, D. J. & Frank, J. Preparation of macromolecular complexes for cryo-electron microscopy. *Nat. Protocols* **2**, 3239-3246 (2007).
- 20 Crassous, J. J. *et al.* Quantitative Analysis of Polymer Colloids by Cryo-Transmission Electron Microscopy. *Langmuir* **25**, 7862-7871 (2009).
- 21 Crassous, J. J., Ballauff, M., Drechsler, M., Schmidt, J. & Talmon, Y. Imaging the Volume Transition in Thermosensitive Core-Shell Particles by Cryo-Transmission Electron Microscopy. *Langmuir* **22**, 2403-2406 (2006).

- 22 Patterson, J. P. *et al.* Structural Characterization of Amphiphilic Homopolymer Micelles Using Light Scattering, SANS, and Cryo-TEM. *Macromolecules* **46**, 6319-6325 (2013).
- 23 Pedersen, J. S. & Gerstenberg, M. C. The structure of P85 Pluronic block copolymer micelles determined by small-angle neutron scattering. *Colloids and Surfaces a-Physicochemical and Engineering Aspects* **213**, 175-187 (2003).
- 24 Pedersen, J. S., Svaneborg, C., Almdal, K., Hamley, I. W. & Young, R. N. A small-angle neutron and X-ray contrast variation scattering study of the structure of block copolymer micelles: Corona shape and excluded volume interactions. *Macromolecules* **36**, 416-433 (2003).
- 25 Bang, J., Viswanathan, K., Lodge, T. P., Park, M. J. & Char, K. Temperature-dependent micellar structures in poly(styrene-*b*-isoprene) diblock copolymer solutions near the critical micelle temperature. *Journal of Chemical Physics* **121**, 11489-11500 (2004).
- 26 Choi, S. Y., Bates, F. S. & Lodge, T. P. Structure of Poly(styrene-*b*-ethylene-*alt*-propylene) Diblock Copolymer Micelles in Squalane. *Journal of Physical Chemistry B* **113**, 13840-13848 (2009).
- 27 Kelley, E. G., Smart, T. P., Jackson, A. J., Sullivan, M. O. & Epps, T. H. Structural changes in block copolymer micelles induced by cosolvent mixtures. *Soft Matter* **7**, 7094-7102 (2011).
- 28 Schneider, C. A., Rasband, W. S. & Eliceiri, K. W. NIH Image to ImageJ: 25 years of image analysis. *Nature Methods* **9**, 671-675 (2012).
- 29 Kline, S. Reduction and analysis of SANS and USANS data using IGOR Pro. *Journal of Applied Crystallography* **39**, 895-900 (2006).
- 30 Eberle, A. P. R. & Porcar, L. Flow-SANS and Rheo-SANS applied to soft matter. *Current Opinion in Colloid & Interface Science* **17**, 33-43 (2012).
- 31 Bai, G., Bee, J. S., Biddlecombe, J. G., Chen, Q. & Leach, W. T. Computational fluid dynamics (CFD) insights into agitation stress methods in biopharmaceutical development. *International Journal of Pharmaceutics* **423**, 264-280 (2012).

## Chapter 3

### BLOCK POLYMER MICELLE SIZE EVOLUTION

The size evolution of block polymer micelles in aqueous solutions was initially unexpected based on previously established work demonstrating that similar solution assemblies exhibited “frozen” chain exchange kinetics. Different mechanisms are proposed to explain the micelle growth by probing the solution assembly process through the use of complementary microscopy and scattering techniques. The figures and text presented in this chapter were reproduced in part with permission from *Nature Communications*, 5, 3599 (2014). Copyright 2014 Nature Publishing Group.

#### 3.1 Introduction

Bottom-up self-assembly provides a simple and tunable approach for creating various nanostructures in solution. Solution assemblies of well-defined nanostructures have attracted attention various applications including drug delivery, cosmetics, dispersant technologies, sensors, and nanoreactors. Many of these envisioned applications exploit solution assemblies as containers, where an outer polymer encapsulates and solubilizes molecular cargoes (e.g. dyes, reagents, or drugs), prevents aggregation, and hinders mass transfer of the cargo to the surrounding solution environment. These applications require a detailed understanding of the micelle exchange kinetics and stability of the self-assembly process in order to improve the efficacy by controlling the nanocarrier shape, size, and encapsulation of the desired cargo.

Amphiphilic block polymers are a promising material for these above-mentioned applications. Analogous to molecular surfactants, macromolecular surfactants assemble into various nanostructures in aqueous solutions including spherical and cylindrical micelles and vesicles, albeit on significantly different size and timescales. Furthermore, design parameters of block polymer assemblies in solution (i.e. size, morphology, surface functionality) can be tuned by controlling the polymer composition, molecular weight, and block chemistry. Importantly, the high molecular weight hydrophobic block gives rise to more robust mechanical properties, tunable membrane thickness and permeability, and kinetically trapped structures relative to liposome and surfactant assemblies.<sup>1</sup> The kinetic stability is especially beneficial for applications in drug delivery and nanoreactors, as the slow exchange of polymer chains between assemblies improves the retention time of the entrapped cargoes.<sup>2</sup> However, these slow dynamic processes often result in ambiguous path-dependent self-assembly and complicate the understanding of their long-term stability.

Previous works have shown that several block polymer systems are ‘frozen’ when dispersed in aqueous solutions with no measurable dynamics processes taking place over days or even months.<sup>3</sup> To facilitate the equilibration of highly amphiphilic polymers, many preparation methods exploit cosolvent mixtures, which significantly lower the energetic barrier to chain exchange. In these approaches, the polymer is molecularly dissolved in a common solvent for both blocks and a non-solvent for one of the blocks is added slowly, leading to self-assembly. When the solvent is only mildly selective for one of the blocks, the assemblies can exchange chains freely and maintain equilibrium; however, further addition of the non-solvent drastically increases the energetic barrier for chain exchange and hence kinetically traps the

structures.<sup>4-6</sup> Several groups have exploited this kinetically-controlled self-assembly to create more complex assemblies such as torroids<sup>7</sup> or patchy spheres.<sup>8</sup> Other cosolvent preparation methods are essential for loading hydrophobic cargoes into block polymer micelles, such as dyes or therapeutic agents for diagnostics and drug delivery applications. While cosolvent preparation methods are used widely throughout literature to prepare solution assemblies and to trap metastable structures, the stability of these assemblies upon removal of the cosolvent is generally overlooked.

This chapter demonstrates that dynamic processes can occur in block polymer micelles after cosolvent removal, even in highly selective solvents such as water, provided that the system is perturbed sufficiently far from the equilibrium size or aggregation number. In the absence of agitation, the micelles did not change size and appeared kinetically-trapped over months, consistent with scaling theories that predict large energy barriers to dynamic processes.<sup>9,10</sup> However, incorporation of gentle agitation (i.e. magnetic stirring), which was not considered in these scaling theories, led to an increase in the micelle size and aggregation number. Interestingly, the micelle sizes evolved through a bimodal distribution. These results provide detailed experimental evidence for a distinct bimodal size distribution of spherical micelles during a fusion controlled growth process, emphasizing the influence of common preparation conditions (e.g. cosolvent addition, dialysis, agitation) on the stability of the resulting block polymer assemblies.

### **3.2 Consequences of Cosolvent Removal**

The consequences of cosolvent removal on the dynamics of block polymer micelles were studied using a poly(butadiene-*b*-ethylene oxide) (PB-PEO) polymer in

THF/water mixtures. PB and PEO block molecular weights were  $3.2 \text{ kg mol}^{-1}$  and  $7.9 \text{ kg mol}^{-1}$ , respectively (B<sub>59</sub>O<sub>180</sub>). The low molecular weight and low glass transition temperature of the hydrophobic PB block allowed investigations into the micelle dynamics independent of entanglement or glassy effects in the micelle core.<sup>3,11</sup> (The classification of core block properties is highly significant when comparing dynamics of other block polymer systems). For example, completely different behavior was found following direct dissolution preparation procedures with PS-PEO in THF/water mixtures, which produced micelles with irreproducible sizes that would precipitate or phase-separate (see Appendix A, Fig. A.4).

PB-PEO micelles were prepared in water/tetrahydrofuran (THF) cosolvent mixtures using a method analogous to common drug-loading procedures (Section 2.2). To restate briefly, the polymer was dissolved in water and the resulting solution was stirred for 3 d, resulting in well-defined micelles with a PB core surrounded by a PEO corona. THF was added to reach the desired composition between 0 vol% THF and 50 vol% THF, and the solutions were stirred for an additional 3 d. The initial polymer concentration was  $2.4 \text{ mg mL}^{-1}$  (mass of polymer per volume of cosolvent solution). Adding the organic cosolvent improved the solvent quality for the core block and reduced the core-corona interfacial tension, leading to a decrease in micelle size as expected. Thereafter, the THF cosolvent was removed from the polymer solution by dialyzing against a large excess of pure water for 24 h. <sup>1</sup>H NMR confirmed that THF solvent was removed from the polymer solution (see Appendix A, Fig. A.5).

The following sections investigate the micelle size evolution in aqueous solutions following the cosolvent preparation process. Section (3.2.1) explores the dependence of solution agitation, while section (3.2.2) explores the effect of varying

initial THF content, as the presence of agitation and the extent of perturbation play a key role in the micelle relaxation process.

### **3.2.1 Dependence of solution agitation**

Following dialysis into pure water, micelles did not grow under quiescent conditions (Figure 3.1). This result was consistent regardless of the initial THF content in the cosolvent mixture and was consistent with scaling theories that predict large energy barriers to dynamic processes in macromolecular assemblies.<sup>10,12</sup> However, gentle agitation via magnetic stirring at 200 rpm, with estimated volume average shear rate  $\sim 20 \text{ s}^{-1}$ ,<sup>13</sup> led to distinct micelle growth depending on the composition of the cosolvent mixture.

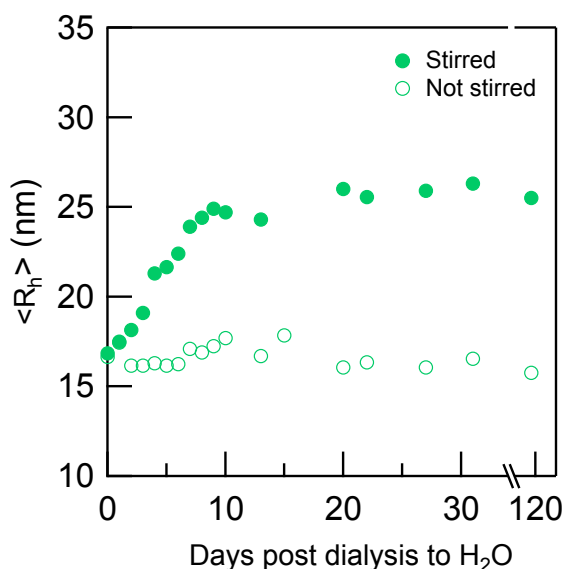


Figure 3.1. Effect of solution agitation on micelle size evolution. Magnetic stirring (200 rpm) leads to size evolution of block polymer micelles following cosolvent removal, as shown through an increase in the hydrodynamic radius ( $R_h$ ) following dialysis into water (0 to 120 d). Beginning from the same dialyzed stock solution ( $B_{59}O_{180}$ , 43 vol% THF,  $10 \text{ mg mL}^{-1}$ ), one sample was magnetically stirred at 200 rpm, while the control was not stirred (i.e. quiescent). No distinct changes in  $R_h$  were measured up to 120 d post dialysis in the absence of agitation. Variability in the fitted  $R_h$  determined from DLS using the quadratic cumulant fit was between 1 to 3 nm.

These results were surprising, as it was not clear how energy dissipation from fairly gentle agitation could overcome the large energetic penalty for chain exchange in water. This dependence on solution agitation hinted that the process was a shear-induced and/or interfacial phenomena, which is discussed later (3.3), and became the focus of further investigations presented in Ch. 4 and Ch. 5.

### 3.2.2 Varying initial THF/water content

To develop a better understanding of the driving force for the micelle size evolution, the initial amount of THF was varied to control the extent of perturbation from the presumed near-equilibrium size (i.e. the micelle size determined in pure water). Note that the “near-equilibrium size” found for these pure water/0% THF samples was inferred from the size reproducibility upon different pathways of micelle formation, such as through thin-film rehydration ( $\langle R_h \rangle \sim 32$  nm).

For polymer solutions that were agitated by magnetic stirring, there was an interesting behavior in the micelle growth that was dependent on the initial THF content, or in other words, there was a behavior that was dependent on how far micelles were perturbed from their desirable size in pure water. The average hydrodynamic radius ( $R_h$ ) of micelles prepared in cosolvent mixtures that contained  $\leq 10$  vol% THF remained constant over 90 d following THF removal, although these nanostructures were smaller than the micelles prepared in pure water (Fig. 3.2). This lack of size evolution suggested that those micelles were near equilibrium or unable to overcome the energetic barrier for rearrangement. The stability of micelles prepared from the pure water and low THF content solutions was consistent with reports indicating that PB-PEO micelles should be kinetically trapped in aqueous solutions due to the highly unfavorable PB-water interaction ( $\chi \sim 3.5$ ).<sup>3,11</sup>

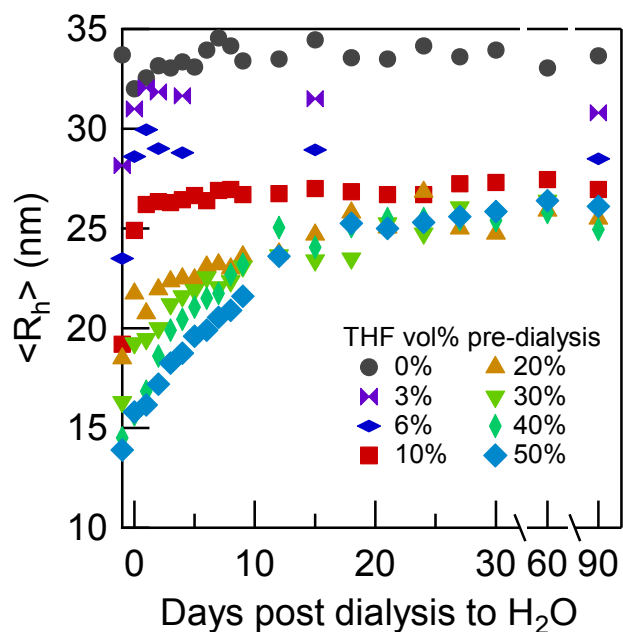


Figure 3.2. Varying initial THF cosolvent content prior to dialysis and subsequent solution agitation. DLS data provided the average hydrodynamic radius ( $R_h$ ) of PB-PEO micelles in water, and showed an increase in  $R_h$  over several days for samples at THF contents greater than 10 vol% THF. Fitted  $R_h$  values (quadratic cumulant method) varied between 1-3 nm.

In contrast, micelles prepared in cosolvent mixtures that contained  $> 10$  vol% THF exhibited significant size increases in the 20 d following THF removal. Micelles prepared from high THF content mixtures approached a similar final size of  $\langle R_h \rangle \sim 25$  nm following dialysis to water, regardless of the initial micelle size. Small angle X-ray scattering analyses (not shown) reinforced the trends seen in the DLS results and provided insight into changes in the micelle size dispersity following cosolvent removal. The disappearance and subsequent reappearance of a distinct peak in the scattering suggested an increase and subsequent decrease in size dispersity. This initial increase and subsequent decrease in dispersity suggested the presence of

multiple micelle populations during the growth process. Moreover, the final micelle sizes were similar for the specimens made from 10-50 vol% THF solutions, supporting the plateau in growth noted in the DLS results.

The micelle growth or lack thereof was reasonable on the basis of the free energy contributions that govern amphiphilic block polymer self assembly<sup>14</sup>. Larger micelles formed in low THF mixtures are closer to their equilibrium size and are unable to overcome the energetic barrier. In contrast, the smaller micelles formed in high THF mixtures have a larger interfacial area per chain than micelles formed in pure water, leading to highly unfavorable PB water interactions. A size increase of the smaller micelles reduces the interfacial area per chain and lowers the free energy of the system. Although free energy analyses suggested that micelle growth would be favorable, the kinetics of growth should remain imperceptibly slow when considering micelle growth mechanisms and their associated energetic barriers in highly amphiphilic systems.<sup>15</sup> These results possibly indicated new insights into block polymer micelle stability and prompted further investigation into possible mechanisms.

### **3.3 Probing Chain Exchange Mechanisms**

Complementary *in situ* characterization methods including DLS, cryo-TEM, and SANS were utilized to probe the chain exchange mechanisms leading to the unexpected micelle size increase in water. The following sections aim to distinguish between the commonly investigated mechanisms of micelle fusion/fission and single chain exchange (3.2.1), the implication of a bimodal distribution from cryo-TEM analysis (3.2.2), the occurrence of micelle chain exchange processes near equilibrium (3.2.3), and the concentration dependence (3.2.4). The general underlying mechanism

that coincides with the experimental evidence is micelle fusion/fission, although the growth appears to occur through a cooperative process (i.e. multiple micelles agglomerate simultaneously) instead of a process involving step-wise, two-body coalescence.

### 3.3.1 Micelle fusion/fission and single chain exchange

In general, two mechanisms are considered key for facilitating changes in micelle size and structure: single chain exchange and micelle fusion/fission. Single chain exchange involves the expulsion of a chain through diffusion of the insoluble core block into the bulk solution. The interfacial tension (i.e. surface energy between the hydrophobic core and water) is considered the largest energetic barrier in this process, and thus the energetic barrier should depend on  $\chi N$ . As the energy barrier only depends on the polymer degree of polymerization and solvent-polymer interactions, the process of single chain exchange does not depend on the micelle size. Near the equilibrium aggregation number, single chain exchange events are known to dominate the dynamics in both small molecule surfactant and block polymer micelles.<sup>4,6,9,16</sup> However, the energetic barrier to chain exchange in macromolecular systems normally is much higher due to the long-chain hydrophobic block, although this barrier is highly dependent on the solvent selectivity for the polymer blocks. Therefore, chain exchange events are imperceptibly slow in highly selective solvents yet occur readily in mildly selective solvents.<sup>3,6,16,17</sup>

The process of micelle fusion is dependent on the micelle aggregation number ( $Q$ ), with the fusion energetic barrier scaling as  $\sim Q_1 Q_2^{0.5}$  for a smaller micelle (1) and larger micelle (2).<sup>12</sup> Far from equilibrium, for example when the aggregation number is much smaller than the equilibrium aggregation number ( $Q_{eq}$ ), the dominant dynamic

process in macromolecular assemblies is debated.<sup>9,15,18-22</sup> Dormidontova used scaling analysis to suggest that fusion is the preferred growth mechanism in micelles in this regime, as opposed to the single chain events that are prevalent near equilibrium.<sup>12</sup> In contrast, other reports argue that the energetic barrier to deform the micelle coronas is too high to permit fusion in these systems, and therefore that only single chain events are favored.<sup>9,10</sup> Thus, despite the growing importance of understanding dynamics in macromolecular assemblies, the mechanisms governing structural evolution in highly perturbed systems remains unresolved.

### 3.3.2 Chain exchange near equilibrium size

SANS was employed to distinguish the role of single chain exchange or micelle fusion/fission mechanisms in the growth of PB-PEO micelles following solvent transfer into pure water. Specifically, single chain exchange in water was investigated using SANS by exploiting contrast variations and monitoring the changes in the scattered intensity over time (Sections 2.2.3 and 2.2.4). Initially, separate non-deuterated PB-*h*PEO micelles and deuterated PB-*d*PEO micelle solutions were prepared in an H<sub>2</sub>O/D<sub>2</sub>O mixture. These separate solutions were mixed at time  $t = 0$ , giving rise to a maximum in scattered intensity due to contrast between the coronas and solvent (Fig. 3.3 black circles). After mixing the PB-*h*PEO and PB-*d*PEO micelle solutions, two possible outcomes were considered. In the first scenario, chain exchange would occur, leading to randomization of the PB-*h*PEO and PB-*d*PEO chains within micelles. This mixing of the chains would reduce the corona/solvent contrast and decrease the scattered intensity, as the isotopic composition of the solvent was selected to contrast-match a 50/50 wt% (randomly mixed) *h*PEO/*d*PEO corona

(Fig. 3.3 open circles). In the second scenario, chain exchange would not occur, and the scattered intensity would remain nearly constant with time.

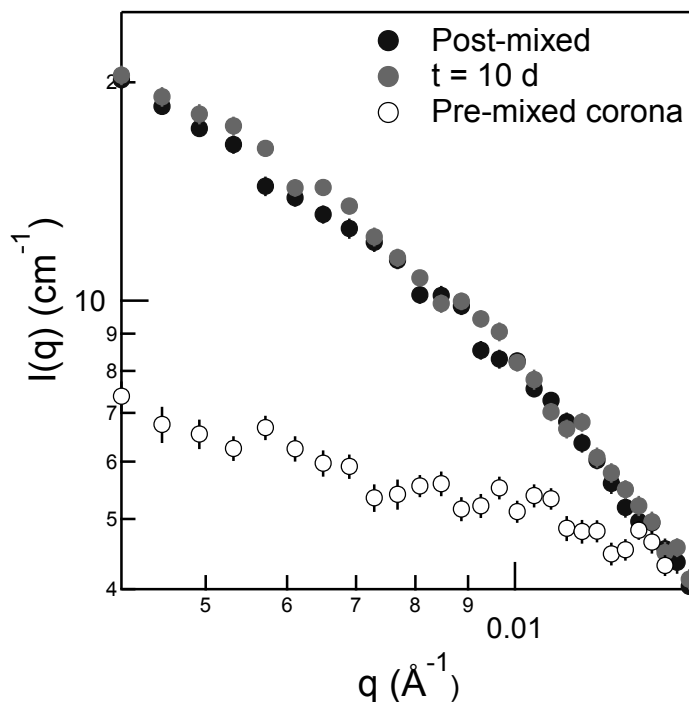


Figure 3.3. Determining chain exchange using SANS contrast-matching methods. The lack of change in scattered intensity for mixed PB-*h*PEO and PB-*d*PEO micelles (0 vol% THF) suggested negligible chain exchange occurred after 10 d. Error bars represent the standard deviation.

For this system, the scattered intensity did not decrease over 10 d while stirring the solutions (Fig. 3.3 gray circles), supporting the second scenario and a lack of appreciable chain exchange by micelle fusion/fission and/or single chain events. This lack of exchange found here is consistent with previous reports on the non-ergodicity of PB-PEO micelles in aqueous solutions and the highly unfavorable PB-water

interaction.<sup>3</sup> Recent reports have demonstrated that the energy barrier to single chain exchange only depends on the properties of the hydrophobic block and not on the micelle size/aggregation number.<sup>16,23</sup> Following this rationale, the results in Fig. 3.3 support that single chain exchange is highly unfavorable in this system and therefore did not to the micelle growth noted in Fig. 3.2. While this ruled-out the likelihood of single chains being expelled from the cores, quickly diffusing through solution, and then inserting into another micelle, it did not confirm the occurrence of micelle fusion/fission either. Further detailed structural studies with cryo-TEM and examination of the concentration dependence were necessary.

### 3.3.3 Bimodal size distribution from cryo-TEM

As single chain exchange was not prevalent, the fusion/fission mechanism was examined as an alternative description of micelle growth. To visualize the micelle growth, cryo-TEM was employed to follow the temporal evolution of a micelle solution (10 mg mL<sup>-1</sup> in 43 vol% THF) over a 21 d period following cosolvent removal. The resulting micrographs are shown in Fig. 3.4, in which the darker domains correspond to the dense PB cores while the fainter halos correspond to the PEO coronas.<sup>24,25</sup> Note that the hexagonal packing was an artifact of grid preparation (Appendix B.2). The core sizes were extracted from the images (Section 2.4), and the corresponding frequency histograms are given in Fig. 3.5. The core radii at Day 0 were described by a single and nearly monodisperse distribution with an average  $R_c \sim 5\text{-}6$  nm. Surprisingly, a second distinct distribution of core radii ( $R_c \sim 10\text{-}11$  nm) appeared after 1 d. The distinct bimodal distribution persisted throughout 10 d, with the population weighting shifting from the smaller to larger distribution over time. By Day 16 to Day 21, the core size distribution exhibited a single and more monodisperse

population ( $R_c \sim 10\text{-}11\text{ nm}$ ), consistent with the timescales determined from DLS (Fig. 2). This increase and subsequent decrease in size dispersity was consistent with similar trends determined from DLS and SAXS.

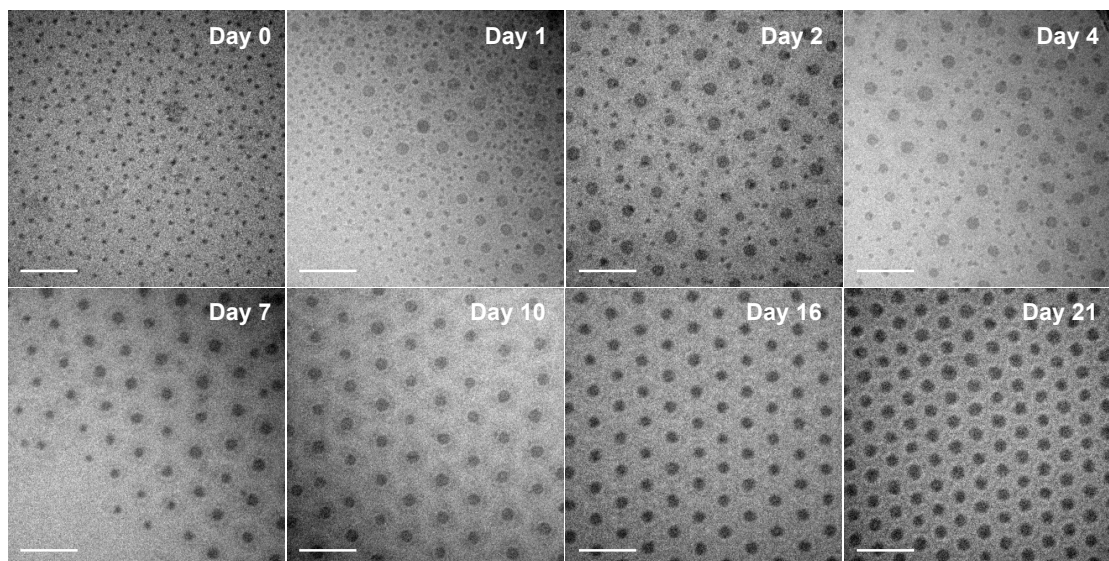


Figure 3.4. Progression of micelle growth through a bimodal pathway. Cryo-TEM analysis of PB-PEO micelles (43 vol% pre-dialysis,  $10\text{ mg mL}^{-1}$ ) in pure water following dialysis and stirring for 21 d. A distinct second distribution appears after 1 day and progresses to a monodispersed larger population near 10 d. Scale bars are 100 nm.

It is beneficial to examine particle distributions in terms of micelle volume, which is related to aggregation number. The second distribution corresponded to an approximate eight-fold increase in core volume or aggregation number from the initial distribution (for the 43 vol% THF sample). Relative frequency histograms of PB-PEO micelle aggregation numbers derived from the measured core radii ( $R_c$ ) for the  $10\text{ mg mL}^{-1}$ , 43 vol% THF samples are presented in Fig. 3.5. The micelle aggregation

number was estimated as  $Q = (4/3) \cdot \pi \cdot R_c^3 \cdot \nu_{PB}^{-1}$  by assuming that the micelle cores were perfect spheres and were composed only of PB. The PB chain properties used to estimate the PB chain volume ( $\nu_{PB} = 6 \text{ nm}^3$ ) included molecular weight  $M_n = 3.2 \text{ kg mol}^{-1}$ ; degree of polymerization  $N_{PB} = 59$ ; and bulk density  $\rho_{PB} = 0.87 \text{ g cm}^{-3}$ . The small and large micelle populations had average aggregation numbers of  $\sim 100$  and  $\sim 800$ , respectively, although the distribution of aggregation numbers for the larger population is much broader than the primary micelle distribution as seen in Fig. 3.6.

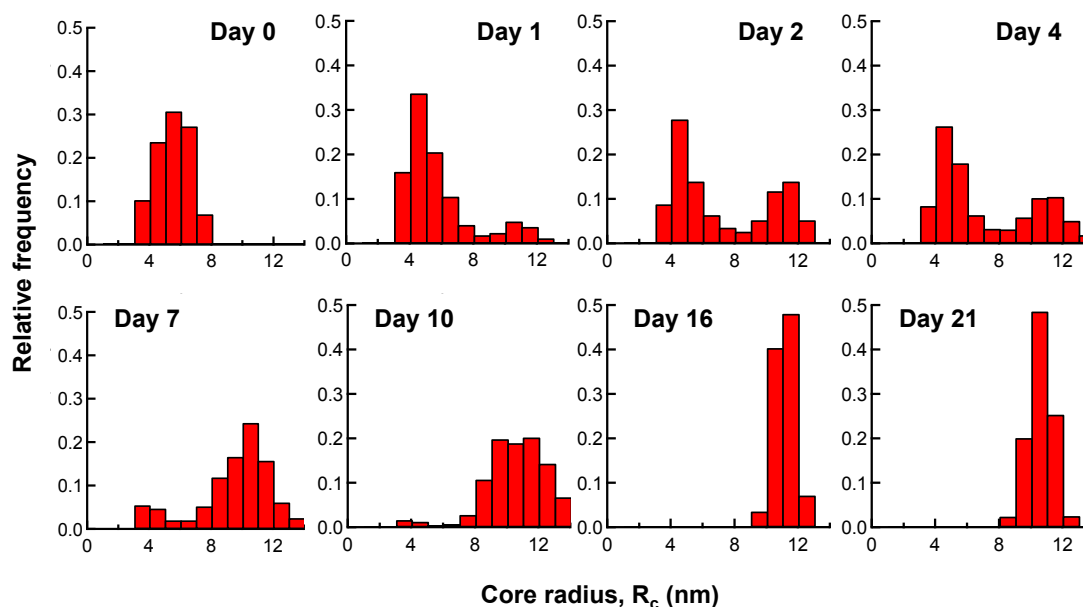


Figure 3.5. Distribution of micelle core radii from Cryo-TEM image analysis. The core distributions determined from Fig. 3.4 are plotted as relative frequency histograms for 21 d following dialysis to pure water. The primary distribution ( $R_c \sim 5\text{-}6 \text{ nm}$ ) and secondary distribution ( $R_c \sim 10\text{-}11$ ) are distinctly separated by a gap in micelles with intermediate core sizes ( $R_c \sim 8 \text{ nm}$ ).

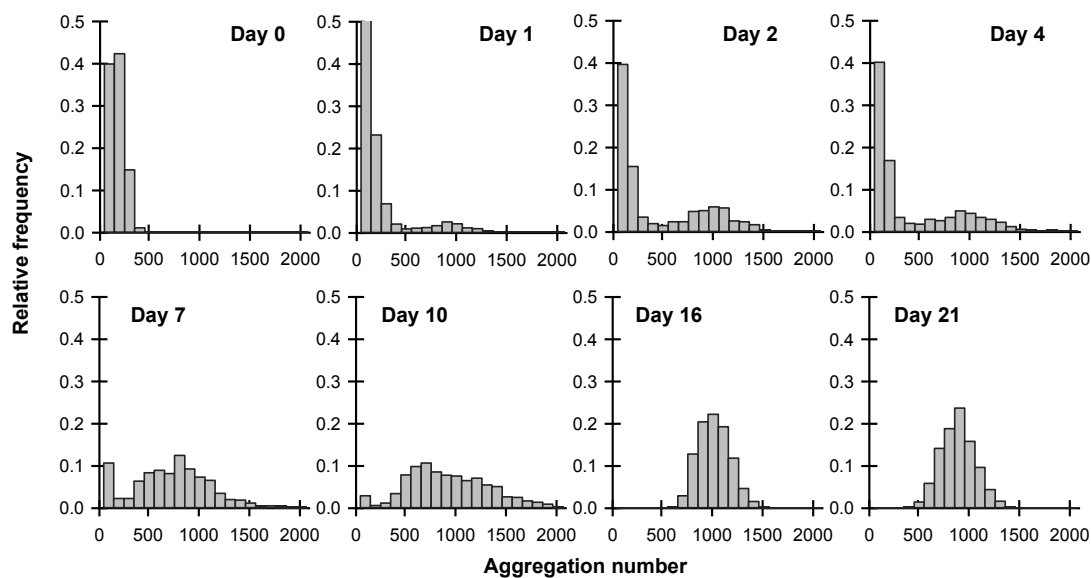


Figure 3.6. Aggregation number distributions determined from core radii shown in Fig. 3.5 (43 vol% THF sample). The initial micelles (day 0) were relatively monodispersed with aggregation numbers of  $\sim 100$ . The larger micelles had a broader distribution of aggregation numbers that was centered around  $\sim 800$ .

The energy barrier to micelle fusion is related to the corona chain stretching, and thus the barrier is expected to scale with aggregation number.<sup>12,21</sup> Accordingly, the fusion of intermediate sized micelles should be significantly slower than the fusion of two smaller micelles. Based on this scaling, distinct intermediate populations should exist if the micelles were growing by stepwise two-body collisions. This concept was demonstrated in computational work<sup>26</sup> that showed distinct multimodal size distributions for micelles undergoing stepwise fusion growth. In contrast, this behavior differs from that of micelles growing through single chain events, which was characterized by a shifting monomodal size distribution.<sup>27,28</sup> However, the bimodal distribution found here does not support either of these predictions, suggesting an

alternate fusion-controlled growth mechanism. The next section investigates the concentration dependence, which provides further evidence that the micelles grow through a fusion-controlled process.

### 3.3.4 Concentration dependence

Micelle fusion events are predicted to follow second-order kinetics based on two-body collision arguments. Following this basis, an increase in the growth rate with increasing micelle concentration is attributed to micelle fusion mechanism.<sup>21,26,29</sup>

The size evolution was examined as a function of micelle concentration using cryo-TEM, SANS, and DLS. Cryo-TEM images qualitatively suggested there was concentration dependence to micelle growth over 16 d (Fig. 3.7). In general, these micrographs suggested that the micelle growth rate increased with micelle concentration (2, 5, and 10 mg mL<sup>-1</sup>) by the appearance of a greater number of larger micelles at higher concentrations. Although microscopy provides unique structural insights, examined sample sizes for microscopy experiments are much smaller ( $\sim 10^3$  micelles) compared to sample sizes for light or neutron scattering experiments ( $\sim 10^{15}$  micelles). Furthermore, artifacts from grid preparation can easily bias the “random” sampling in microscopy techniques, which would invalidate any underlying distributions or statistics regardless of sample size. Thus, scattering techniques are necessary to probe the entire sample volume for comparison.

In the SANS experiments, the micelle coronas were contrast-matched to the solvent (D<sub>2</sub>O) by blending PB-*h*PEDO and PB-*d*PEDO polymers (88 wt% PB-*d*PEDO / 12 wt% PB-*h*PEDO), thereby allowing SANS to probe only the PB core size distribution. The scattering curve showed a marked difference in micelle populations for the various sample concentrations (Fig. 3.8 points). The distinct maximum and

minimum in the 5 mg mL<sup>-1</sup> and 10 mg mL<sup>-1</sup> scattering curve indicated that micelles were fairly monodispersed in the higher concentration samples and were located at approximately the same  $q$  values. These data supported that the larger micelles were the same size ( $R_c \sim 10$  nm) in both samples. Meanwhile, the 2 mg mL<sup>-1</sup> sample showed no distinct maximum or minimum  $q$ , suggesting that either the sample had higher dispersity or the superposition of the scattering from the bimodal distribution smeared out these distinguishing features.

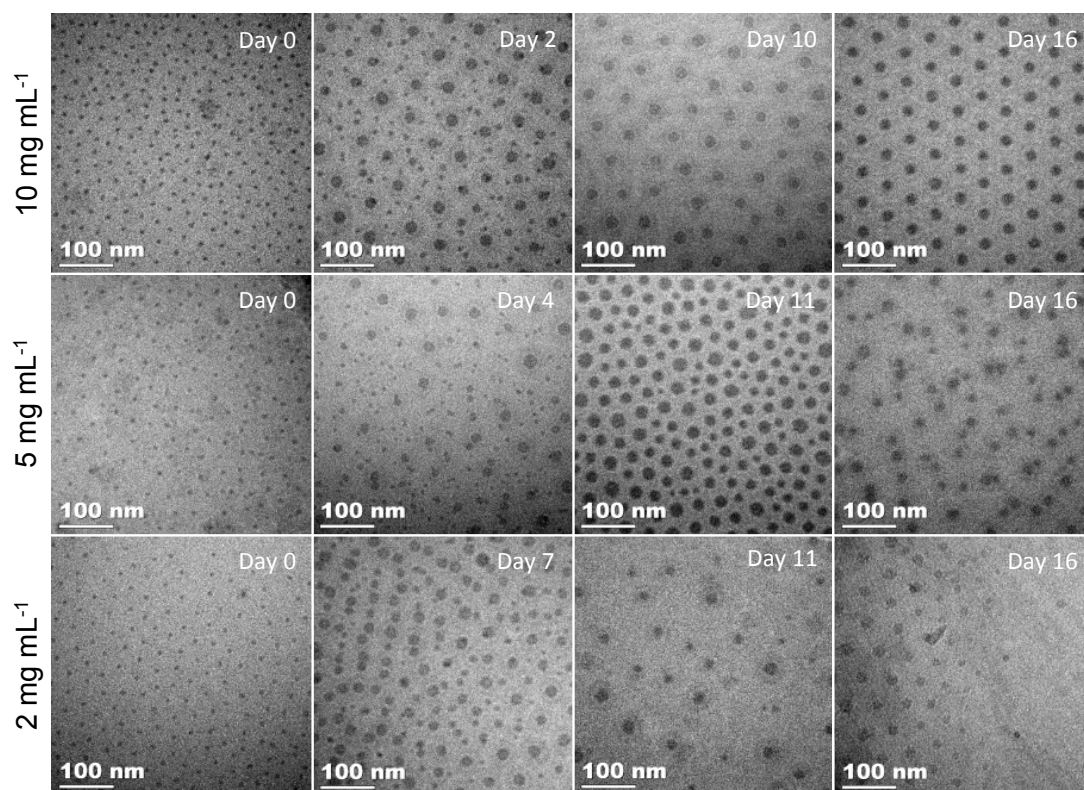


Figure 3.7. Micelle size evolution as a function of concentration. Cryo-TEM images of PB-PEO (43 vol% pre-dialysis) at different initial concentrations qualitatively suggested that lower concentrations led to slower micelle growth rates. This conclusion was supported by the presence of smaller micelles at day 11 and day 16 for the  $2 \text{ mg mL}^{-1}$  and  $5 \text{ mg mL}^{-1}$  samples, and nearly monodispersed larger micelles at day 10 and day 16 for the  $10 \text{ mg mL}^{-1}$  sample.

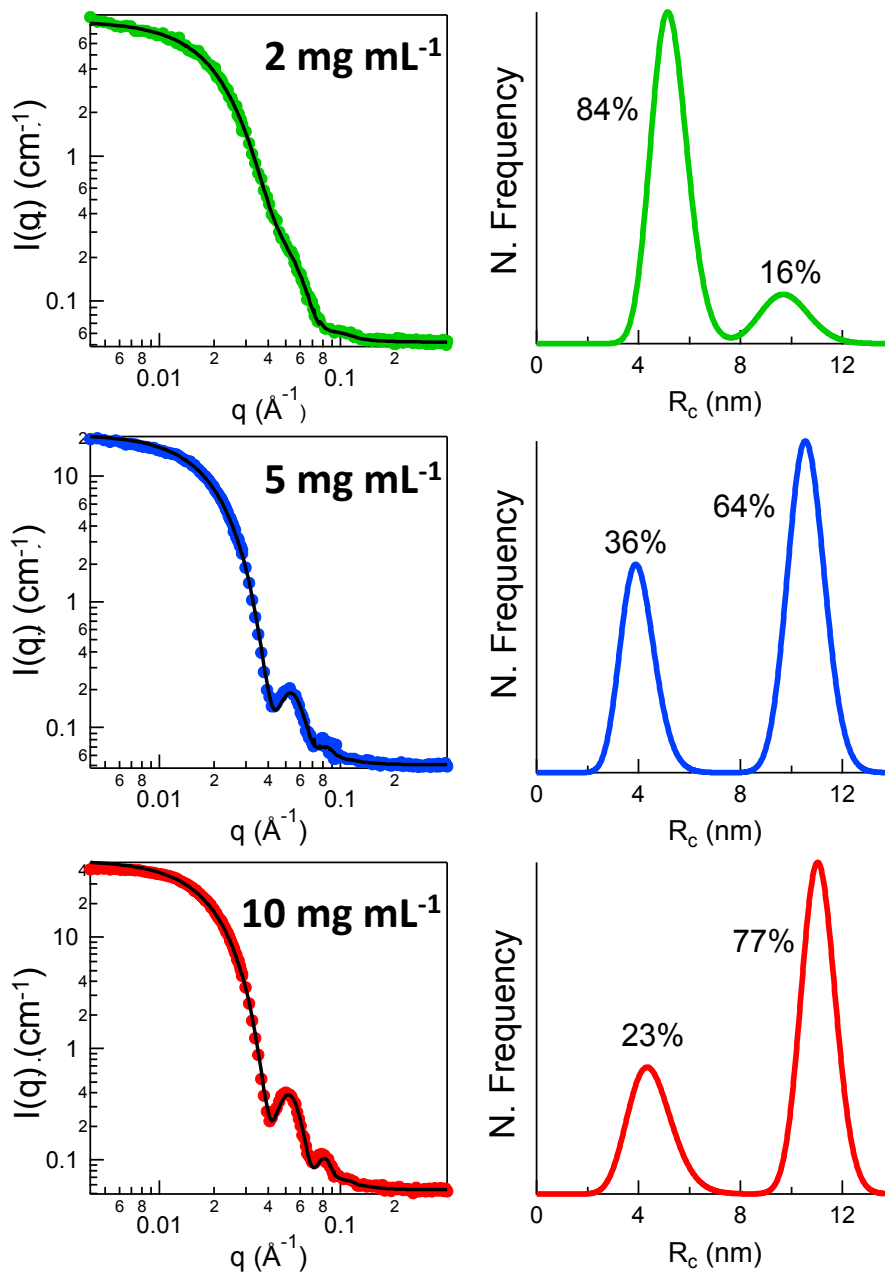


Figure 3.8. Bimodal distribution and concentration dependence determined from SANS. A bimodal Schulz distribution of spheres provided a better fit to corona-matched PB-PEO micelles compared to a fit using a single broader Schulz distribution. Increasing polymer concentration led to a shift toward larger micelle populations after mixing for 11 d (43 vol% THF prior to dialysis). The bimodal distribution and concentration dependence suggested a fusion/fission chain exchange mechanism.

These trends were substantiated by modeling the data using a bimodal distribution of Schulz spheres, which resulted in significantly better fits than the model for monomodal spheres, as shown in Appendix A (Figure A.6). The resulting bimodal fits to the SANS data (Fig. 3.8 black lines, left) and corresponding number frequency distributions of core radii (Fig. 3.8 right) are presented for the different polymer concentrations. The bimodal core distribution with maxima centered at  $R_c \sim 5$  nm and  $\sim 10$  nm was in good agreement with the cryo-TEM results. Additionally, the SANS results indicated that the relative weighting of the larger to smaller micelle core population increased with increasing polymer concentration, again supporting the fusion mechanism for micelle growth. The most distinguishing feature that was captured by the fit of the bimodal distribution of spheres involved the slight shoulder at mid- $q$  for the  $2 \text{ mg mL}^{-1}$  data (Fig. 3.8  $q \sim 0.04$  to  $0.08 \text{ \AA}^{-1}$ ). This shoulder in the scattering curve was due to the superposition of the two distinct core distributions and would not exist for dispersed monomodal distributions.

Although cryo-TEM and SANS techniques together provided excellent structural and statistical detail, the methods were inherently time and resource intensive. Meanwhile, light scattering methods were much less time intensive and more accessible. Consequently, it was of interest to determine if DLS could monitor concentration dependent micelle growth and distinguish between monomodal and bimodal micelle size distributions.

Results from the DLS concentration study are given in Fig. 3.9. Micelles were prepared in water/tetrahydrofuran (THF) cosolvent mixtures at various initial THF contents (vol%). The polymer concentrations prior to dialysis were  $1 \text{ mg mL}^{-1}$  and  $10 \text{ mg mL}^{-1}$ . The DLS data were fit with the quadratic cumulant method, and the fits

indicated that changes in the hydrodynamic radii ( $R_h$ ) occurred over a comparable time frame for the different concentrations. DLS experiments could not definitely confirm the concentration dependence determined by the cryo-TEM and SANS analyses. The reason for this discrepancy is related to the large uncertainty in the fitted intensity-weighted distributions, as discussed further in the following section.

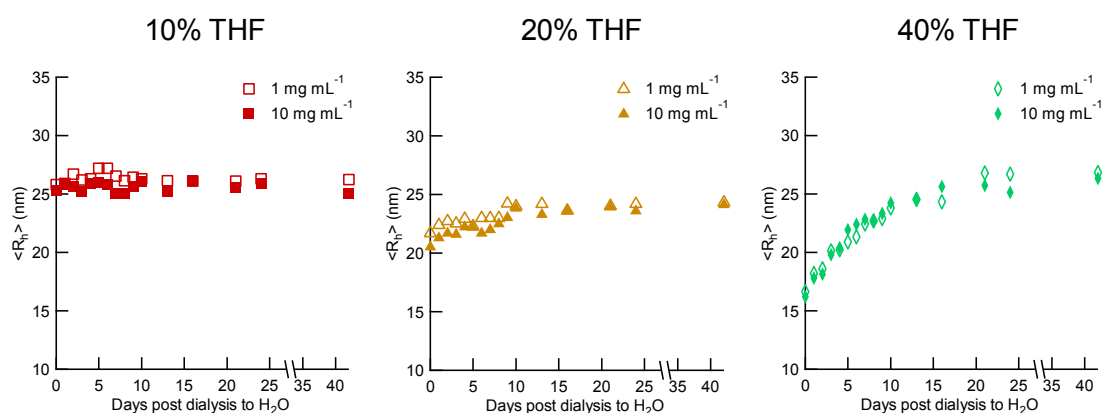


Figure 3.9. DLS data probing the concentration dependence of micelle growth. PB-PEO micelles were prepared at various THF contents (10 wt%, 20 wt%, and 40 wt%) and concentrations (1 mg mL<sup>-1</sup> and 10 mg mL<sup>-1</sup>) prior to dialysis. The DLS experiments were not able to distinguish a concentration dependence as cryo-TEM and SANS suggested. Variability in the fitted  $\langle R_h \rangle$  was within 1-3 nm.

### 3.3.5 Fitting DLS autocorrelation functions

The DLS data contained information about the hydrodynamic diameter and size dispersity of micelles in dilute solutions. Although the concentration dependence was not apparent from DLS experiments, different fitting functions were compared to determine if more detailed information could be extracted from DLS data. The three

fitting methods addressed here are referred to as the quadratic cumulant (QC), the double exponential (DE), and the polydisperse double exponential (PDE), which are detailed in Section 2.3.1.

For the bimodal distribution fits (DE and PDE),  $R_{h1}$  and  $R_{h2}$  were fixed at  $R_{h1} = 15.5$  nm and  $R_{h2} = 26$  nm for each day, and only the intensity weight ( $A_2$ ) and polydispersity parameters (PDE  $\sigma_1$  and  $\sigma_2$ ) were varied. These  $R_h$  values were chosen based on the initial and final sizes, under the assumption that these sizes defined the two main micelle populations. Note that the smaller and larger micelle populations are indicated with subscript '1' and '2', respectively, and that the smaller micelle population intensity weight follows as  $A_1 = 1 - A_2$  based on the data normalization. For the monomodal distribution (QC),  $R_h$  and  $\sigma$  were both allowed to vary in the fit.

The experimental autocorrelation functions for micelle solutions (40 vol% THF and 2 mg mL<sup>-1</sup> prior to dialysis) were analyzed with these three different fits after 90 d stirring after dialysis. Data were normalized between 1 and 2 using the measured baseline and plateau at smaller  $\tau$  (not shown). The DE fits (dashed lines) to the micelle growth data (points) over 90 d are shown in Fig. 3.10. Notably, the DE fit consistently overestimates the data at smaller correlation times and underestimates the data at larger correlation times. The poor fit is likely due to the inherent polydispersity in the sample size distribution that simply is not accounted for in the DE fit. Meanwhile, the PDE fit (Fig. 3.11, dashed lines) better captured the data (points) at lower and higher correlation times due the incorporation of polydispersity for the bimodal distribution. In general, it could be argued that additional parameters will always provide a better fits to experimental data. However, in this case,

incorporating the polydispersity parameter was physically realistic and therefore justifiable.

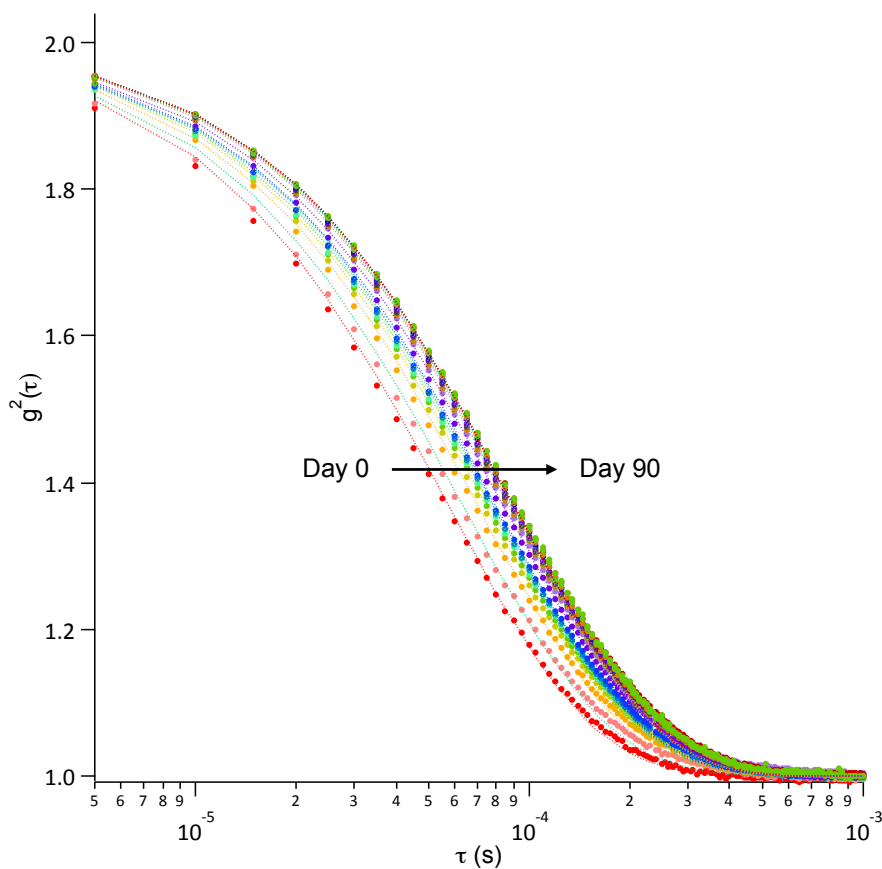


Figure 3.10. DLS autocorrelation functions and double exponential fits over 90 d of stirring post-dialysis for PB-PEO micelles in water (40 vol% THF pre-dialysis,  $2 \text{ mg mL}^{-1}$ ). The double exponential fit (dashed lines) tended to over-predict data (points) at earlier correlation times and under-predict at later correlation times.

The intensity weighting ( $A_2$ ) for the larger size distribution increased over 90 d for the PDE and DE fits, potentially supporting a bimodal growth pathway (Fig.

3.12a). The fitted polydispersity (QC and PDE) was largest at earlier time points ( $t < 7$  d) before gradually decreasing over 90 d (Fig. 3.12b), consistent with the trends in polydispersity that were determined from cryo-TEM, SANS, and SAXS. The sensitivity of the  $\sigma_1$  parameter (smaller population) became negligible as  $A_2$  increased, and the  $\sigma_2$  parameter (larger population) effectively captured the polydispersity.

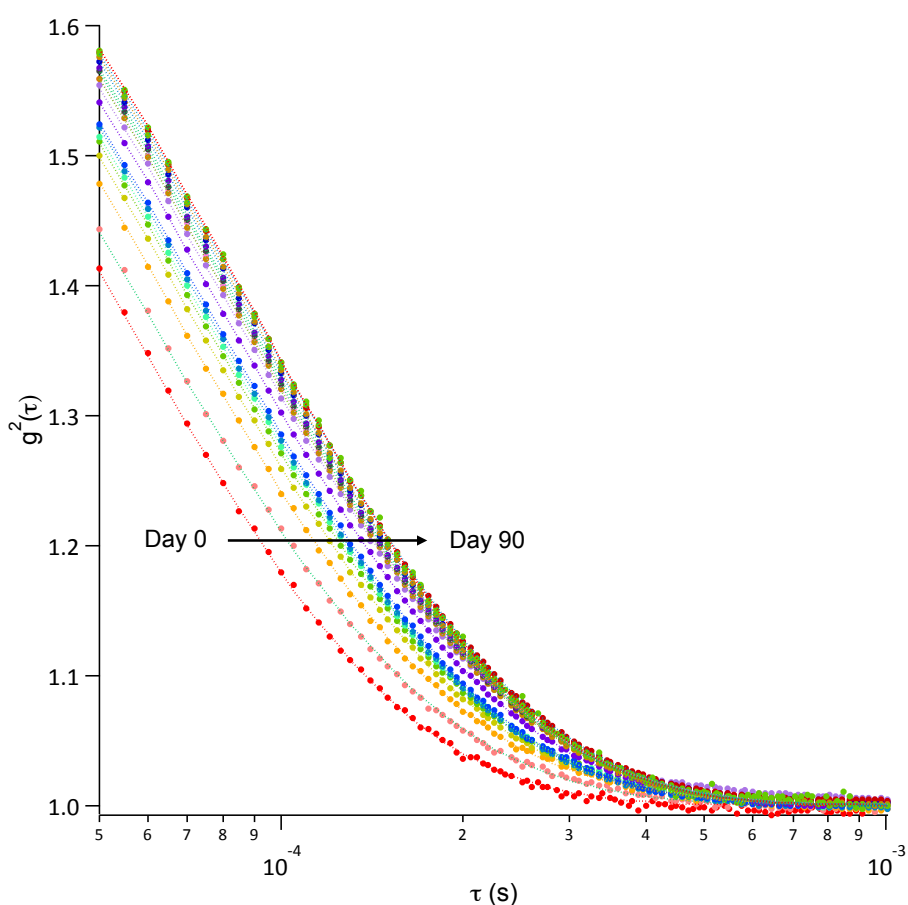


Figure 3.11. DLS autocorrelation functions and polydisperse double exponential fit over 90 d of stirring post-dialysis for PB-PEO micelles in water (40 vol% THF pre-dialysis,  $2 \text{ mg mL}^{-1}$ ). The polydisperse double exponential function (dashed lines) better fit the experimental data (points) at earlier and later correlation times.

Two polydisperse double exponential (PDE) fits and corresponding size distributions were compared for the same DLS data describing PB-PEO micelles in water on Day 9 after dialysis (40 vol% THF, 2 mg mL<sup>-1</sup> before dialysis) (Fig. 3.12c and 3.12d). The measured autocorrelation data (black dots) and PDE fit (red line) using the first set of given parameters ( $A_1 = 0.3$ ,  $\sigma_1 = 0$ ,  $R_{h1} = 17$  nm,  $A_2 = 0.7$ ,  $\sigma_2 = 0.22$ ,  $R_{h2} = 27.5$  nm) resulted in a root mean square error of 4.57E-03. The measured autocorrelation data and PDE fit (blue line) using a second set of parameters ( $A_1 = 0$ , undefined  $\sigma_1$ , undefined  $R_{h1}$ ,  $A_2 = 1.0$ ,  $\sigma_2 = 0.22$ ,  $R_{h2} = 23.5$  nm) resulted in a root mean square error of 4.87E-03.

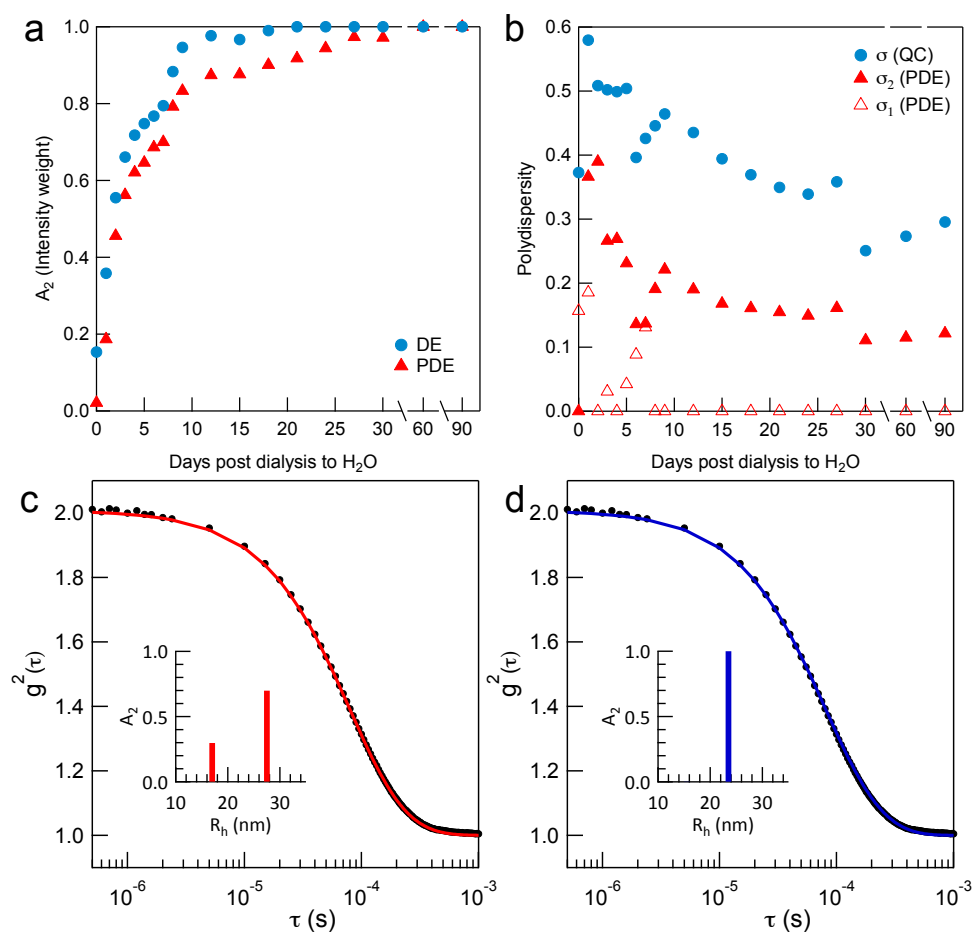


Figure 3.12. DLS fitting parameters for PB-PEO micelles 40 vol% THF pre-dialysis. (a) Intensity weighting of larger micelle population as a function of days post dialysis for double exponential and polydisperse double exponential fits. (b) Polydispersity parameters for the quadratic cumulant and polydisperse double exponential fits. (c) Experimental autocorrelation function on day 9 and corresponding fit with polydisperse double exponential. Inset shows fitted  $R_h$  and intensity weight ( $A_2$ ). (d) Corresponding fit to the same data shown in (c) but with different fitted  $R_h$  and  $A_2$ .

The nearly identical fits to the same measured autocorrelation curve led to significantly different intensity weights of the larger micelles, resulting in even greater

uncertainty in the number size distribution determined from DLS. Near the plateau in  $R_h$  around Day 8 or 9, small differences in the intensity weight would correspond to very significant differences in number weight. For example, assuming the intensity scales with the radius as  $I \sim R^6$ , allowing the intensity weights of the larger micelles to vary between 70% to 100% would result in a range of number weights between 10% and 100% (refer to Appendix A, Figure A.7). For this reason, quantitative kinetics extracted from light scattering data contained significant uncertainty. The uncertainty demonstrated in Fig. 3.12c and Fig. 3.12d likely explained the discrepancy in concentration dependence between the DLS results and the cryo-TEM and SANS results.

The root mean square error (RMSE) for three different fitting methods obtained over 90 d (40 vol% THF, 2 mg mL<sup>-1</sup> before dialysis) is given in Fig. 3.13. In general, the low RMSE of the corresponding fits to the data indicated that all three fitting methods effectively captured the growth over 90 d. Therefore, distinguishing the underlying size distribution from DLS was not conclusive, although the comparison clearly showed that the PDE and QC fits were consistently better fits compared to the DE fit over 90 d. However, the QC fit was chosen to describe the trend in increase  $R_h$ , as it captured the general trends in the data with only two parameters.

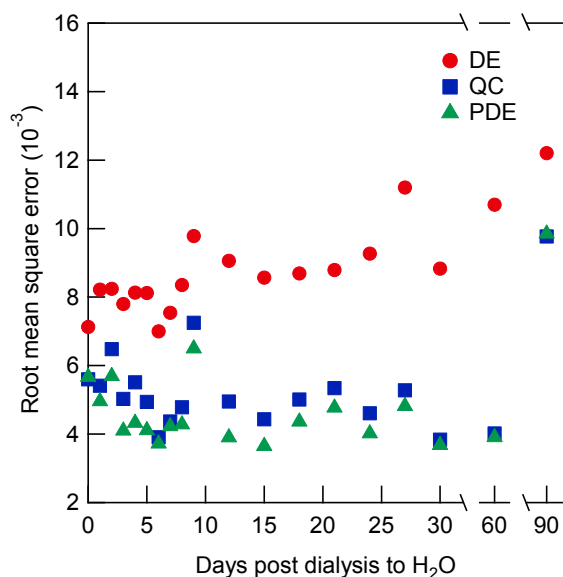


Figure 3.13. Root mean square error (RMSE) for different DLS fitting methods. The polydisperse double exponential fit gave the best fit overall throughout 90 d (PB-PEO 40 vol% THF pre-dialysis 2 mg mL<sup>-1</sup>) followed by the quadratic cumulant and the double exponential fits.

### 3.4 Shear-Induced Interfacial Nucleation

The bimodal micelle growth behavior in the PB-PEO micelle solutions has critical implications for block polymer micelle stability in highly selective solvents. When perturbed far enough from their equilibrium size, block polymer micelles grew through a fusion-controlled, bimodal pathway separated by multiple fusion events. Similar bimodal growth processes are found in various systems including proteins,<sup>30</sup> small molecules,<sup>30,31</sup> and nanoparticles,<sup>32</sup> with each system characterized by distributions of primary particles and larger aggregates.

For the micelle growth found here, one proposed mechanism is that the small micelles fuse to form metastable intermediates, which then fuse rapidly with additional smaller micelles to produce larger micelles, similar to a nucleation and

growth mechanism. This growth process is analogous to micellization of surfactants, in which the final micelle size is limited by repulsive interactions between head groups.<sup>33</sup> In the case of PB-PEO micelles described herein, corona chain repulsion could limit the micelle growth and final size independent of the initial size, as shown in Fig. 3.2. Importantly, this steady state size was smaller than that of micelles formed by directly dispersing the PB-PEO in water without THF addition (0 vol% THF), highlighting the influence of processing conditions on the self-assembly of macromolecular amphiphiles.

An alternate hypothesis for the bimodal growth mechanism entails agitation-induced interfacial adsorption and growth at the air-water interface. This concept was supported by Fig 3.1, which demonstrated that the micelle growth critically depended on stirring the solution. Such agitation-induced phenomena are known to affect the stability of block polymer surfactants,<sup>34,35</sup> other macromolecular assemblies,<sup>36-38</sup> and proteins<sup>13,39-41</sup> in aqueous solutions. For example, several studies demonstrated that proteins readily aggregated during agitation by adsorbing and unfolding at the air-water.<sup>39-41</sup> Analogously, the micelles could “unlock” after adsorbing at the air-water interface before fusing and growing into larger micelles. Essentially, the fluid hydrophobic interface would provide an alternative growth pathway with a lower energetic barrier than bulk water. Interestingly, the potential interfacial nucleation/unfolding step appeared hindered to some extent by the micelle size, as growth eventually plateaued after weeks of relaxation (Fig. 3.2). Clearly, further quantitative studies are required to distinguish a more complicated mechanism incorporating the influence of shear and interfacial effects.

### 3.5 Chapter Summary

In summary, these findings highlight the considerable influence of cosolvent preparation methods on the stability of macromolecular assemblies and demonstrate the kinetic constraints in block polymer micelles containing highly hydrophobic cores. Micelle fusion/fission events occur in amphiphilic block polymer micelles when the system is perturbed far from equilibrium, even in highly selective solvents such as water. The unexpected micelle growth likely was induced by an interfacial and/or shear phenomenon, leading to a bimodal size distribution separated by multiple fusion events with less dominant intermediate sizes. While the effects of perturbation and agitation often are overlooked in polymeric assemblies, these results highlight similarities between the processing effects in polymeric systems and those that are influential in small molecule and protein assemblies. The relationships between processing conditions and subsequent dynamics have critical implications on the stability of macromolecular-based nanocarriers. Furthermore, these results emphasize the need for more quantitative investigations into the underlying mechanisms affecting micelle stability to enable a thorough understanding of the complex dynamic processes in amphiphilic block polymer solution assemblies. These results prompted studies into temperature and molecular weight effects (Chapter 4) as well as investigations into the shear and interfacial effects (Chapter 5) to better grasp the influence of kinetic and thermodynamic contributions on micelle chain exchange in dilute aqueous solutions.

## REFERENCES

- 1 Blanz, A., Armes, S. P. & Ryan, A. J. Self-assembled block copolymer aggregates: from micelles to vesicles and their biological applications. *Macromolecular Rapid Communications* **30**, 267-277 (2009).
- 2 Smart, T. *et al.* Block copolymer nanostructures. *Nano Today* **3**, 38-46 (2008).
- 3 Won, Y. Y., Davis, H. T. & Bates, F. S. Molecular exchange in PEO-PB micelles in water. *Macromolecules* **36**, 953-955 (2003).
- 4 Lund, R., Willner, L., Richter, D. & Dormidontova, E. E. Equilibrium chain exchange kinetics of diblock copolymer micelles: Tuning and logarithmic relaxation. *Macromolecules* **39**, 4566-4575 (2006).
- 5 Lund, R. *et al.* Unraveling the equilibrium chain exchange kinetics of polymeric micelles using small-angle neutron scattering - architectural and topological effects. *Journal of Applied Crystallography* **40**, S327-S331 (2007).
- 6 Lund, R., Willner, L., Stellbrink, J., Lindner, P. & Richter, D. Logarithmic chain-exchange kinetics of diblock copolymer micelles. *Physical Review Letters* **96**, 068302 (2006).
- 7 Pochan, D. J. *et al.* Toroidal triblock copolymer assemblies. *Science* **306**, 94-97 (2004).
- 8 Groschel, A. H. *et al.* Precise hierarchical self-assembly of multicompart ment micelles. *Nat. Commun.* **3**, 10 (2012).
- 9 Halperin, A. & Alexander, S. Polymeric micelles - their relaxation kinetics. *Macromolecules* **22**, 2403-2412 (1989).
- 10 Nyrkova, I. A. & Semenov, A. N. On the theory of micellization kinetics. *Macromolecular Theory and Simulations* **14**, 569-585 (2005).
- 11 Jain, S. & Bates, F. S. Consequences of nonergodicity in aqueous binary PEO-PB micellar dispersions. *Macromolecules* **37**, 1511-1523 (2004).
- 12 Dormidontova, E. E. Micellization kinetics in block copolymer solutions: Scaling model. *Macromolecules* **32**, 7630-7644 (1999).

- 13 Bai, G., Bee, J. S., Biddlecombe, J. G., Chen, Q. & Leach, W. T. Computational fluid dynamics (CFD) insights into agitation stress methods in biopharmaceutical development. *International Journal of Pharmaceutics* **423**, 264-280 (2012).
- 14 Halperin, A., Tirrell, M. & Lodge, T. P. Tethered chains in polymer microstructures. *Advances in Polymer Science* **100**, 31-71 (1992).
- 15 Esselink, F. J., Semenov, A. N., ten Brinke, G., Hadziioannou, G. & Oostergetel, G. T. Ordering of block copolymer micelles in confined two-dimensional solutions. *Macromolecules* **28**, 3479-3481 (1995).
- 16 Choi, S. H., Lodge, T. P. & Bates, F. S. Mechanism of molecular exchange in diblock copolymer micelles: hypersensitivity to core chain length. *Physical Review Letters* **104**, 047802 (2010).
- 17 Lund, R., Willner, L. & Richter, D. Kinetics of Block Copolymer Micelles Studied by Small-Angle Scattering Methods. *Advances in Polymer Science* **259**, 51-158 (2013).
- 18 Nicolai, T., Colombani, O. & Chassenieux, C. Dynamic polymeric micelles versus frozen nanoparticles formed by block copolymers. *Soft Matter* **6**, 3111-3118 (2010).
- 19 Denkova, A. G., Mendes, E. & Coppens, M. O. Non-equilibrium dynamics of block copolymer micelles in solution: recent insights and open questions. *Soft Matter* **6**, 2351-2357 (2010).
- 20 Rharbi, Y. Fusion and fragmentation dynamics at equilibrium in triblock copolymer micelles. *Macromolecules* **45**, 9823-9826 (2012).
- 21 Meli, L. & Lodge, T. P. Equilibrium vs metastability: High-temperature annealing of spherical block copolymer micelles in an ionic liquid. *Macromolecules* **42**, 580-583 (2009).
- 22 Repollet-Pedrosa, M. H. & Mahanthappa, M. K. Fusion of poly(vinyl acetate-b-vinyl alcohol) spherical micelles in water induced by poly(ethylene oxide). *Soft Matter* (2013).
- 23 Zinn, T., Willner, L., Lund, R., Pipich, V. & Richter, D. Equilibrium exchange kinetics in n-alkyl-PEO polymeric micelles: single exponential relaxation and chain length dependence. *Soft Matter* **8**, 623-626 (2012).

- 24 Zheng, Y. *et al.* Directly Resolved Core-Corona Structure of Block Copolymer Micelles by Cryo-Transmission Electron Microscopy. *The Journal of Physical Chemistry B* **103**, 10331-10334 (1999).
- 25 Won, Y.-Y., Brannan, A. K., Davis, H. T. & Bates, F. S. Cryogenic Transmission Electron Microscopy (Cryo-TEM) of Micelles and Vesicles Formed in Water by Poly(ethylene oxide)-Based Block Copolymers. *The Journal of Physical Chemistry B* **106**, 3354-3364 (2002).
- 26 Li, Z. L. & Dormidontova, E. E. Equilibrium chain exchange kinetics in block copolymer micelle solutions by dissipative particle dynamics simulations. *Soft Matter* **7**, 4179-4188 (2011).
- 27 Honda, C., Hasegawa, Y., Hirunuma, R. & Nose, T. Micellization kinetics of block copolymers in selective solvent. *Macromolecules* **27**, 7660-7668 (1994).
- 28 Nose, T. & Iyama, K. Micellization and relaxation kinetics of diblock copolymers in dilute solution based on A-W theory: I. Description of a model for core-corona type micelles. *Computational and Theoretical Polymer Science* **10**, 249-257 (2000).
- 29 Li, Z. L. & Dormidontova, E. E. Kinetics of Diblock Copolymer Micellization by Dissipative Particle Dynamics. *Macromolecules* **43**, 3521-3531 (2010).
- 30 De Greef, T. F. A. *et al.* Supramolecular Polymerization. *Chemical Reviews* **109**, 5687-5754 (2009).
- 31 Stepanenko, V., Li, X.-Q., Gershberg, J. & Würthner, F. Evidence for Kinetic Nucleation in Helical Nanofiber Formation Directed by Chiral Solvent for a Perylene Bisimide Organogelator. *Chemistry – A European Journal* **19**, 4176-4183 (2013).
- 32 Wang, J. *et al.* Nucleation-Controlled Polymerization of Nanoparticles into Supramolecular Structures. *Journal of the American Chemical Society* **135**, 11417-11420 (2013).
- 33 Tanford, C. *The Hydrophobic Effect: Formation of Micelles and Biological Membranes*. 2nd edn, (Wiley-Interscience, 1979).
- 34 Li, S. *et al.* Surface micelle formation at the air/water interface from nonionic diblock copolymers. *Langmuir* **9**, 2243-2246 (1993).

- 35 Ahmed, F., Hategan, A., Discher, D. E. & Discher, B. M. Block Copolymer Assemblies with Cross-Link Stabilization: From Single-Component Monolayers to Bilayer Blends with PEO–PLA. *Langmuir* **19**, 6505-6511 (2003).
- 36 Wang, C.-W., Sinton, D. & Moffitt, M. G. Flow-Directed Block Copolymer Micelle Morphologies via Microfluidic Self-Assembly. *Journal of the American Chemical Society* **133**, 18853-18864 (2011).
- 37 Sorrells, J. L., Tsai, Y.-H. & Wooley, K. L. The influence of solution-state conditions and stirring rate on the assembly of poly(acrylic acid)-containing amphiphilic triblock copolymers with multi-amines. *Journal of Polymer Science Part A: Polymer Chemistry* **48**, 4465-4472 (2010).
- 38 Yu, H. & Jiang, W. Effect of Shear Flow on the Formation of Ring-Shaped ABA Amphiphilic Triblock Copolymer Micelles. *Macromolecules* **42**, 3399-3404 (2009).
- 39 Nielsen, L. *et al.* Effect of environmental factors on the kinetics of insulin fibril formation: Elucidation of the molecular mechanism. *Biochemistry* **40**, 6036-6046 (2001).
- 40 Thomas, C. R. & Geer, D. Effects of shear on proteins in solution. *Biotechnology Letters* **33**, 443-456 (2011).
- 41 Patapoff, T. W. & Esue, O. Polysorbate 20 prevents the precipitation of a monoclonal antibody during shear. *Pharmaceutical Development and Technology* **14**, 659-664 (2009).

## Chapter 4

### EFFECTS OF MOLECULAR WEIGHT AND TEMPERATURE

The previous chapter demonstrated that changes in micelle size or aggregation number could occur in water provided that micelles were perturbed far enough from their assumed near-equilibrium size. Complementary *in situ* characterization methods depicted an exchange process that followed a bimodal pathway characterized by both concentration and shear dependence. To better understand the thermodynamic and kinetic contributions to this bimodal growth process, Ch. 4 focuses on the effects of other key system parameters, namely core molecular weight, corona molecular weight, and temperature.

#### 4.1 Introduction

Block polymer materials have gained significant attention for applications in drug delivery, catalysis, diagnostics, and other dispersant technologies. These applications require processing and formulation steps, both of which can influence the structure and function of block polymer solution assemblies. As a result, it is critical to understand both the thermodynamic and kinetic contributions to block polymer solution assembly.

Several experimental and theoretical works have established fundamental relationships between key parameters that dictate micelle equilibrium size and structure.<sup>1</sup> Zhulina *et al.* used free energy analysis to establish relationships between equilibrium aggregation number, core and corona block degree of polymerization,

segment length, as well as core-solvent interfacial tension.<sup>2</sup> These predictions agreed reasonably well with experiments on sphere-to-cylinder morphological transitions.<sup>2</sup>

More recently, experiments using time-resolved SANS (TR-SANS) on block polymers in cosolvent mixtures have greatly improved the understanding of chain exchange dynamics under quiescent conditions, as well as the effects of core block molecular weight and interfacial tension.<sup>1,3</sup> The inherent polydispersity of macromolecular assemblies was found to play an important role in the apparent logarithmic chain exchange relaxation process, as it was demonstrated that the dispersity of the core block could account for a double exponential relaxation process.<sup>4</sup> Furthermore, the independent chain hypothesis was supported through experiments in which polymers of different core block molecular weight were mixed, and TR-SANS techniques were used to measure two distinct relaxation processes.<sup>5,6</sup>

In addition to the influences of core block molecular weight and solvent selectivity, the effect of temperature has also been previously explored. For single chain exchange experiments under quiescent conditions, a experimentally determined temperature-dependent relaxation times agreed with the expected changes in diffusion of unentangled polymers within the cores, as predicted by the Rouse model.<sup>4</sup> A time-temperature superposition was employed to access a broader range in relaxation times, which were experimentally feasible SANS acquisition times. Other temperature jump experiments examined poly(butadiene-*b*-ethylene oxide) (PB-PEO) micelles in ionic liquids, measuring a decrease in micelle hydrodynamic radius at various temperatures and concentrations under quiescent conditions.<sup>7,8</sup> A fusion/fission exchange mechanism most likely explained the decrease in micelle size that occurred over

minutes based on (1) the lack of single-chain exchange determined by SANS and (2) the distinct concentration-dependent decay rate.<sup>8</sup>

While considerable progress has been made in understanding the chain exchange in aqueous solutions under *quiescent* conditions, little work has explored the exchange kinetics in *agitated* aqueous solutions. Theoretical and experimental evidence that demonstrated arrested chain exchange under quiescent conditions is likely responsible for this overlooked distinction pertaining to agitated micelle solutions.<sup>9-11</sup> However, the results of Ch. 3 indicated that highly amphiphilic PB-PEO micelles could evolve in water after considerable perturbation and agitation. These results motivated the exploration into the molecular weight and temperature dependence within agitated aqueous solution in order to better understand and explain the mechanism for chain exchange.

Chapter 3 investigated the concentration dependence and effect of solution agitation on the PB-PEO micelle size evolution in aqueous solutions following THF cosolvent removal. Section 4.2 expands upon the slow micelle size evolution by exploring the temperature and core/corona molecular weight dependence. With fixed polymer concentrations and agitation rate, complementary characterization methods (DLS and cryo-TEM) probe the effects of these important system parameters. Section 4.3 illustrates that the characteristic timescale for the micelle growth can be controlled and significantly reduced by five orders of magnitude by vigorous agitation (i.e. rapid vortex mixing). An empirical correlation showed that the intensity-weighted micelle relaxation could be described by an exponential relationship. Overall, the characteristic relaxation time was found to depend on the polymer molecular weight, temperature, and method of solution agitation.

## **4.2 Slow Micelle Relaxation Kinetics**

Following the methods established in Ch. 3, this section investigates the micelle size evolution following cosolvent removal. Experiments were designed to distinguish relationships between the micelle chain exchange process and parameters including the corona and core molecular weight as well as temperature (4.2.1-4.2.3). Observed morphological transitions at higher temperatures are discussed in further detail (4.2.4).

### **4.2.1 Experimental design**

The previous chapter revealed a dependence of solution agitation and polymer concentration on the micelle growth process. The main objective for the following experiments was to examine other effects that may provide insight into the underlying growth mechanism. Consequently, the polymer concentration ( $10 \text{ mg mL}^{-1}$ ) and agitation rate (magnetic stirring at 200 rpm) were fixed for each sample. For each temperature and molecular weight, the micelle size perturbation was examined for 40 wt% THF samples (before dialysis to water) and compared to the 0 wt% THF samples. Figure 4.1 demonstrated the 24 combinations of experimental parameters (2 THF contents, 3 molecular weights, 4 temperatures) that were chosen to minimize the total number of necessary experiments to establish trends.

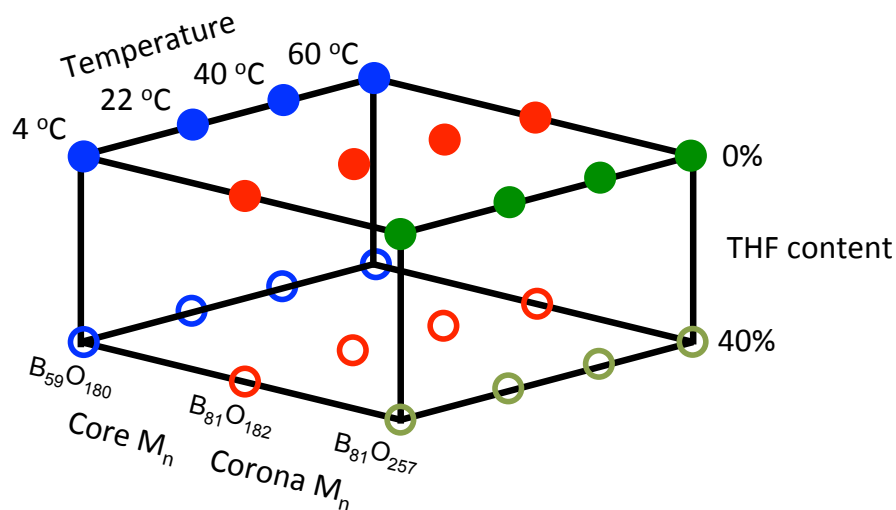


Figure 4.1. Experimental design variables. The four main variables investigated were temperature, core and corona molecular weight, and THF content before dialysis to water. Each variable was expected to influence micelle chain exchange and to provide insight into the growth mechanism. The polymer concentration before dialysis ( $10 \text{ mg mL}^{-1}$ ) and solution agitation (magnetic stirring at 200 rpm) were fixed.

The dependence of solution agitation was reproduced for higher molecular weight samples  $B_{81}O_{182}$  and  $B_{81}O_{257}$  at room temperature ( $22 \pm 3 \text{ }^\circ\text{C}$ ) with varying THF contents prior to dialysis against  $\text{H}_2\text{O}$ . Figure 4.2 showed that the effective  $R_h$  did not significantly change without magnetic stirring. These results were consistent with the lower molecular weight sample  $B_{59}O_{180}$  shown in Fig. 3.1.

The frozen kinetics in water under quiescent conditions can be advantageous. For example, samples at various time points could be stored (without agitation) for later examination with other techniques such as SANS or cryo-TEM. Moreover, the size distribution did not change measurably during sample acquisition. As a result, good time resolution was not necessary.

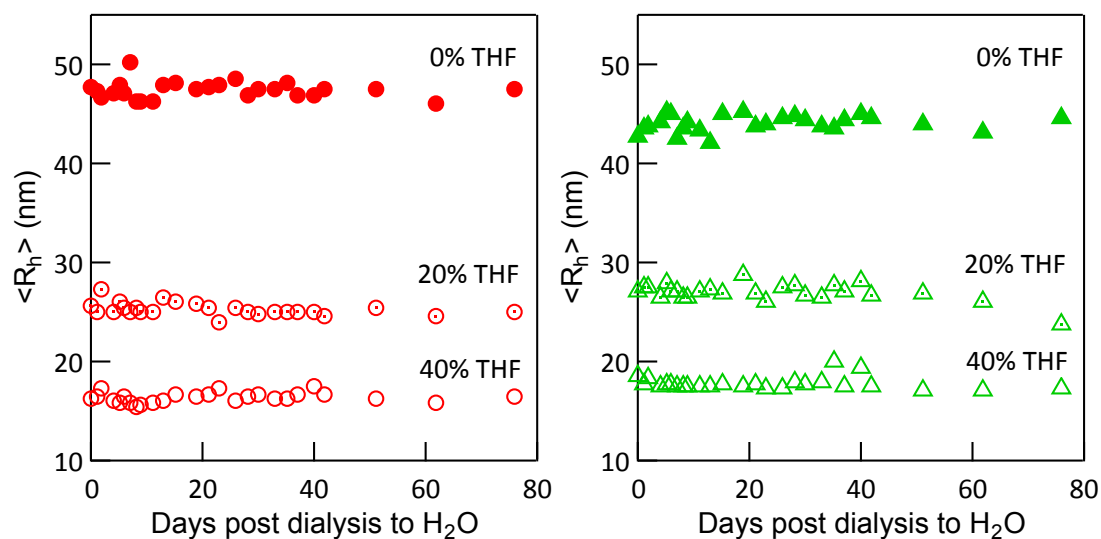


Figure 4.2. Micelle hydrodynamic radius without solution agitation in water following dialysis. Solutions of  $B_{81}O_{182}$  (left) and  $B_{81}O_{257}$  (right) in various THF/water contents (wt% THF) were dialyzed against pure water to produce kinetically-frozen micelles. In the absence of stirring, micelles did not change size over 80 d at room temperature regardless of the THF content.

#### 4.2.2 Core and corona molecular weight dependence

Block polymer micelle thermodynamics and chain exchange kinetics depend on the core (PB) and corona (PEO) molecular weight. In general, minimum free energy analysis and scaling relationships provide predictions for the energetically favorable micelle aggregation number, morphology, and size in solution.<sup>2,12</sup>

Thermodynamic relationships establish a micelle morphology and size toward which the system will evolve given infinite time, but they do not describe how fast the system will evolve. For systems that evolve slowly, as is generally the case for high molecular weight amphiphiles, kinetic relationships begin to dominate the discussion.

Chain exchange kinetic relationships depend on many variables, two of which are the degree of polymerization of the core and corona blocks. A strong kinetic

dependence on the core block ( $N_B$ ) for single chain exchange (Eq. 1.6) relates the Rouse timescale (chain diffusion within the core) and a double exponential dependence on  $\chi N$ , or the core-solvent interaction strength<sup>4</sup>. Meanwhile, for a given aggregation number, energetic barriers for micelle fusion should scale with the corona block ( $N_A$ ), assuming that the necessary chain compression required for micelle coalescence scales with the corona thickness or radius of gyration.<sup>13</sup> However, these trends were established for quiescent conditions that account for micelle diffusion and chain diffusion due to thermal energy. Given that the micelle growth found in Ch. 3 was dependent on solution agitation, it was uncertain how the kinetics would depend on core or corona molecular weight under flowing conditions. Hence, establishing trends in molecular weight and temperature could provide insight into the kinetic process and underlying chain exchange mechanism.

Figure 4.3 mapped all samples with varying molecular weight, temperature, and THF content. First, the molecular weight dependence is discussed in general without considering effects of temperature. In the following section, the temperature dependence and reasons for the sharp size increase and precipitation are discussed in detail (4.2.3 and 4.2.4).

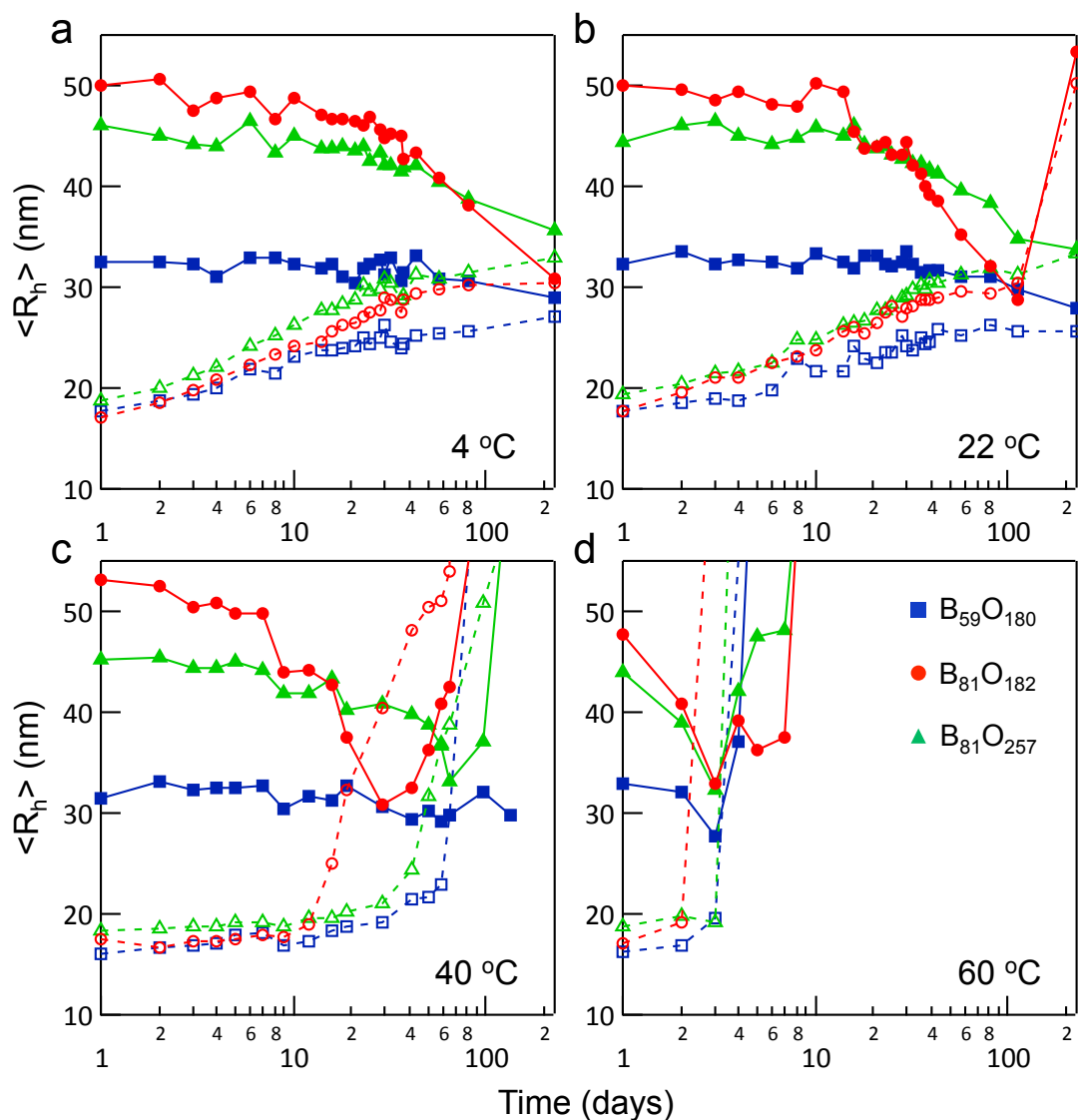


Figure 4.3. Molecular weight and temperature dependence of micelle size evolution. Micelles that were magnetically stirred showed either an increase (40 wt% THF, open symbols) or decrease (0% THF, closed symbols) in hydrodynamic radius over time. Both the molecular weight and temperature led to different characteristic relaxation timescales.

As shown in Fig. 4.3 for 0% THF samples (solid symbols), the initial intensity-weighted  $R_h$  values were significantly larger for  $B_{81}O_{182}$  (~ 50 nm) and

$B_{81}O_{257}$  ( $\sim 45$  nm) polymers compared to  $B_{59}O_{180}$  ( $\sim 35$  nm). This result could be rationalized based on the increase in  $N_{PB}$  from 59 to 81; however, the subsequent decrease in  $R_h$  over time to  $\sim 30$ - $35$  nm upon stirring suggested that the sizes obtained by direct dissolution were not near equilibrium. This result differed from the lower molecular weight polymer ( $B_{59}O_{180}$ , 0% THF) that formed reproducible sizes when directly dispersed in water. The contrast in the initial  $R_h$  demonstrated the strong sensitivity to molecular weight in the direct dissolution method. Similar path-dependent solution assembly was explored previously for PB-PEO ( $B_{148}O_{159}$ ) in ionic liquids, which showed larger micelles forming via direct dissolution when compared to a cosolvent preparation method.<sup>7</sup>

The 0% THF samples were examined with cryo-TEM to probe the micelle size distribution. Figure 4.4 illustrated that both  $B_{81}O_{182}$  and  $B_{81}O_{257}$  contained micelles with core sizes of  $R_c \sim 14$ - $15$  nm, as well as an approximate micelle radius  $R_m \sim 35$ - $40$  nm. Cryo-TEM results suggested that the initial size determined from DLS ( $R_h \sim 45$ - $50$  nm) was due to the intensity weighting of the size distribution. This result implied the 0 wt% THF solutions contained some mixture of larger micelles ( $R_h \sim 45$ - $50$  nm) and smaller micelles ( $R_h \sim 35$ - $40$  nm), instead of a single population. SANS analysis further supported this conclusion for  $B_{81}O_{182}$  micelles ( $R_c \sim 14$  nm,  $R_m \sim 35$  nm) and  $B_{81}O_{257}$  micelles ( $R_c \sim 15$  nm,  $R_m \sim 41$  nm) in water (see Appendix A, Figure A.8). The subsequent size decrease upon solution agitation over several months likely resulted from breakage (fission) of the slightly larger micelles apparent from DLS kinetic plots.

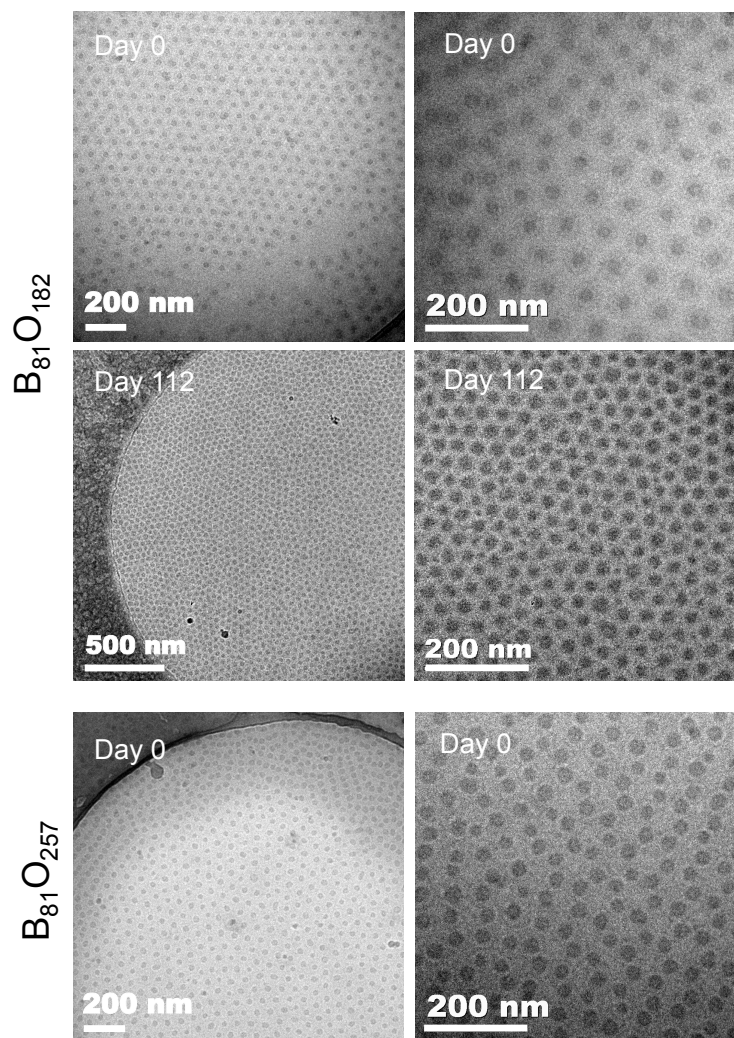


Figure 4.4. Cryo-TEM images of PB-PEO micelles after dialysis (0% THF, 22 °C) samples. Images of  $B_{81}O_{182}$  immediately after dialysis on day 0 (top row) and day 112 (middle row) showed a slight decrease in core size from  $R_c \sim 14\text{-}16$  nm to  $R_c \sim 12$  nm. For comparison,  $B_{81}O_{257}$  showed similar core sizes  $R_c \sim 15$  nm on day 0 (bottom row).

Figure 4.3 also showed the effect of samples prepared from a cosolvent preparation method (40 wt% THF). The initial hydrodynamic radius  $R_i$  (Day 0) for the 40 wt% THF samples did not appear to depend significantly on either the core or

corona molecular weight ( $R_h \sim 18$  nm) based on the fitted  $R_h$  variability (1 to 3 nm). Upon agitating the solutions, the average intensity weighted  $R_h$  increased throughout several weeks before reaching a size plateau, defined as the steady state or final size  $R_f$ . The size relaxation was found to follow the empirical expression written as

$$\frac{R_h(t) - R_i}{R_f - R_i} = 1 - \exp\left(-\frac{t}{\tau}\right) \quad (4.1)$$

in which  $\tau$  is the characteristic relaxation time.

Unlike the initial size, the steady state size and characteristic relaxation time depended on the core and corona molecular weight. For  $B_{59}O_{180}$ , the steady state hydrodynamic radius was  $R_h \sim 25$  nm with a characteristic time of  $\tau \sim 7$  d to 10 d depending on the defined  $R_i$  and  $R_f$ . An increase in core molecular weight ( $B_{81}O_{182}$ ) resulted in larger steady state size ( $R_h \sim 30$  nm) and characteristic time ( $\tau \sim 13$  d to 14 d). Further increasing the corona molecular weight ( $B_{81}O_{257}$ ) led to an increase in steady state size ( $R_h \sim 33$  nm) and similar characteristic times ( $\tau \sim 14$  d to 15 d). These general trends for increasing  $R_h$  and  $\tau$  did not apply for higher temperatures (40 °C and 60 °C), which was discussed further in the following section.

Cryo-TEM was utilized to further probe the molecular weight dependence of micelle growth in aqueous solutions. Figure 4.5 showed that micelles stirring at room temperature grew through a bimodal pathway regardless of the molecular weight. The larger micelle population for  $B_{81}O_{182}$  and  $B_{81}O_{257}$  ( $R_c \sim 14$ -16 nm,  $R_m \sim 35$ -40 nm) were estimated from cryo-TEM to be slightly larger than  $B_{59}O_{180}$  ( $R_c \sim 11$ -12 nm,  $R_m \sim 30$ -35 nm). By qualitatively comparing micelle size distributions from cryo-TEM at similar time points for different molecular weights,  $B_{81}O_{182}$  and  $B_{81}O_{257}$  appeared to grow at a slower rate than  $B_{59}O_{180}$  based on differences in the relative

number of smaller and larger micelles. These qualitative trends were consistent with the increase in steady state sizes and characteristic times determined from DLS.

Both DLS and cryo-TEM were effective at establishing a qualitative framework for the molecular weight dependence on micelle growth in aqueous environments. Namely, these particle-sizing techniques demonstrated that increasing the core and corona molecular weight both slowed down the growth process (40 wt% THF samples) and also led to the breakage of larger micelles over time (0 wt% THF samples). However, skewed intensity-weighted distribution from DLS and potentially biased sampling statistics from cryo-TEM rendered the quantitative assessment unreliable. Future kinetic studies using SANS or other analytical separation techniques are necessary for quantitative kinetics, good statistics, and better size resolution.

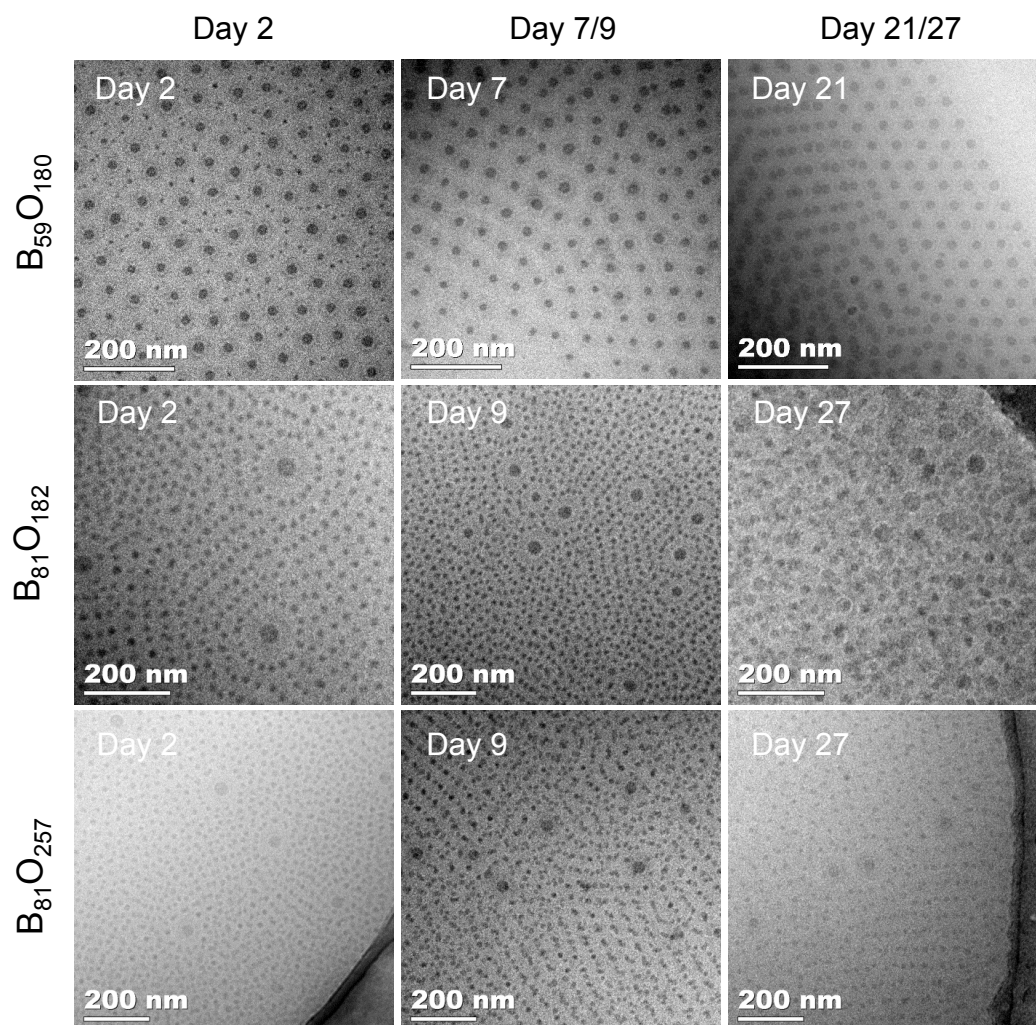


Figure 4.5. Bimodal micelle size evolution following dialysis to water (40% THF, 22°C). Agitated solutions of  $B_{59}O_{180}$  (top),  $B_{81}O_{182}$  (middle), and  $B_{81}O_{257}$  (bottom) showed a bimodal distribution of micelle sizes.  $B_{81}O_{182}$  and  $B_{81}O_{257}$  showed slower micelle growth based the predominance of smaller micelles on day 27 compared to  $B_{59}O_{180}$  on day 21.

### 4.2.3 Temperature dependence

Changes in temperature were expected to affect both the thermodynamics and kinetics of micelle growth and breakage. There are numerous parameters coupled with the system temperature, such as solvent quality, solution viscosity, particle and

chain diffusivity, polymer interactions, and interfacial tension. Each could affect the chain exchange kinetics to varying degrees, and hence some of these consequences were considered for the 0% THF samples followed by the 40 wt% THF samples.

Figure 4.6 portrayed the same DLS data shown previously (Fig. 4.5) in a different format to highlight the effect of temperature on the 0 wt% and 40 wt% THF samples. For  $B_{81}O_{182}$  and  $B_{81}O_{257}$  (0 wt%), an increase in temperature from 4 °C up to 60 °C led to faster decreases in  $R_h$ . Greater chain mobility, diffusion, and lower PB-water interfacial tension<sup>14</sup> from increasing temperature could explain the faster kinetics of micelle breakage. Furthermore, the nearly exponential decay in effective  $R_h$  (variation of Eq. 4.1) was consistent with previous data for PB-PEO spherical micelles in ionic liquids.<sup>7</sup> Within ionic liquids, micelles could equilibrate under quiescent conditions on a much faster timescale ( $10^2$  min) at temperatures ranging up to 170 °C. The results here demonstrated that similar micelle relaxation occurred over longer timescales ( $10^3$  to  $10^5$  min) at lower temperatures, provided that samples were agitated or stirred.

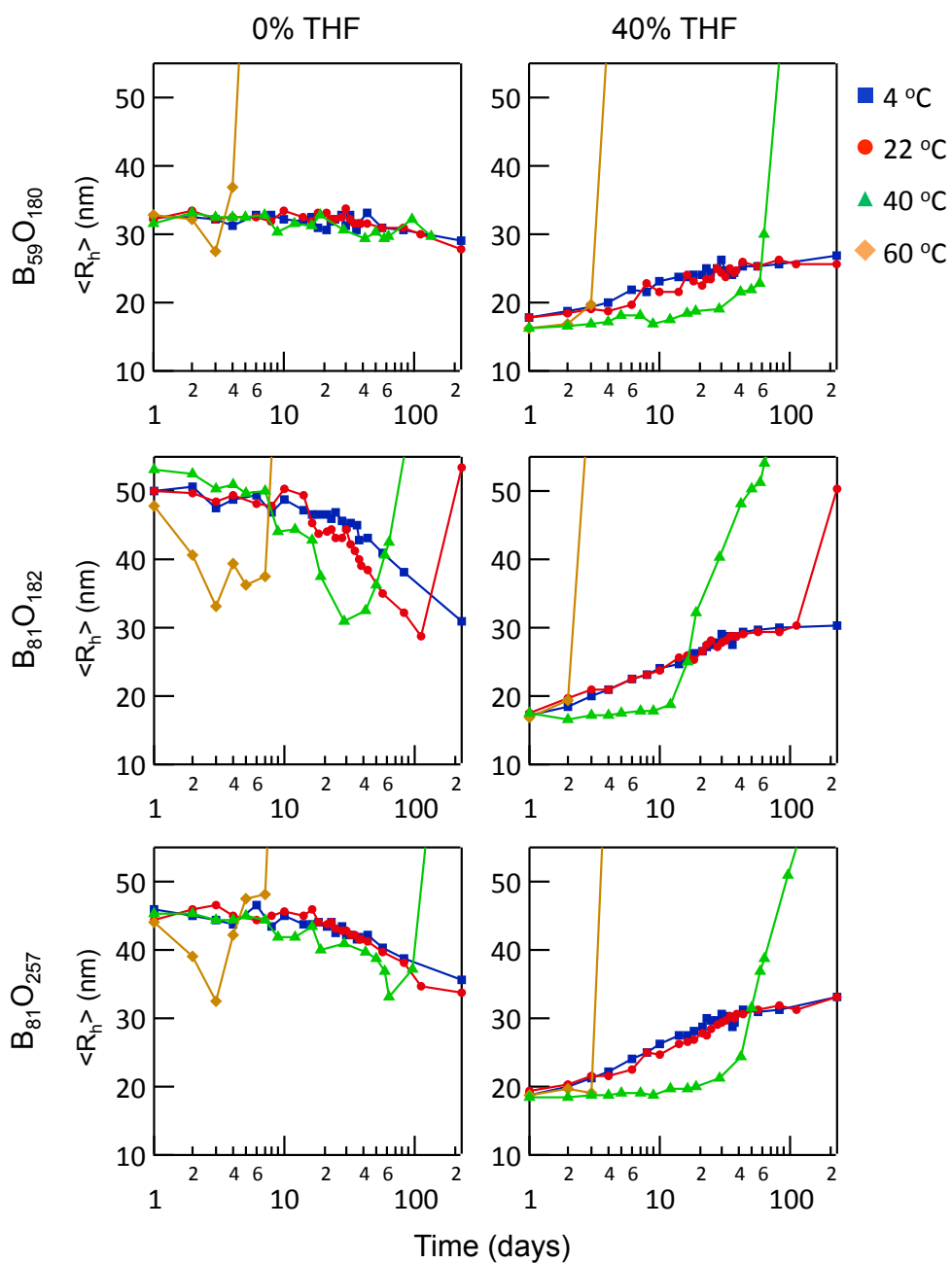


Figure 4.6. Temperature and molecular weight dependence of micelle size evolution. Rearranged presentation of data in Figure 4.3 to highlight the effect of temperature. For 0 wt% THF samples, solutions stirred at higher temperature led to faster size decreases and eventually to polymer precipitation. For 40 wt% THF samples, increasing temperature led to slower micelle growth and eventual precipitation.

Contrary to the increased rate of micelle breakage with higher temperatures, the rate of micelle growth was slower with increasing temperature. Micelles perturbed to smaller sizes (40 wt% THF) exhibited a nearly constant  $R_h$  (~18 nm) for 10 to 30 d at 40 °C, depending on the molecular weight. Assuming the micelles were undergoing a fusion-based growth mechanism suggested in Ch. 3, there are several proposed arguments for the slower growth kinetics with increasing temperature. Based on the high number of expected micelle collisions due to diffusion ( $\sim 10^4$  collisions/s at 25 °C), there must be a low probability for micelle coalescence and consequently a large energetic barrier for growth in bulk solution. While increasing temperature will increase the particle diffusivity and rate of collisions, the rise in temperature also seems to increase the energetic barrier, based on the apparent slower growth in  $R_h$ . One speculation is an increase in steric stabilization from the collapsing PEO corona at elevated temperatures. Although water acts a good solvent for PEO near room temperature, increasing temperature lowers the solvent quality for PEO, resulting in corona dehydration and collapsing PEO chains.<sup>15,16</sup> Presumably, an increase in affinity for PEO-PEO interactions and an increase in the corona chain density could produce a higher energetic barrier for fusion. Alternatively, the finding could be due to a lower air-water interfacial tension ( $\sim 73$  mN m<sup>-1</sup> at 20 °C and  $\sim 66$  mN m<sup>-1</sup> at 60 °C) and lower water viscosity at elevated temperatures (1.002 cP at 20 °C and 0.467 cP at 60 °C),<sup>17</sup> which may affect the growth process given the observed dependence on shear and interfacial effects.

Another interesting trend demonstrated in Fig. 4.6 was the sharp increase in  $R_h$  after a finite induction period at 40 °C and 60 °C. This trend was found for both the

0 wt% and 40 wt% THF samples. By visual inspection, the solution became slightly cloudy prior to the sudden increase in  $R_h$ . Once  $R_h$  exceeded  $\sim 60$  nm, there were visible polymer precipitates in solution, and the solution became white. The induction period prior to polymer precipitation was fairly consistent in a repeated trial at 40 °C (see Appendix A, Figure A.9).

After failed attempts to re-dissolve the dried  $B_{81}O_{182}$  in THF (good solvent for PB-PEO), it was assumed that the rapid increase in  $R_h$  at 40 °C and 60 °C was due to cross-linking or degradation of alkene groups within the PB micelle core (see Appendix A, Figure A.10a). SEC analysis showed that  $B_{81}O_{182}$  micelle solutions at 4 °C did not cross-link over the examined time (see Appendix A, Figure A.10b). PB cross-linking would significantly affect chain dynamics, leading to destabilized micelles and large aggregates. Accordingly, the rate of cross-linking would be expected to increase with temperature and aeration (oxidation), leading to the faster precipitation shown in Fig. 4.6. The significant size changes due to polymer degradation are discussed further in the following section.

#### **4.2.4 Morphological transition and aggregation**

One consequence of examining block polymer micelle kinetics at elevated temperatures was the sudden precipitation of polymer, evidenced by the rapid increase in  $R_h$  in Figure 4.6. One sample prone to faster precipitation at 40 °C ( $B_{81}O_{182}$ , 40 wt% THF) was examined with cryo-TEM to identify structural changes. Figure 4.7 (left) showed a similar bimodal distribution of smaller and larger spherical micelles after stirring for 19 d at 40 °C. Day 19 corresponded to the beginning of the abrupt increase in  $R_h$  (Fig. 4.6). However, by Day 51, a drastic increase hydrodynamic radius from  $R_h \sim 25$  nm to  $R_h \sim 50$  nm was indicative of a morphological transition, as shown

in Fig. 4.7b. The mixed morphology on Day 51 included toroids, larger spheres, and cylindrical micelles.

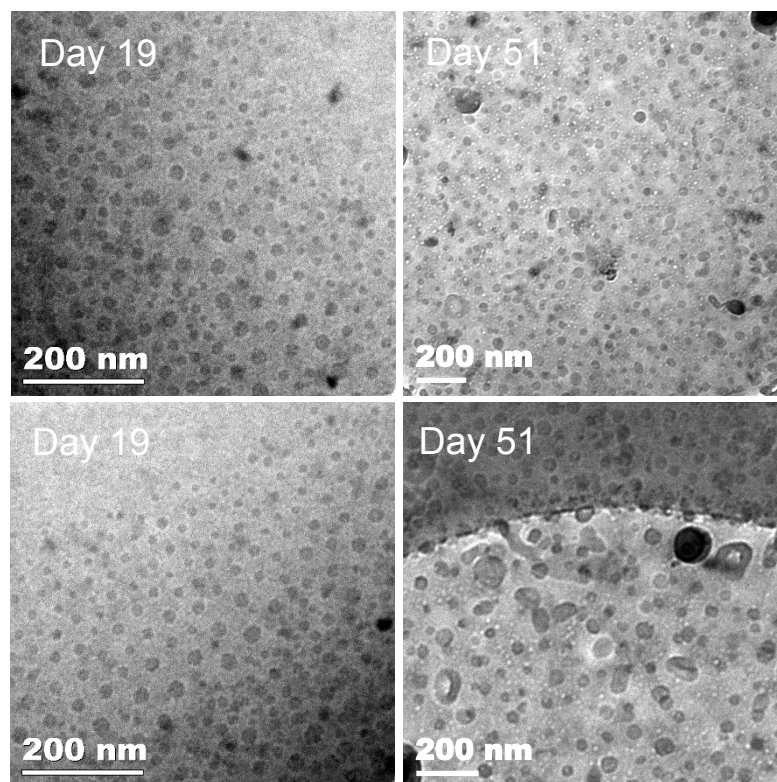


Figure 4.7. Morphological transitions during micelle size evolution. Cryo-TEM images of  $B_{81}O_{182}$  prepared at 40 wt% THF and  $10 \text{ mg mL}^{-1}$  prior to dialysis. Aqueous micelle solutions were stirred at  $40 \text{ }^\circ\text{C}$  for 19 d (left) and 51 d (right). Distinctly different morphologies such as cylinders and toroids were observed after 51 d at  $40 \text{ }^\circ\text{C}$ . Morphological changes and subsequent polymer precipitation was likely due to cross-linking of the PB cores accelerated by elevated temperatures and aeration from stirring.

The assumed cross-linking of the PB core block was likely the reason for the morphological transition and ultimate precipitation (Appendix A, Figure A.10). As the extent of cross-linking presumably increased over time at elevated temperatures,

the effective increase in  $N_{PB}$  as well as added entanglement and reduced mobility of PB could trigger a change in morphology to balance the altered interfacial area and chain stretching of the core and corona chains. The toroid and cylindrical micelles possibly were metastable intermediates before the phase separation into large precipitated particles. Based on the elevated temperature studies, the long-term fate of PB-based micelles is the formation of cross-linked polymer and ultimately unstable solution structures. Future long-term micelle stability studies should explore PB-PEO analogs, such as PEE-PEO, that have low  $T_g$  and low entanglements ( $T_g \sim -20$  °C,  $M_e \sim 9.5$  kg mol<sup>-1</sup>).<sup>18</sup> Prior conversion of the reactive alkene groups in PB to non-reactive alkane groups in PEE (catalytic hydrogenation)<sup>19</sup> can avert the effects of cross-linking and polymer degradation on the micelle dynamics at elevated temperatures.

### 4.3 Fast Micelle Relaxation Kinetics

Long-term kinetic studies of PB-PEO micelles spanning ( $> 200$  d) were performed to distinguish trends in molecular weight and temperature; however, the long-term experiments were inconvenient and led to issues with polymer degradation at elevated temperatures. It was postulated that the timescale for chain exchange could be reduced through more vigorous methods of agitation. Hence, the samples were reexamined with alternative agitation methods. Figure 4.8a demonstrated that micelle growth kinetics ( $B_{81}O_{182}$ , 40 wt% THF) could occur significantly faster through rapid vortex mixing ( $\sim 10^5$  times faster than magnetic stirring). The change in average  $R_h$  over time showed a similar decaying exponential growth (Eq. 4.1) that was highly dependent on the work input into the system via vortex mixing. Figure 4.8b illustrated an initial increase in the size polydispersity, followed by a maximum and subsequent decrease in polydispersity over time.

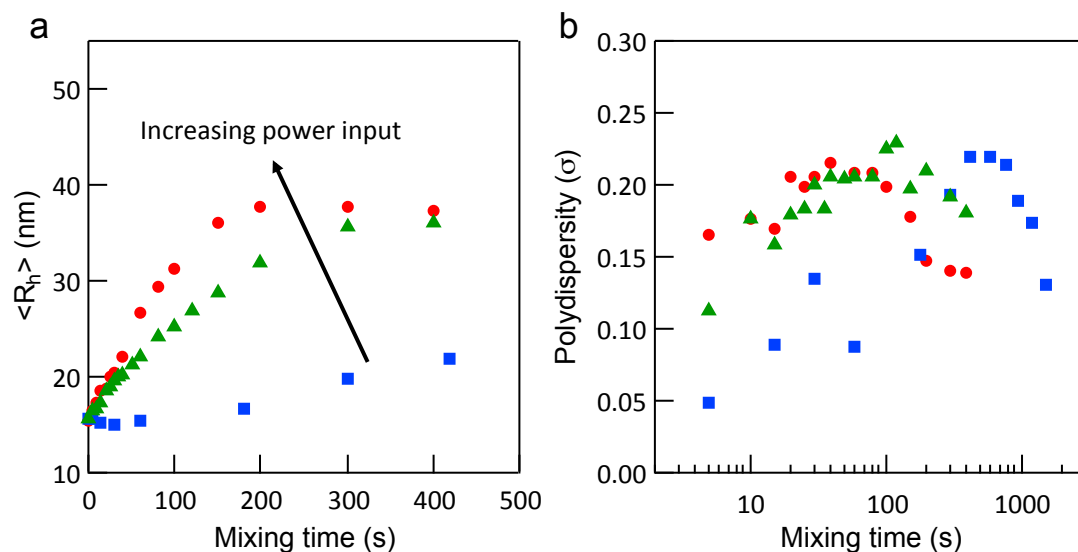


Figure 4.8. Micelle growth from rapid vortex mixing. (a) Effective hydrodynamic radius increases as a function of vortex mixing time for  $B_{81}O_{182}$  micelles in water (40 wt% THF before dialysis). The relaxation time scale was significantly lower compared to magnetically stirred solutions, showing a trend of decreasing characteristic time with increasing power input. (b) Fitted polydispersity parameters from the quadratic cumulant method showed an increase and subsequent decrease as a function of vortex mixing time.

The decaying-exponential size relaxation and polydispersity trend determined by DLS were consistent with previous investigations that identified a shifting bimodal size distribution. Therefore, cryo-TEM was used to confirm if the accelerated growth process followed a similar bimodal pathway. Figure 4.9 showed representative images of a micelle solution ( $B_{81}O_{182}$ , 40 wt% THF) vortexed for 60 s at  $\sim 3200$  rpm, which confirmed that the accelerated micelle growth was also occurring through a bimodal pathway. This result was significant for two reasons: (1) it provided a much more experimentally convenient method for fundamental studies of size evolution on a

shorter timescale, and (2) it established a simple route to tune the timescale of dynamic processes.

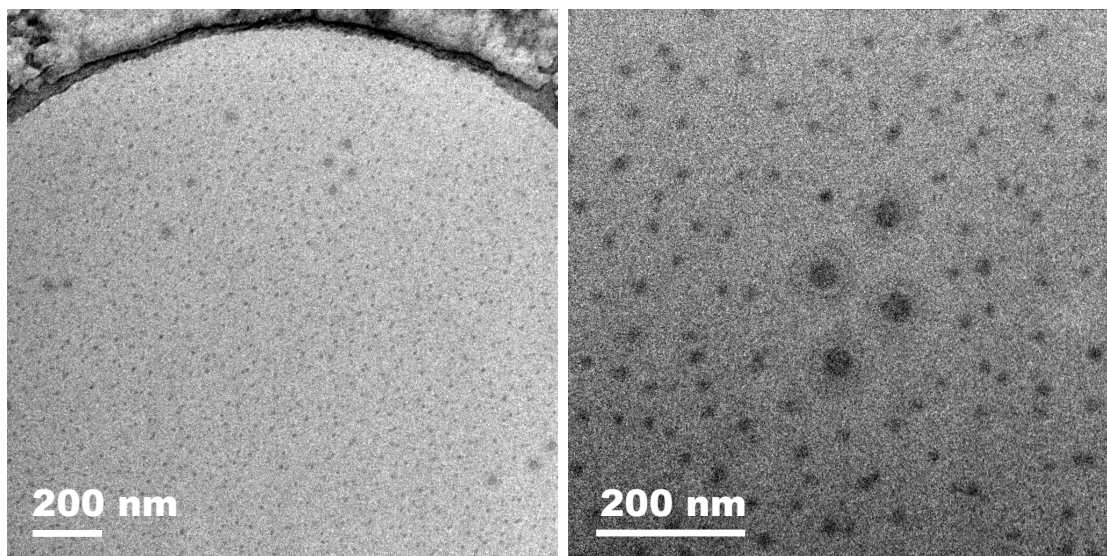


Figure 4.9. Cryo-TEM images of micelle growth from rapid vortex mixing.  $B_{81}O_{182}$  micelle solutions (40 wt% THF before dialysis to water) were imaged after 60 s of rapid vortex mixing. A bimodal distribution of micelle sizes was observed similarly to magnetically stirred micelle solutions.

Micelle growth kinetics with various mixing methods and various molecular weights were plotted on the same semi-log plot, as shown in Figure 4.10a. From a given initial size  $R_i \sim 17$  nm at room temperature, it was clear that both the molecular weight and type of agitation played a role in the steady state or final size  $R_f$ . For example, increasing the molecular weight from  $B_{59}O_{180}$  to  $B_{81}O_{182}$  or  $B_{81}O_{257}$  led to an increase in  $R_f \sim 25$  nm to  $R_f \sim 32$  nm when stirring at 200 rpm. The characteristic time also roughly doubled from  $\sim 7$  d to  $\sim 14$  d with the examined increase in molecular weight. More interestingly, rapid vortex mixing of  $B_{81}O_{182}$  solutions led to an increase

in final size from  $R_f \sim 30$  nm to  $R_f \sim 37$  nm, as compared to magnetic stirring. This result reiterated the importance of kinetically-controlled self-assembly, demonstrating that the steady-state micelle size and true equilibrium micelle size are not always equivalent. The increase in  $R_f$  suggested a different mechanism for chain exchange occurred in the case of rapid vortex mixing compared to magnetic stirring. With a method to control micelle relaxation kinetics on a more reasonable experimental timescale, new possibilities existed for investigating micelle chain exchange kinetics in aqueous solutions (Ch. 5).

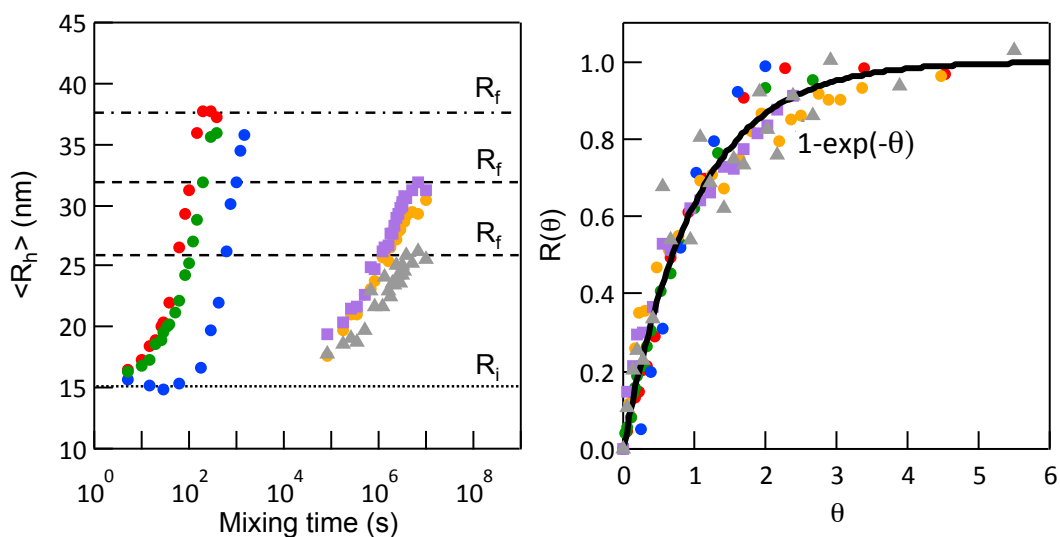


Figure 4.10. Comparison of timescales and final micelle hydrodynamic radii ( $R_f$ ) for micelle solutions after rapid vortex mixing (red, green, blue) and magnetic stirring (purple, orange, gray). The agitation rate and polymer molecular weight for  $B_{59}O_{180}$  (triangles),  $B_{81}O_{182}$  (circles), and  $B_{81}O_{257}$  (squares) led to distinct relaxation timescales and final radii (left). A dimensionless plot followed an exponential relaxation curve from Eq. 4.1 (right).

Dimensionless analysis (Fig. 4.10b) was achieved by normalizing DLS results using dimensionless time,  $\theta = t/\tau$ , in which  $\tau$  is the characteristic relaxation time, and dimensionless size,  $R(\theta) = (R(t) - R_i)/(R_f - R_i)$ , in which  $t$  is the mixing time (Eq. 4.1). A similar decaying exponential trend was observed for different types of mixing and molecular weight. This dimensionless analysis was encouraging in that the phenomena for size growth of “frozen” micelles in aqueous solutions could be generalized to the form  $R(\theta) = 1 - \exp(-\theta)$ . However, this relationship was still based on growth of intensity-weighted micelle distributions instead of number-weighted distributions, which complicates the quantification of underlying rate expressions. Thus, the consistent trend shown in Fig. 4.10b requires additional validation by quantifying growth kinetics with SANS, exploring greater ranges in molecular weight, and using controlled agitation methods.

#### 4.4 Chapter Summary

The results presented in this chapter provided useful insight into the growth and breakage mechanisms of highly amphiphilic block polymer micelles in aqueous solutions. Despite previous experiments that showed PB-PEO micelles were kinetically-frozen in bulk water under quiescent conditions, these results further confirmed that micelles can evolve over reasonable timescales given sufficient perturbation and agitation.

The block polymer molecular weight and solution temperature affect the thermodynamics and kinetics for micelle chain exchange. In general, increasing molecular weight led to larger micelles upon direct dissolution of PB-PEO (0 wt% THF), and these larger micelles eventually broke apart into smaller micelles with agitation. An increase in molecular weight also increased the characteristic time

for micelle growth (40 wt% THF) according to DLS and cryo-TEM data. A similar bimodal size distribution was observed for all three molecular weight species.

Solution temperature considerably affected the timescale for micelle growth and breakage of agitated micelle solutions. In general, increasing the temperature from 4 °C to 60 °C resulted in faster breakage of micelles directly dispersed in water (0 wt% THF) and slower growth of cosolvent-perturbed micelles (40 wt% THF before dialysis). Furthermore, higher temperatures eventually induced morphological transitions polymer precipitates, likely due to cross-linking and degradation of the PB block. Repeating long-term kinetic experiments with an analogous polymer (PEE-PEO) would be necessary to avoid effects of polymer degradation.

The necessity of solution agitation for micelle growth or breakage suggested a shear-induced and/or interfacial pathway for chain exchange. By operating within shorter timescales (min), vigorous solution agitation methods such as rapid vortex mixing offer a more practical method to investigate the stability highly amphiphilic micelles in aqueous solutions. Importantly, shear and interfacial surface turnover rates can differ drastically based on the mixing method, as shown for magnetic stirring and vortex mixing.<sup>20</sup> This critical dependence on solution agitation set the foundation for Ch. 5, which further explores the effect of flow on micelle chain exchange in aqueous solutions.

## REFERENCES

- 1 Lund, R., Willner, L. & Richter, D. Kinetics of Block Copolymer Micelles Studied by Small-Angle Scattering Methods. *Advances in Polymer Science* **259**, 51-158 (2013).
- 2 Zhulina, E. B., Adam, M., LaRue, I., Sheiko, S. S. & Rubinstein, M. Diblock copolymer micelles in a dilute solution. *Macromolecules* **38**, 5330-5351 (2005).
- 3 Lund, R., Willner, L., Stellbrink, J., Lindner, P. & Richter, D. Logarithmic chain-exchange kinetics of diblock copolymer micelles. *Physical Review Letters* **96**, 068302 (2006).
- 4 Choi, S. H., Lodge, T. P. & Bates, F. S. Mechanism of molecular exchange in diblock copolymer micelles: hypersensitivity to core chain length. *Physical Review Letters* **104**, 047802 (2010).
- 5 Lu, J., Bates, F. S. & Lodge, T. P. Chain Exchange in Binary Copolymer Micelles at Equilibrium: Confirmation of the Independent Chain Hypothesis. *ACS Macro Letters* **2**, 451-455 (2013).
- 6 Lu, J., Choi, S., Bates, F. S. & Lodge, T. P. Molecular Exchange in Diblock Copolymer Micelles: Bimodal Distribution in Core-Block Molecular Weights. *ACS Macro Letters* **1**, 982-985 (2012).
- 7 Meli, L. & Lodge, T. P. Equilibrium vs metastability: High-temperature annealing of spherical block copolymer micelles in an ionic liquid. *Macromolecules* **42**, 580-583 (2009).
- 8 Meli, L., Santiago, J. M. & Lodge, T. P. Path-dependent morphology and relaxation kinetics of highly amphiphilic diblock copolymer micelles in ionic liquids. *Macromolecules* **43**, 2018-2027 (2010).
- 9 Nicolai, T., Colombani, O. & Chassenieux, C. Dynamic polymeric micelles versus frozen nanoparticles formed by block copolymers. *Soft Matter* **6**, 3111-3118 (2010).
- 10 Won, Y. Y., Davis, H. T. & Bates, F. S. Molecular exchange in PEO-PB micelles in water. *Macromolecules* **36**, 953-955 (2003).

- 11 Lund, R., Willner, L., Richter, D. & Dormidontova, E. E. Equilibrium chain exchange kinetics of diblock copolymer micelles: Tuning and logarithmic relaxation. *Macromolecules* **39**, 4566-4575 (2006).
- 12 Zhulina, E. B. & Borisov, O. V. Theory of Block Polymer Micelles: Recent Advances and Current Challenges. *Macromolecules* **45**, 4429-4440 (2012).
- 13 Dormidontova, E. E. Micellization kinetics in block copolymer solutions: Scaling model. *Macromolecules* **32**, 7630-7644 (1999).
- 14 Brandrup, J. & Immergut, E. H. *Polymer Handbook*. 3rd edn, Vol. VI 414-426 (Wiley-Interscience, 1989).
- 15 Kumbhakar, M., Goel, T., Nath, S., Mukherjee, T. & Pal, H. Microenvironment in the Corona Region of Triblock Copolymer Micelles: Temperature Dependent Solvation and Rotational Relaxation Dynamics of Coumarin Dyes. *The Journal of Physical Chemistry B* **110**, 25646-25655 (2006).
- 16 Behrens, M. A., Bergenholtz, J. & Pedersen, J. S. Temperature-Induced Attractive Interactions of PEO-Containing Block Copolymer Micelles. *Langmuir* **30**, 6021-6029 (2014).
- 17 *CRC Handbook of Chemistry and Physics*. 95th edn, (Taylor & Francis Group, 2014).
- 18 Won, Y.-Y., Brannan, A. K., Davis, H. T. & Bates, F. S. Cryogenic Transmission Electron Microscopy (Cryo-TEM) of Micelles and Vesicles Formed in Water by Poly(ethylene oxide)-Based Block Copolymers. *The Journal of Physical Chemistry B* **106**, 3354-3364 (2002).
- 19 Hillmyer, M. A. & Bates, F. S. Synthesis and characterization of model polyalkane-poly(ethylene oxide) block copolymers. *Macromolecules* **29**, 6994-7002 (1996).
- 20 Bai, G., Bee, J. S., Biddlecombe, J. G., Chen, Q. & Leach, W. T. Computational fluid dynamics (CFD) insights into agitation stress methods in biopharmaceutical development. *International Journal of Pharmaceutics* **423**, 264-280 (2012).

## Chapter 5

### MICELLE CHAIN EXCHANGE INDUCED BY FLOW

Chapter 5 explores shear and interfacial effects on micelle size evolution in aqueous solutions. Various common laboratory methods for solution agitation and controlled methods for applying shear flow were investigated to decouple shear and interfacial effects. With the ability to control and lower the chain exchange timescale through the rate of agitation, SANS methods were used to quantify exchange kinetics and establish an improved understanding of the underlying chain exchange mechanisms induced by flow. Reproduced with permission from *ACS Macro Letters*, submitted for publication. Unpublished work copyright 2014 American Chemical Society.

#### 5.1 Introduction

Chapters 3 and 4 demonstrated the importance of solution agitation on micelle size evolution. Specifically, Chapter 3 showed that the extent of perturbation through cosolvent switches determined a regime where micelles either remained kinetically trapped or grew through a bimodal distribution. Chapter 4 investigated important parameters, namely molecular weight and temperature, which affect micelle relaxation timescales. Both of these investigations showed that under quiescent conditions, poly(butadiene-*b*-ethylene oxide) (PB-PEO) micelles remained stable as expected from previous reports on the non-ergodicity of highly hydrophobic core blocks in water.<sup>1,2</sup> While these systems appear completely frozen under quiescent conditions,

many envisioned applications that employ block polymer micelles as nanocontainers, for example as drug delivery vehicles, generally operate under flowing conditions. Thus, a better understanding of micelle stability under flow was necessary to explain the unexpected micelle size evolution and chain exchange in aqueous solutions.

The exposure of block polymer micelles to shear flow has not gone completely unexplored. Stellbrink *et al.* used Rheo-SANS to examine the effect of shear flow on kinetically frozen PEP-PEO block polymer micelles in water.<sup>3</sup> Micelle interactions were induced by flow, as indicated by the appearance of a structure factor that was dependent on the shear rate, polymer concentration, and polymer molecular weight. Interestingly, solutions of star-like micelles at sufficiently high shear rates and concentrations showed a tilted elongation along the flow direction, suggesting that shear could affect the stability of kinetically-frozen block polymer assemblies. Other investigations by Wang *et al.* used microfluidic devices to impose shear-induced morphology transitions of PS-PAA block polymers from spheres to cylinders and vesicles, as well as the breakage of larger cylindrical micelles into spheres.<sup>4,5</sup>

Considerable efforts to understand the influence of shear and interfacial effects on nanoscale assemblies have focused generally on emulsions and protein solutions used in personal care products and pharmaceuticals.<sup>6-12</sup> Similar shear and interfacial effects are encountered in micelle formulations with intended use in drug delivery or catalysis applications. The agitation experienced during processing, shipping, or usage of these nanoscale solution assemblies can induce aggregation and undesirable changes in the size, structure, and function of the nanocarrier. As a result, there is a need to better understand and quantify the effects of routine agitation on micelle chain exchange.

This chapter explores shear and interfacial effects on the chain exchange of PB-PEO block polymer micelles in water. SANS and contrast-matching techniques were employed to quantify the extent of chain exchange between micelles as a result of agitation. Specifically, the various routine agitation methods included cone-plate flow, Couette flow, nitrogen gas sparging, and rapid vortex mixing (5.2). These methods enabled the distinction between agitation effects with limited interfacial contact (i.e. cone-plate flow and Couette flow) and agitation effects with significant interfacial contact (i.e. sparging and vortexing). The results from rapid vortex mixing were quantified at various polymer concentrations to establish the kinetics of chain exchange (5.3). Finally, the relevance of shear and interfacial effects on micelle chain exchange are discussed in the context of other amphiphilic systems (5.4).

## **5.2 Shear and Interfacial Effects on Chain Exchange**

Micelle growth revealed in Ch. 3 and 4 was shown to be entirely dependent on stirring. Subsequently, various mixing methods were employed to decouple shear and interfacial effects. Controlled flow methods with minimal air-water interfacial contact were used to distinguish between these two effects, such as flow obtained from stress- or strain-controlled rheometers with cone-plate (5.2.1) or Couette geometries (5.2.2). Subsequent methods that generate significantly more air-water interfacial area, such as gas sparging (5.2.3) and rapid vortex mixing (5.2.4), were used to further explore the dependence on the air-water interface.

### **5.2.1 Cone-plate flow**

Cone-plate experiments were carried out to establish appropriate shear rates and acquisition times for subsequent flow-SANS experiments. PB-PEO micelle

solutions ( $5 \text{ mg mL}^{-1}$ ,  $\text{B}_{81}\text{O}_{182}$  dialyzed to water from 40 wt% THF) were sheared in a cone-plate rheometer for 5 min intervals and subsequently analyzed using DLS.

Fig. 5.1 shows shifts in the autocorrelation function to longer correlation times as a result of shear flow. This shift indicated a micelle size increase after a 5 min exposure to shear at  $3000 \text{ s}^{-1}$ , and a greater size increase after a 5 min exposure at  $7000 \text{ s}^{-1}$ . The same sample vortexed at  $\sim 3200 \text{ rpm}$  for 5 min showed a comparatively larger micelle size. Nevertheless, these preliminary DLS results showed the expected process timescale was on the order of minutes to hours ( $3000\text{-}7000 \text{ s}^{-1}$ ). This was the targeted experimental time window, and these were the shear rates used in subsequent Flow-SANS experiments.

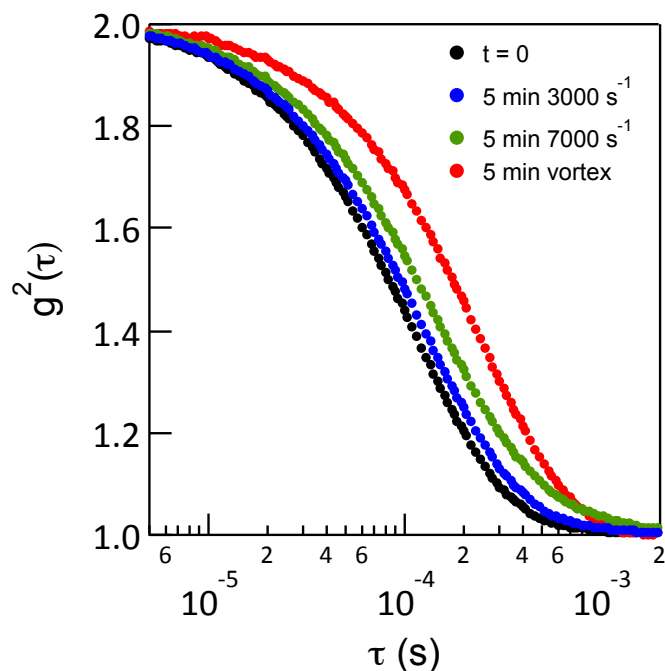


Figure 5.1. DLS autocorrelation function of  $B_{81}O_{182}$  micelle solutions (40 wt% THF pre-dialysis) after shear flow in a cone-plate rheometer. An increase in micelle size after 5 min of shear (shift to larger correlation time) suggested that micelle size evolution could be accelerated with increasing shear rate.

### 5.2.2 Couette flow

Experiments to probe the influence of shear flow were necessary to understand the underlying mechanism for micelle growth. One hypothesis was that micelles were flocculating or agglomerating under shear flow before coalescing into larger, more stable micelles. In particular, the appearance of a structure factor peak near  $q \sim 0.02 \text{ \AA}^{-1}$  would be expected if the micelles were “sticking” together or flocculating during flow. With dilute solutions, a structure factor was not expected under quiescent conditions as shown previously. Thus, for the appearance of a micelle structure factor under dilute conditions, the strength of the induced attractive interaction between

micelles would need to be very strong. Periodic time points under quiescent conditions (stop-flow) were captured over a wide  $q$ -range to investigate the progression of the micelle form factor over time.

Flow-SANS was performed by scattering off a micelle solution within rotating concentric cylinders oriented in the 1-3 plane (Ch. 2.3.4). Figure 5.2a showed the Flow-SANS result of shearing for 20 min each at  $3000\text{ s}^{-1}$ ,  $5000\text{ s}^{-1}$ , and  $7000\text{ s}^{-1}$ . Note that the scattering data was isotropic, suggesting no flow induced particle alignment. Periodically after 20 min, the flow was stopped to capture a wider  $q$ -range and to examine changes in the micelle core form factor (Fig. 5.2b). Contrary to the size changes determined from the cone-plate experiments with DLS, neither measurable changes in structure factor nor any measurable changes in form factor occurred after flowing for 60 min. This result implied that the proposed mechanism for shear-induced flocculation was not occurring over the examined timescales.

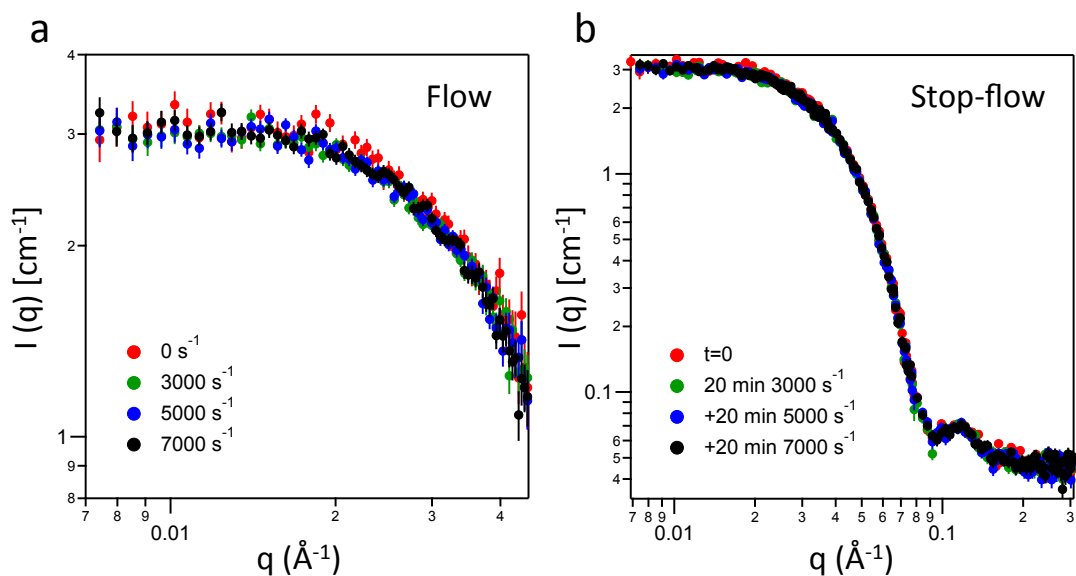


Figure 5.2. Flow-SANS results for corona-matched blended PB-*h*PEO/PB-*d*PEO micelles (40 wt% THF pre-dialysis). Scattered intensity from micelle cores did not change significantly under flow (a) or after stopping flow after 60 min at high shear rates (b). The lack of particle interactions or structure factor suggested flocculation and aggregation was not occurring. Furthermore, no changes in micelle core size suggested sufficient air-water interface was necessary for chain exchange. The error bars represent the standard deviation.

For micelles near their equilibrium size ( $B_{59}O_{180}$  or  $B_{59}dO_{163}$  in  $D_2O/H_2O$ ), there was no decrease in the intensity after shearing for 90 min at  $5000\text{ s}^{-1}$ , suggesting negligible chains had exchanged between micelles (Fig. 5.3). With shear flow appearing to have no effect on solution structure, micelle size, or chain exchange, the results suggested that micelle growth and chain exchange was not solely a shear-induced phenomenon.

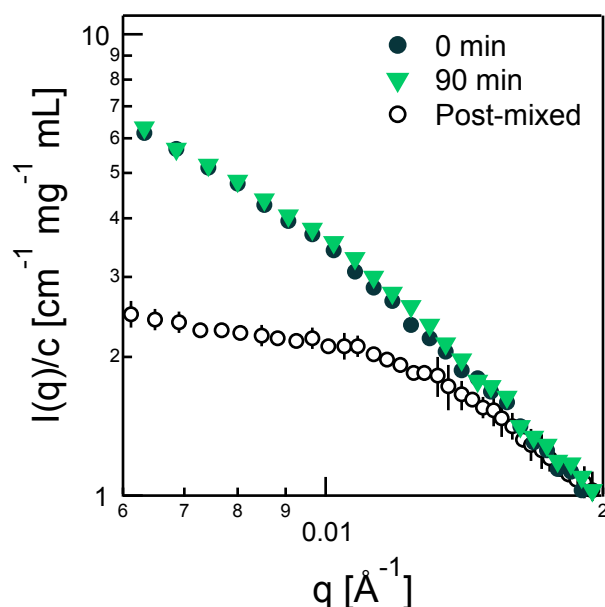


Figure 5.3. SANS experiment to quantify chain exchange due to Couette flow. The lack of decrease in intensity suggested negligible chain exchange occurred after flowing for 90 min at  $5000 \text{ s}^{-1}$ . The 0 min sample and pre-mixed sample are averaged scattering intensities of three micelle concentrations. The error bars represent the standard deviation.

It was reasoned that another key parameter must be involved in the micelle growth process, most likely the air-water interface. The discrepancy between no observed micelle growth (Couette flow) and preliminary micelle growth (cone-plate flow) could be due to the differences in the ratio of solution volume to air-water contact area (i.e. cone-plate flow had higher air-water interfacial area to volume ratio than Couette flow). Therefore, new methods to induce chain exchange between micelles through deliberate interfacial contact, such as nitrogen gas sparging, were attempted to control the amount of air-water surface area.

### 5.2.3 Nitrogen gas sparging

By ruling out the possibility of shear-induced flocculation, it was hypothesized that the micelle growth found previously (Fig. 3.1, Fig. 4.3, and Fig. 4.8) was due to interfacial aggregation. Bubbling nitrogen gas through a micelle solution at a controlled flow rate of nitrogen ( $10 \text{ mL min}^{-1}$ ) allowed the amount of generated gas-liquid surface area to be approximated through a simple geometric estimation. With a flow rate of  $10 \text{ mL min}^{-1}$  and an average gas bubble diameter of  $\sim 3 \text{ mm}$ , the air-water surface area generated per second was on the order of  $1 \text{ cm}^2 \text{ s}^{-1}$ , assuming the bubble retained a spherical shape before collapsing into the bulk.

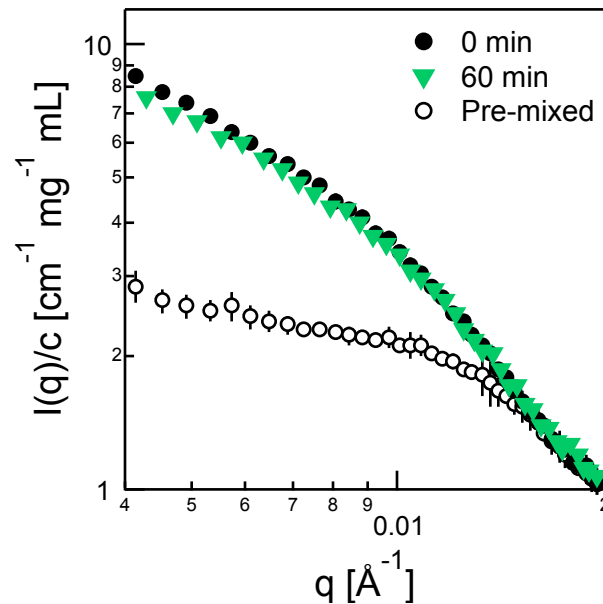


Figure 5.4. SANS experiment to quantify chain exchange due to gas sparging. The lack of decrease in intensity suggested negligible chain exchange occurred after 60 min mixing by nitrogen gas sparging. The 0 min sample and pre-mixed sample are averaged scattering intensities of three micelle concentrations. The error bars represent the standard deviation.

Figure 5.4 shows that there was no significant chain exchange between micelles after 60 minutes of nitrogen gas sparging. It was suspected that perhaps the surface turnover rate was still too low to measure significant chain exchange. For future investigations, increasing the nitrogen flow rate would increase the surface regeneration rate. Additionally, the sparging time should be extended to determine if chain exchange occurs over a longer timescale (i.e. on the order of days). However, another simple approach (rapid vortex mixing) was employed due to the significantly higher surface regeneration rate ( $\sim 10^2 \text{ cm}^2 \text{ s}^{-1}$ ).<sup>9</sup>

#### **5.2.4 Rapid vortex mixing**

All previous mixing methods (magnetic stirring, Couette flow, and nitrogen gas sparging) did not induce chain exchange in micelles up to the longest examined timescale (10 d, 90 min, and 60 min, respectively). These methods are estimated to have low air-water surface turnover rates ( $\sim 1 \text{ cm}^2 \text{ s}^{-1}$  or less). Meanwhile, rapid vortex mixing is known to generate high volume average shear rates, high shear rates near air-water interfaces, and high surface generation rates depending on the rate of agitation. A computational fluid dynamic study of vortex mixing 1 mL of water in a glass vial at 1000 rpm estimated a volume average shear rate ( $400 \text{ s}^{-1}$ ), average shear rate at air-water interface ( $200 \text{ s}^{-1}$ ), and air-water surface generation rate ( $200 \text{ cm}^2 \text{ s}^{-1}$ ). The vortex mixer used in the following experiments operated at even higher rates of agitation ( $\sim 3200 \text{ rpm}$ ), and hence these estimates suggested at least two orders of magnitude greater surface turnover compared to other attempted agitation methods.

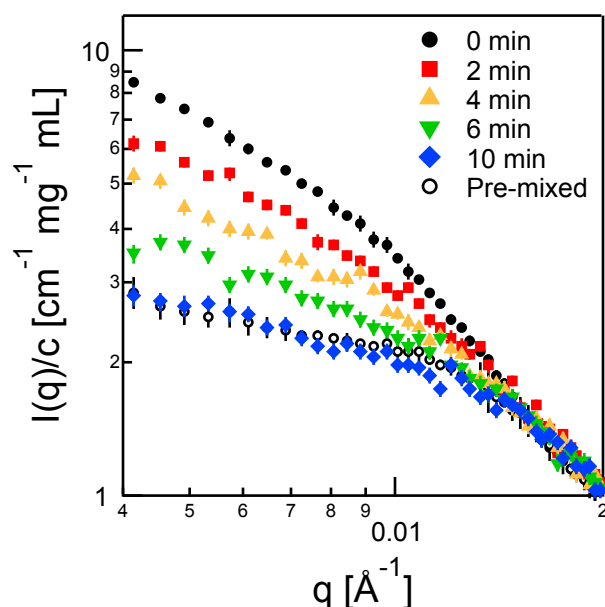


Figure 5.5. SANS experiment to quantify chain exchange due rapid vortex mixing. The decrease in intensity over minutes demonstrated that rapid vortex mixing could lead to chain exchange between micelles ( $B_{59}O_{180}$  and  $B_{59}dO_{163}$  in  $D_2O/H_2O$ ,  $2.4 \text{ mg mL}^{-1}$ ). The fraction of chains exchanged could be quantified according to Eq. 5.1. The 0 min sample and pre-mixed sample are averaged scattering intensities of three micelle concentrations. The error bars represent the standard deviation.

Figure 5.5 showed that rapid vortex mixing PB-PEO micelles ( $B_{59}O_{180}$  and  $B_{59}dO_{163}$  in  $D_2O/H_2O$ ,  $2.4 \text{ mg mL}^{-1}$ ) resulted in a significant drop in scattered intensity over 10 min, which demonstrated chain exchange between micelles could be induced in aqueous solutions. The random chain exchange assumptions and conditions leading to decreasing intensity over time were described previously (2.2.4).

An order-of-magnitude approximation was based on the air-water surface turnover rate induced by rapid vortex mixing. At a polymer concentration of  $2.4 \text{ mg mL}^{-1}$ , there are approximately  $10^{14}$  micelles in 1 mL with  $Q \sim 800$  (0% THF).

Assuming each micelle occupies an area  $\sim 10^4 \text{ nm}^2$  (100 nm x 100 nm) at the interface, and the surface turnover rate is  $\sim 200 \text{ cm}^2/\text{s}$ , the expected timescale for complete exchange of chains between all micelles is  $\sim 1 \text{ min}$ . This estimate was fairly consistent with the timescale for full chain exchange (10 min), especially given several necessary assumptions. Specifically, it was assumed that micelles adsorb quickly to newly generated air-water interface (i.e. interface at a given moment without adsorbed polymer). This assumption is reasonable based on the fast timescale ( $\sim 10^{-4} \text{ s}$ ) for micelles to diffuse on the order of micelle spacing in solution ( $\sim 100 \text{ nm}$ ) compared to the process timescale. However, there may be an energy barrier hindering the rate of micelle adsorption to the interface, possibly leading to an overestimation of the number of micelles at an interface and hence an underestimation of the timescale. Furthermore, the unverified assumption that micelles completely mix chains at the interface after surface regeneration may be inaccurate. The chain exchange process could be stepwise, implying that only a small fraction of chains exchange with each interfacial encounter. For example, if only 10% of the chains were randomly mixed after a surface turnover event, then the process would take on average ten times as long. This scenario again would lead to an underestimation of the process timescale. Finally, the surface turnover rate for vortex mixing from computational fluid dynamic simulations<sup>9</sup> could differ significantly from reality, especially given differences in vial size, air headspace, and the rate of agitation (3200 rpm vs. 1000 rpm). Knowing that these factors will affect the timescale for chain exchange, a simple estimation nevertheless agreed reasonably with the experimental timescale, suggesting the rate of chain exchange was surface limited.

### 5.3 Fast Chain Exchange for Rapid Vortex Mixing

As shown in Fig. 4.10, rapid vortex mixing led to micelle relaxation and growth through a bimodal pathway that was five orders of magnitude faster than the rate in magnetically stirred solutions. Furthermore, Fig. 5.5 demonstrated that rapid vortex mixing micelle solutions near their equilibrium size could induce chain exchange. This drastic difference in chain exchange timescale was hypothesized to depend on high air-water surface turnover rates coupled to high shear rates.

If the rate of chain exchange between micelles near equilibrium was related to the air-water interfacial area, then the rate should depend on the available air/liquid volume ratio. Figure 5.6a showed that significantly slower chain exchange occurred for the same vial containing 4 mL of solution as compared to 1 mL of solution (both at  $5 \text{ mg mL}^{-1}$ ). This result supported the argument that air-water contact area was a critical factor for chain exchange. Subsequent experiments used 1 mL solution volume.

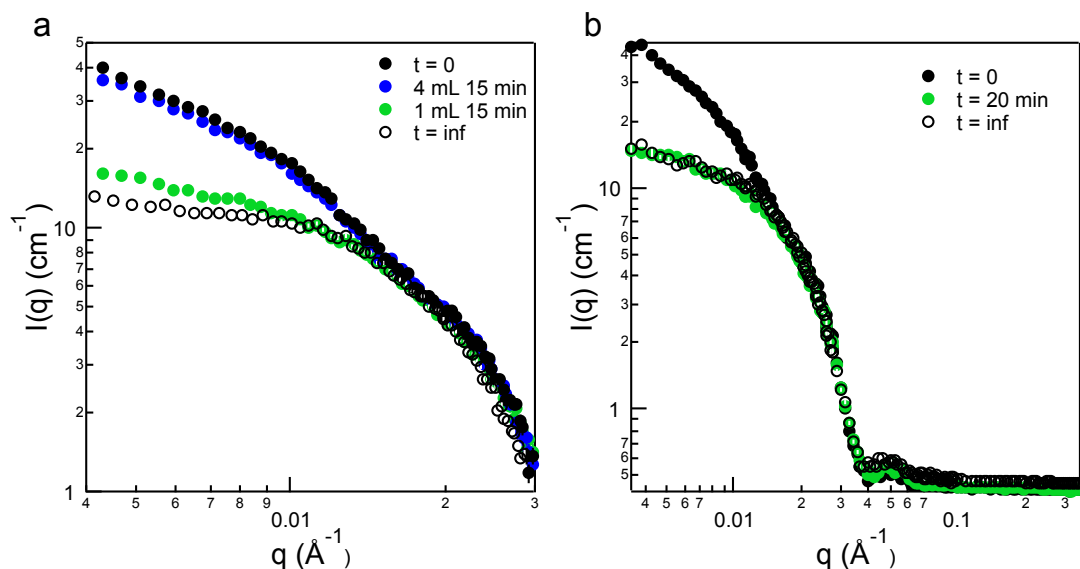


Figure 5.6. (a) Effect of air headspace on chain exchange due to rapid vortex mixing. Solution volumes of 1 mL and 4 mL were vortex mixed for 15 min in the same vial size. The solution with less possible air-water contact area per unit volume (4 mL solution) was significantly slower than the solution with more air headspace (1 mL solution). (b) The spherical form factor of PB cores did not change significantly as a result of rapid vortex mixing, further validating the use of Eq. 5.1 to quantify chain exchange.

To quantify chain exchange between micelles using SANS, the spherical form factor before and after vortex mixing was examined. SANS experiments conducted over a larger  $q$ -range ( $0.003$  to  $0.3 \text{\AA}^{-1}$ ) validated that the spherical form factor was consistent for solutions of post-mixed micelles at  $t = 0$  min (black circles) and after mixing for 20 min (green circles), as shown in Figure 5.6b. The unaltered form factor confirmed that the size and shape of the micelles were not changing significantly on average due to rapid vortex mixing. With this assumption supported, quantification of the fraction of chains exchanged between micelles was warranted using previously established methods.

### 5.3.1 Quantifying micelle chain exchange

A previously established method to determine the extent of chain exchange was utilized given the scattered intensity  $I(q,t)$  as a function of  $q$  at various mixing times (Section 2.2.4). Measuring the initial condition with maximum scattered intensity  $I(t=0)$  and the final condition with minimum scattered intensity  $I(t=\infty)$  enabled quantification of the fraction of chains exchanged between micelles,  $[1 - R(t_{mix})]$ , where  $R(t_{mix})$  is given as<sup>2</sup>

$$R(t_{mix}) = \left( \frac{I(t_{mix}) - I(\infty)}{I(0) - I(\infty)} \right)^{1/2} \quad (5.1)$$

Note that  $I(t_{mix})$  was determined by integrating  $I(q,t_{mix})$  from low to mid- $q$  range, in this case from 0.004 to 0.02  $\text{\AA}^{-1}$ . For the case of mixing micelles with  $h$ -cores and  $h/d$ -coronas, it was shown that  $R(t_{mix})$  is valid at sufficiently low  $q$  or large length scales.<sup>13</sup> At high  $q$ , local domains of either  $h$ - or  $d$ -chains can contribute to excess scattering.<sup>14</sup> Other major assumptions included kinetic zero-average contrast conditions and unchanging micelle form factors (Fig. 5.6b).

### 5.3.2 Concentration dependence

With an established method to quantify the fraction of chains exchanged as a function of time, it was important to understand the concentration dependence of the chain exchange mechanism. For example, an increasing rate of chain exchange with concentration may indicate a fusion/fission controlled process, whereas a lack of dependence on concentration would support a single chain exchange mechanism.

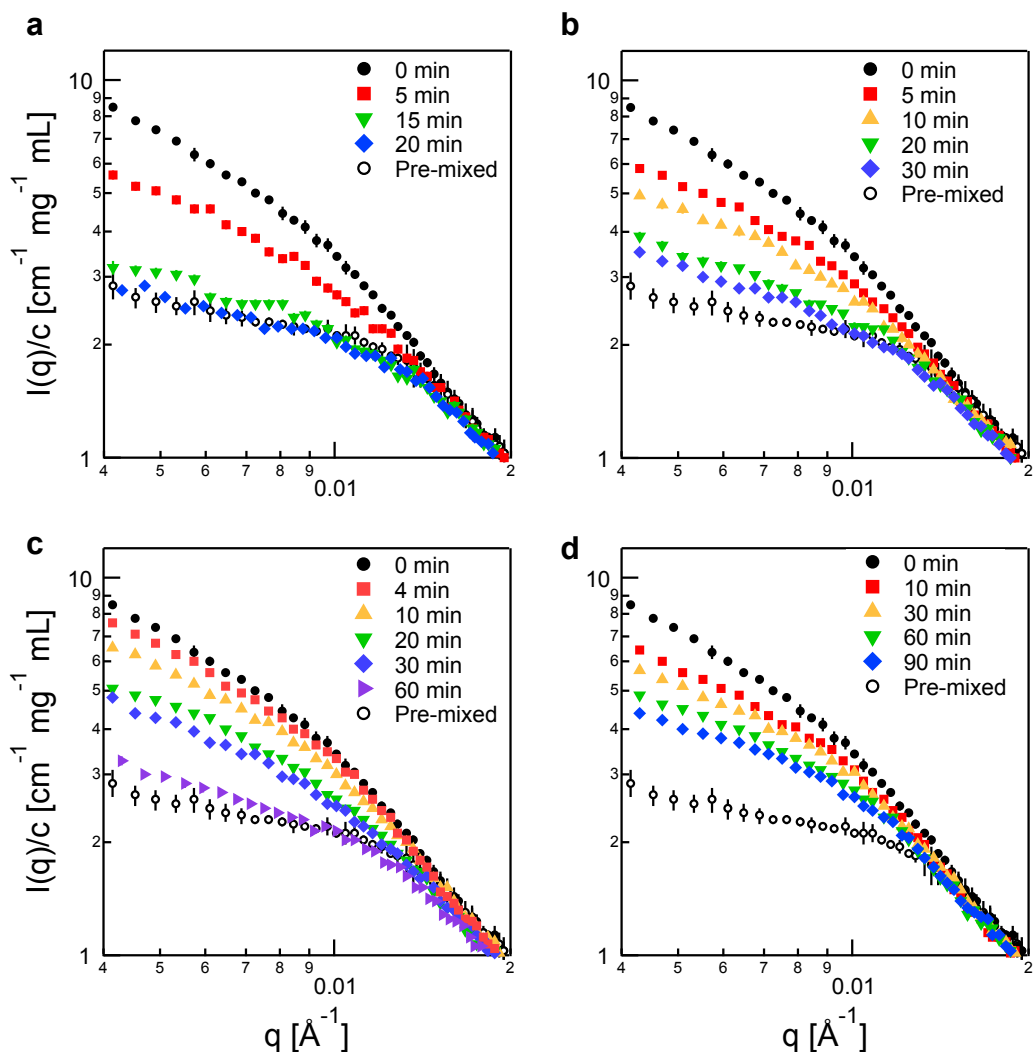


Figure 5.7. SANS concentration series to determine micelle chain exchange kinetics after rapid vortex mixing in solutions at (a)  $5.0 \text{ mg mL}^{-1}$ , (b)  $7.5 \text{ mg mL}^{-1}$ , (c)  $10.0 \text{ mg mL}^{-1}$ , and (d)  $15.0 \text{ mg mL}^{-1}$ . The 0 min sample and pre-mixed sample are averaged scattering intensities of three micelle concentrations. The error bars represent the standard deviation.

As before, separate PB-*h*PEO and PB-*d*PEO micelle solutions were mixed at varying polymer concentrations. The scattered intensity was collected as a function of vortex mixing time. Figure 5.7 showed that the general trend of decreasing intensity

as a function of mixing time was reproducible at various concentrations. Due to more chains contributing in the exchange process, samples with higher concentration required proportionally larger time between sampling (e.g. up to 60 min for  $10 \text{ mg mL}^{-1}$ ).

### 5.3.3 Surface-limited chain exchange kinetics

Applying the same assumptions and methods (Eq. 5.1) to determine the fraction of chains exchanged, the chain exchange kinetics could be quantified and plotted in the form of concentration of chains exchanged vs. mixing time. Figure 5.8a showed the fraction of chains exchanged  $[1 - R(t_{mix})]$  as a function of mix time. Figure 5.8b showed the same data converted to a concentration of mixed chains  $C_0[1 - R(t_{mix})]$ , in which  $C_0$  is the total constant polymer concentration. This expression assumes a zero-order rate expression with respect to polymer concentration.

The results shown in Figure 5.8 were significant in distinguishing the chain exchange mechanism. For single chain exchange, the assumed rate-limiting step is the expulsion of a core chain into water, where the chain diffuses through solution and reinserts into another micelle. Previous kinetic studies on single chain exchange between diblock copolymer micelles under quiescent conditions found an approximate logarithmic exchange rate.<sup>15,16</sup> With the exception of the  $15 \text{ mg mL}^{-1}$  sample, the chain exchange rate was highly linear with mixing time, which suggested chain exchange found here was not single chain exchange in bulk. The linear exchange kinetics with mix time strongly suggested the mechanism was surface-limited (zero-order), implying that the “limiting reagent” was the air-water interface. The zero-

order rate constant decreased within the range from  $0.24 \pm 0.01 \text{ mg mL}^{-1} \text{ min}^{-1}$  at lower concentrations to  $0.09 \pm 0.02 \text{ mg mL}^{-1} \text{ min}^{-1}$  at higher concentrations.

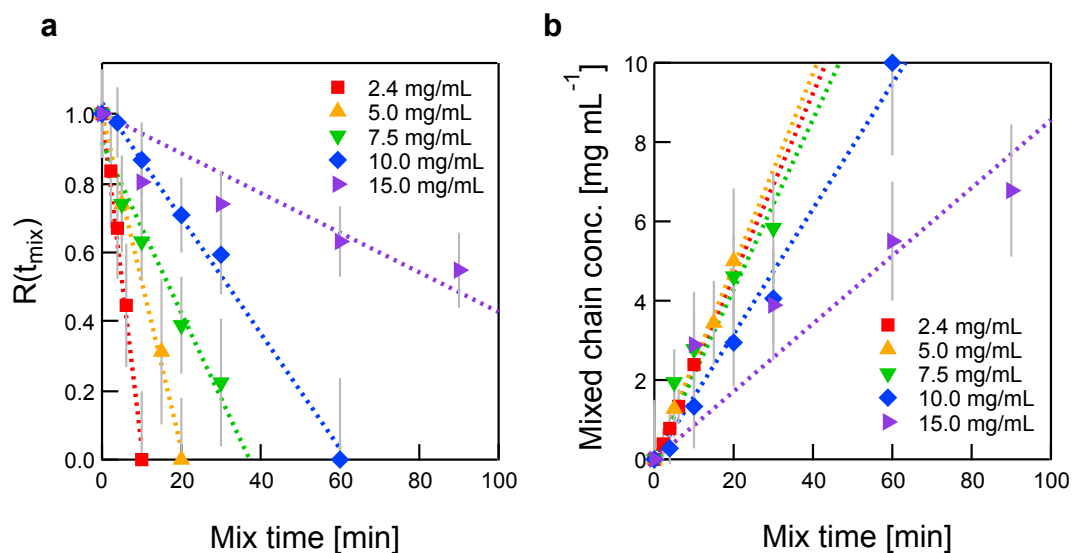


Figure 5.8. Quantification of micelle chain exchange kinetics. (a) The fraction of chains exchanged and (b) concentration of chains exchanged as a function of mix time. The linear kinetics suggested a surface-limited exchange process. Increasing concentration also led to a decrease in the apparent zero-order rate constants and deviations from linearity. The error bars for  $R(t_{\text{mix}})$  and mixed chain concentration were propagated based on the uncertainty in polymer concentration.

Surface-limited kinetics are reasonable based on two conditions: (1) chain exchange was effectively frozen in the bulk solution, and (2) surfactants spontaneously tend toward interfaces to lower the surface energy. The apparent decrease in the exchange rate constant (decreasing slope in Fig. 5.8b) with increasing polymer concentration was less discernible. One possible explanation for the

decreasing rate could be the slight increase in solution viscosity upon addition of polymer. Presumably, a higher viscosity could reduce the air-water surface turnover rate for a given rate of agitation (~3200 rpm). The decrease in exchange rate was most pronounced for the 15 mg mL<sup>-1</sup> sample, which also appeared to deviate from linearity. This deviation could occur as the solution concentration approaches the corona overlap concentration, in which micelle coronas begin to overlap and interparticle interactions become significant. Interestingly, a similar trend in hindered single chain exchange kinetics was found for much higher polymer concentrations (15 vol% PS-PEP in squalane)<sup>17</sup> compared to dilute solutions (0.5-2 vol% PS-PEP in squalane).<sup>18</sup> The slower single chain exchange at higher polymer concentrations was subsequently rationalized by Halperin to originate from coronal screening and an increase in osmotic pressure.<sup>19</sup>

To explore the effect of viscosity or coronal screening effects on the exchange mechanism, further kinetic experiments are required in the semi-dilute and concentrated regimes to distinguish the full dependence on concentration and bulk solution properties. Despite the speculation for the concentration-dependent rate constant, the method to quantify chain exchange proved useful in suggesting a surface-limited kinetic process from rapid vortex mixing. Although the employed mixing method decreased the process timescale considerably, rapid vortex mixing resulted in poorly defined flow. As a consequence, important factors such as the shear viscosity, shear rate, air-water surface area, and surface turnover rate remained difficult to determine. However, the vortex mixing stands as a simple handle to control the timescale for chain exchange of block polymer micelles in aqueous solutions. A more controlled approach for generating a hydrophobic interface would help explain the

surface-limited process, such as using concentric rotating cylinders with hydrophobic-coated surfaces or adding hydrophobic beads with defined surface areas. Furthermore, examining the effect of a solid-liquid interface compared to a gas-liquid or liquid-liquid interface would distinguish the importance of fluidity and rupturing of the interface.

#### **5.4 Relevance to Other Amphiphilic Systems and Applications**

Solution agitation, fluid air-water interfaces, and surface-induced aggregation have been the focus of several pharmaceutical and protein stability studies over the past two decades. In several examples, the fluid nature of the air-water interface and high shear rates near the interface are argued to play a crucial role in unfolding and aggregating proteins.<sup>8,9,20</sup> For example, studies on the aggregation kinetics of solutions containing therapeutic proteins were found to correlate with the rupturing and regeneration of the air-water interface.<sup>21,22</sup> The elimination of hydrophobic surfaces and the addition of surfactants have been found to improve protein solution stability by limiting undesirable aggregation.<sup>8</sup> Meanwhile, the stress at solid-liquid interfaces (e.g. glass vial wall, stainless steel wall, Teflon stir bar) can also significantly affect protein stability and aggregation. For example, the aggregation of a particular monoclonal antibody (mAb) was found to have a second-order dependence on stainless steel surface area and zero-order dependence on mAb concentration.<sup>23</sup> Other work that examined the aggregation and breakage kinetics of small molecule assemblies also demonstrated a strong dependence on the type of solution agitation.<sup>24</sup>

The stability and aggregation of solution assemblies are fundamentally linked for stabilized colloidal suspensions, such as intricately folded proteins, small molecule

assemblies, or block polymer micelles. Although each subset is often studied as a distinct entity, there can be significant knowledge shared between these systems. Highly amphiphilic block polymer assemblies have been shown to provide greater kinetic stability owing to slow chain exchange. However, this work demonstrated that polymeric micelles are not necessarily kinetically-trapped under conditions of sufficient perturbation. This knowledge will be important in the formulation and processing of block polymer assemblies for various applications. Understanding the interfacial and flow effects on micelle stability could provide useful design criteria, for example, that lead to improved blood circulation by limiting protein adsorption and aggregation when exposed to hydrophobic domains.

## **5.5 Chapter Summary**

Previous chapters demonstrated that the micelle chain exchange process in aqueous solutions was dependent on solution agitation (Ch. 3), and the timescale for exchange process can be significantly reduced through rapid mixing methods (Ch. 4). SANS methods were employed to quantify chain exchange using SANS, further demonstrating that micelle chain exchange processes in aqueous solutions are highly dependent on the mixing method. Discrepancies in micelle growth from controlled flows generated with a cone-plate or concentric cylinder geometry were indicative that the presence of an air-water interface was critical for fast chain exchange. A common laboratory method for solution agitation, rapid vortex mixing, generated high volume average shear rates and high air-water surface turnover rates. The resulting chain exchange kinetics was linear with mix time, suggesting a surface-limited exchange process. As expected, reducing the air volume within a vial led to significantly slower exchange rates. Interestingly, the rate of chain exchange decreased with increasing

polymer concentration. It was speculated that an increase in viscosity, decrease in surface turnover rate, or the onset of interparticle interactions could account for decreased rate of exchange.

Interfacial and shear effects have been studied throughout a various self-assembled systems, including proteins, peptides, small molecule, and polymeric solutions. SANS techniques provide unique insight into the structure and dynamics of solution assemblies, given that available deuterated/hydrogenated analogs are commercially available or synthetically feasible. This work expands on these general approaches to study kinetics of micelle chain exchange in aqueous solutions as a consequence of mixing. In the future, the same methods and principles can be applied to investigate the role of other important system parameters under flow, such as molecular weight, temperature, and tunable interfacial modifications, which could provide useful engineering insight when formulating and processing block polymer micelles for various applications.

## REFERENCES

- 1 Won, Y. Y., Davis, H. T. & Bates, F. S. Molecular exchange in PEO-PB micelles in water. *Macromolecules* **36**, 953-955 (2003).
- 2 Lund, R., Willner, L., Richter, D. & Dormidontova, E. E. Equilibrium chain exchange kinetics of diblock copolymer micelles: Tuning and logarithmic relaxation. *Macromolecules* **39**, 4566-4575 (2006).
- 3 Stellbrink, J., Lonetti, B., Rother, G., Willner, L. & Richter, D. Shear induced structures of soft colloids: Rheo-SANS experiments on kinetically frozen PEP-PEO diblock copolymer micelles. *Journal of Physics-Condensed Matter* **20** (2008).
- 4 Wang, C.-W., Sinton, D. & Moffitt, M. G. Flow-Directed Block Copolymer Micelle Morphologies via Microfluidic Self-Assembly. *Journal of the American Chemical Society* **133**, 18853-18864 (2011).
- 5 Wang, C.-W., Sinton, D. & Moffitt, M. G. Morphological Control via Chemical and Shear Forces in Block Copolymer Self-Assembly in the Lab-on-Chip. *ACS Nano* **7**, 1424-1436 (2013).
- 6 Leal-Calderon, F., Schmitt, V. & Bibette, J. *Emulsion science: basic principles*. (Springer, 2007).
- 7 Schuster, D. *Encyclopedia of Emulsion Technology: Basic theory, measurement, applications*. Vol. 3 (CRC Press, 1987).
- 8 Thomas, C. R. & Geer, D. Effects of shear on proteins in solution. *Biotechnology Letters* **33**, 443-456 (2011).
- 9 Bai, G., Bee, J. S., Biddlecombe, J. G., Chen, Q. & Leach, W. T. Computational fluid dynamics (CFD) insights into agitation stress methods in biopharmaceutical development. *International Journal of Pharmaceutics* **423**, 264-280 (2012).
- 10 Kiese, S., Pappenberg, A., Friess, W. & Mahler, H.-C. Shaken, not stirred: Mechanical stress testing of an IgG1 antibody. *Journal of Pharmaceutical Sciences* **97**, 4347-4366 (2008).

- 11 Nielsen, L. *et al.* Effect of environmental factors on the kinetics of insulin fibril formation: Elucidation of the molecular mechanism. *Biochemistry* **40**, 6036-6046 (2001).
- 12 Roberts, C. J. *Nucleation, Aggregation, and Conformational Distortion*. 125-149 (John Wiley & Sons, Inc., 2014).
- 13 Zinn, T., Willner, L., Lund, R., Pipich, V. & Richter, D. Equilibrium exchange kinetics in n-alkyl-PEO polymeric micelles: single exponential relaxation and chain length dependence. *Soft Matter* **8**, 623-626 (2012).
- 14 Lund, R., Willner, L. & Richter, D. Kinetics of Block Copolymer Micelles Studied by Small-Angle Scattering Methods. *Advances in Polymer Science* **259**, 51-158 (2013).
- 15 Lund, R., Willner, L., Stellbrink, J., Lindner, P. & Richter, D. Logarithmic chain-exchange kinetics of diblock copolymer micelles. *Physical Review Letters* **96**, 068302 (2006).
- 16 Choi, S. H., Lodge, T. P. & Bates, F. S. Mechanism of molecular exchange in diblock copolymer micelles: hypersensitivity to core chain length. *Physical Review Letters* **104**, 047802 (2010).
- 17 Choi, S. H., Bates, F. S. & Lodge, T. P. Molecular Exchange in Ordered Diblock Copolymer Micelles. *Macromolecules* **44**, 3594-3604 (2011).
- 18 Lund, R. *et al.* Unraveling the equilibrium chain exchange kinetics of polymeric micelles using small-angle neutron scattering - architectural and topological effects. *Journal of Applied Crystallography* **40**, S327-S331 (2007).
- 19 Halperin, A. On Micellar Exchange: The Role of the Insertion Penalty. *Macromolecules* **44**, 5072-5074 (2011).
- 20 Sluzky, V., Tamada, J. A., Klibanov, A. M. & Langer, R. Kinetics of insulin aggregation in aqueous solutions upon agitation in the presence of hydrophobic surfaces. *Proceedings of the National Academy of Sciences* **88**, 9377-9381 (1991).
- 21 Rudiuk, S., Cohen-Tannoudji, L., Huille, S. & Tribet, C. Importance of the dynamics of adsorption and of a transient interfacial stress on the formation of aggregates of IgG antibodies. *Soft Matter* **8**, 2651-2661 (2012).

- 22 Bee, J. S. *et al.* Production of particles of therapeutic proteins at the air-water interface during compression/dilation cycles. *Soft Matter* **8**, 10329-10335 (2012).
- 23 Bee, J. S., Davis, M., Freund, E., Carpenter, J. F. & Randolph, T. W. Aggregation of a monoclonal antibody induced by adsorption to stainless steel. *Biotechnology and Bioengineering* **105**, 121-129 (2010).
- 24 Carnall, J. M. A. *et al.* Mechanosensitive Self-Replication Driven by Self-Organization. *Science* **327**, 1502-1506 (2010).

## Chapter 6

### CONCLUSIONS AND FUTURE RECOMMENDATIONS

#### 6.1 Thesis Summary

Controlling chain exchange of block polymer micelles in aqueous solutions is important in the development of emerging applications that hinge on the stability of block polymer solution assemblies. Understanding kinetic pathways that affect solution assemblies is critical to tailor materials for desired applications and to establish novel capabilities and features. This thesis expands the use of complementary solution characterization methods to explore the size evolution of block polymer micelles in aqueous solutions. DLS, Cryo-TEM, and SANS methods probed the structure and exchange kinetics of poly(butadiene-*b*-ethylene oxide) (PB-PEO) diblock copolymer micelles, specifically focusing on processing effects such as cosolvent addition and removal (Ch. 3), molecular weight and temperature (Ch. 4), and shear and interfacial effects (Ch. 5). Detailed particle characterization under various solution conditions offered new insights into block polymer micelle self-assembly and dynamics in aqueous solutions.

Chapter 2 discussed polymer properties and solution preparation methods, which are known to critically influence the self-assembled structure and dynamics of block polymer assemblies. Furthermore, the use of complementary solution characterization methods (DLS, cryo-TEM, and SANS) established a balance between accessibility and structural insight.

Chapter 3 revealed an unexpected size evolution of PB-PEO micelles in aqueous solutions upon perturbation using THF/water cosolvent mixtures. Spherical PB-PEO micelles grew in size through a bimodal distribution, which depended on the polymer concentration and solution agitation. These findings highlighted the considerable influence of cosolvent preparation methods on the stability of macromolecular assemblies and demonstrated the kinetic constraints in block polymer micelles containing highly hydrophobic cores. Furthermore, these findings suggested the growth processes was likely a shear and/or interfacial fusion-controlled process, prompting further investigation into critical parameters underlying the chain exchange process. The relationship between processing conditions and chain exchange dynamics has critical implications on the stability of macromolecular-based nanocarriers.

Chapter 4 explored the dependence of molecular weight and temperature on the micelle growth process. In general, changing temperature and the molecular weight of the core and corona block led to different relaxation timescales and steady-state sizes following the addition and subsequent removal of THF cosolvent. Specifically, higher molecular weight polymers generally assembled into larger micelles upon direct dissolution of PB-PEO in water, eventually decreasing in size presumably through a fusion/fission mechanism. Higher molecular weight polymers exhibited larger characteristic timescales for micelle growth and relaxation after sufficient perturbation (40 wt% THF pre-dialysis). A similar bimodal size distribution was observed for all three molecular weight species, albeit with different initial and steady state micelle sizes. Solution temperature considerably affected the timescale for micelle growth and breakage of agitated micelle solutions. In particular, higher

temperatures (40-60 °C) resulted in faster breakage of large micelles directly dispersed in water (0 wt% THF) and slower growth of smaller micelles (40 wt% THF). Higher temperatures also led to morphological transitions and precipitation, presumably due to cross-linking or degradation of the PB cores.

Chapter 5 investigated the effects of shear and air-water interface on micelle size evolution in aqueous solutions. Previously established methods to quantify block polymer micelle chain exchange using SANS were applied to reveal the dependence of chain exchange processes in aqueous solutions on the agitation method. The different outcomes obtained from controlled flows generated with a cone-plate or concentric-cylinder geometry indicated that sufficient air-water interface in addition to high shear rates were critical for fast chain exchange (minutes). Comparably fast exchange kinetics was quantified over minute timescales using rapid vortex mixing. Importantly, the rate of chain exchange was linear with mix time, suggesting a surface-limited aggregation process. The exchange rate constant decreased with increasing polymer concentration, suggesting that changes in viscosity or interparticle interactions could affect the interfacial chain exchange mechanism.

Overall, this work developed new insights in amphiphilic block polymer chain exchange processes by demonstrating that micelles could evolve and relax in highly selective solvents given sufficient perturbation and agitation. These results may find broader relevance in understanding the stability and aggregation kinetics of other amphiphilic systems, such as proteins, peptides, and other nanoparticle solutions, which have exhibited comparable dependence on solution processing conditions.

## 6.2 Future Recommendations

A robust method is needed to quantify micelle populations to establish reliable growth rate expressions and to better understand the fundamentals of micelle size evolution in aqueous solutions. This task is not easy considering the nanometer size scale and relatively small differences between primary particles and aggregates. SANS provides one route to fit a number distribution, owing to the good spatial resolution and statistics. Additionally, given that the characteristic relaxation times can be decreased from weeks to minutes by using vigorous mixing methods, a neutron experiment could be accomplished within a reasonable timeframe using the same sample. However, neutron scattering is fairly inaccessible and expensive; therefore, an alternative method would be advantageous. Analytical separation techniques such as analytical centrifugation or size exclusion chromatography may provide a means to first separate particles and then quantify relative size distributions. These proposed methods would require sufficient sedimentation coefficients or column-packing parameters for good separation, and it would require operating under the assumption that the separation does not skew or disrupt the micelle distribution.

The properties of the core block are important in chain exchange dynamics, yet the core block behavior is not entirely understood. Similar perturbation and relaxation experiments accomplished through a cosolvent switch could be repeated with an analogous block polymer containing a low  $T_g$  core block (e.g. PEE or PEP), crystalline block (e.g. PCL), or glassy block (e.g. PS). In this manner, a more universal behavior could be evaluated based on the core block behavior, such as entanglement, interfacial tension, crystallinity, and glassy effects. In particular, PEE-PEO would be an easy route for matching  $N_{\text{core}}$  and  $N_{\text{corona}}$  of the current PB-PEO polymers, as it can be synthesized by catalytic hydrogenation of PB-PEO.<sup>1</sup> Unlike PB, PEE and PEP are

also not susceptible to cross-linking and degradation (Ch. 4) from higher temperatures and aeration due to agitation. Furthermore, the molecular weight range examined was relatively small for the PB core and PEO corona block. While the characteristic relaxation times and size scales were shown to be sensitive to these small changes in molecular weight, studies of relaxation kinetics obtained over a broader range are necessary to develop correlations or scaling relationships for describing more universal behavior.

Solution agitation in the presence of a hydrophobic interface was a key driving force for chain exchange in frozen block polymer solution assemblies. One route toward establishing a more controlled flow with a hydrophobic interface could be to use rotating concentric cylinders that are coated or made of some hydrophobic material. Another method could incorporate solid beads in micelle solutions to control interfacial area, surface chemistry, and adsorption properties. It may be that the fluidity and rupturing of the hydrophobic interface is essential for micelle chain exchange and growth in an aqueous environment. In this case, the effect of flow at an air-water interface could be better characterized with an interfacial rheometer. Furthermore, a surface rupturing mechanism such as rotating rod or rolling device<sup>2</sup> could be used to relate exchange kinetics to the number of rupture events and the exposed surface area.

There are several avenues to build upon this work for the application of block polymer micelles as drug delivery vehicles. Loading hydrophobic drug or dye molecules into micelles is known to affect self-assembly and dynamics,<sup>3</sup> but the entire process remains poorly understood. Equally, the effect of chain exchange processes on drug loading and release kinetics are also poorly defined.

Compounded by the complexity of additional components, the effect of shear and interfacial effects have not been directly explored in the context of micelle drug release characteristics and serum stability. Currently, there is a discontinuity in the understanding of fundamental polymer self-assembly and the countless complexities expressed in biological environments. One recommendation is to develop a more biologically relevant yet high throughput metric for quantifying drug loading and release kinetics. Currently, methods to explore serum stability or drug release are either high-throughput or biologically relevant. For example, dialysis methods that quantify drug release can be conclusive and high-throughput, but are not in the least biologically relevant. Meanwhile, *in vivo* models can generate biologically relevant but not high-throughput assessment.

New high-throughput, more biologically relevant, experimental methods are necessary to better screen for desirable drug delivery characteristics, such as micelle stability, drug retention, and controlled release. One concept entails tailorable microfluidic-mixing devices that better quantify micelles stability under biomimetic, vascular-like environments. Key variables could be controlled, such as temperature, viscosity, pH, flow rate, residence time, channel diameter, channel surface chemistry, micelle concentration, and serum protein concentration. In particular, serum proteins or specific surface chemistries may act as hydrophobic domains for micelle adsorption and aggregation. Flow devices could be hierarchically modified to serve as a more realistic, convenient, and high-throughput environment for investigating serum stability, circulation time, and drug release kinetics. Undoubtedly, this metric would fail to capture all of the biological complexities of an *in vivo* model. However, it would serve as a platform toward improved experimental screening methods to

identify characteristics that affect drug release and micelle serum stability under imposed shear flow.

Several routes are possible for the continuation of this work.

Recommendations center upon fundamental questions regarding solution assembly of block polymers, methods to better quantify micelle number distributions, and other methods to control flow and interfacial properties. Application-driven possibilities also exist for improving methods to investigate block polymer micelles for use as drug delivery vehicles. Discoveries along these routes could provide fundamental insights into block polymer chain exchange in aqueous solutions and improve the efficacy of polymeric drug delivery vehicles.

## REFERENCES

- 1 Hillmyer, M. A. & Bates, F. S. Synthesis and characterization of model polyalkane-poly(ethylene oxide) block copolymers. *Macromolecules* **29**, 6994-7002 (1996).
- 2 Rudiuk, S., Cohen-Tannoudji, L., Huille, S. & Tribet, C. Importance of the dynamics of adsorption and of a transient interfacial stress on the formation of aggregates of IgG antibodies. *Soft Matter* **8**, 2651-2661 (2012).
- 3 Schulz, A. *et al.* Drug-Induced Morphology Switch in Drug Delivery Systems Based on Poly(2-oxazoline)s. *ACS Nano* **8**, 2686-2696 (2014).

**Appendix A**  
**SUPPLEMENTARY DATA**

PB- <i>h</i> P EO, B <sub>59</sub> O <sub>180</sub>		PB- <i>d</i> P EO, B <sub>59</sub> <i>d</i> O <sub>163</sub>	
Concentration [mg mL <sup>-1</sup> ]	Absorbance at 259 nm [a.u.]	Concentration [mg mL <sup>-1</sup> ]	Absorbance at 259 nm [a.u.]
4.82	0.1748	10.08	0.2803
2.44	0.0962	5.04	0.1593
1.15	0.0467	2.52	0.0863
0.63	0.0260	1.25	0.0447
0.32	0.0134	0.64	0.0243
0.16	0.0067	0.00	0.0020

Figure A.1. Polymer concentration and UV-Vis absorbance data for B<sub>59</sub>O<sub>180</sub> in H<sub>2</sub>O (left) and 88 wt% B<sub>59</sub>*d*O<sub>163</sub> / 12 wt% B<sub>59</sub>O<sub>180</sub> in D<sub>2</sub>O (right) used in the calibration curves shown in Figure 2.2.

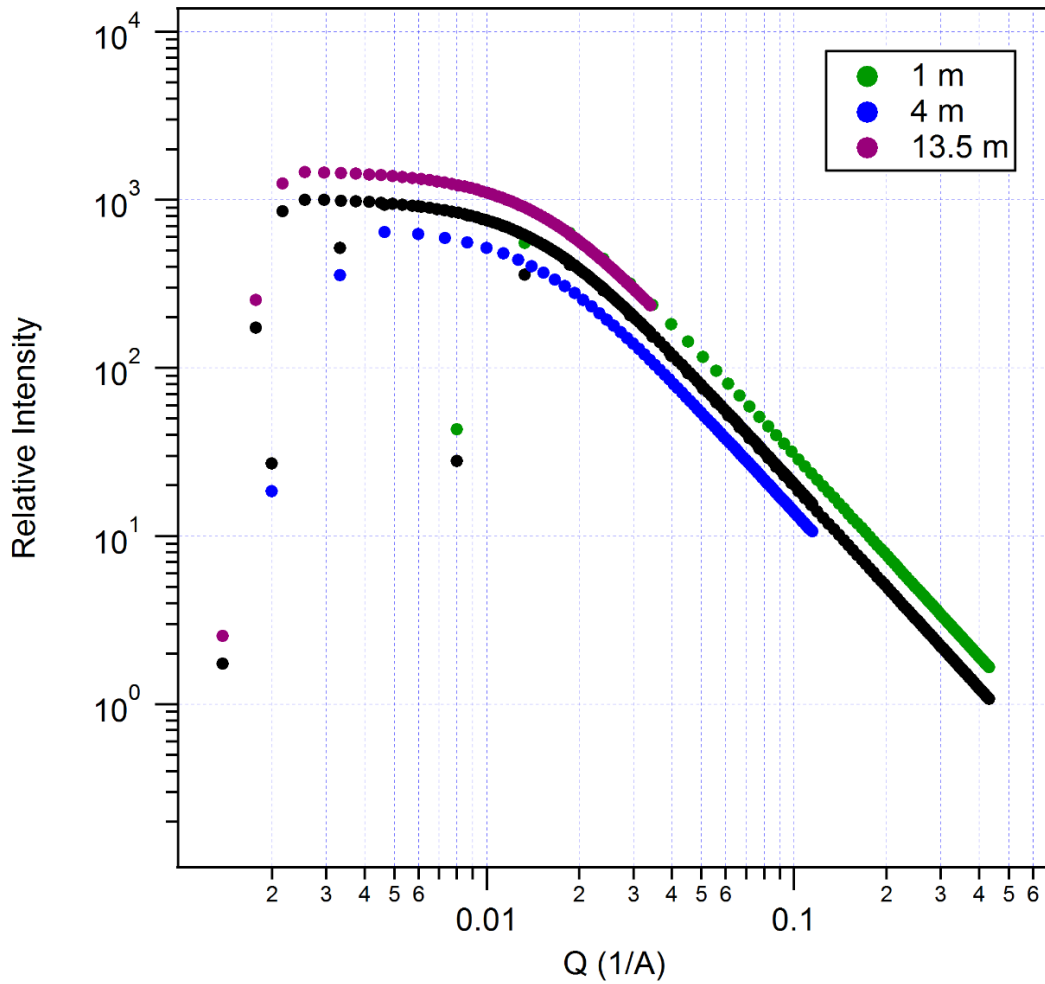


Figure A.2. Q-ranges for SANS sample-to-detector distances at 1 m (green), 4 m (blue), and 13.5 m (violet) produced using SASCALC package in Igor Pro. Neutron wavelength was 6  $\text{\AA}$ . Scattered intensity for the three overlaid curves (black) show good overlap throughout  $\sim 0.003 \text{ \AA}^{-1}$  to  $\sim 0.4 \text{ \AA}^{-1}$

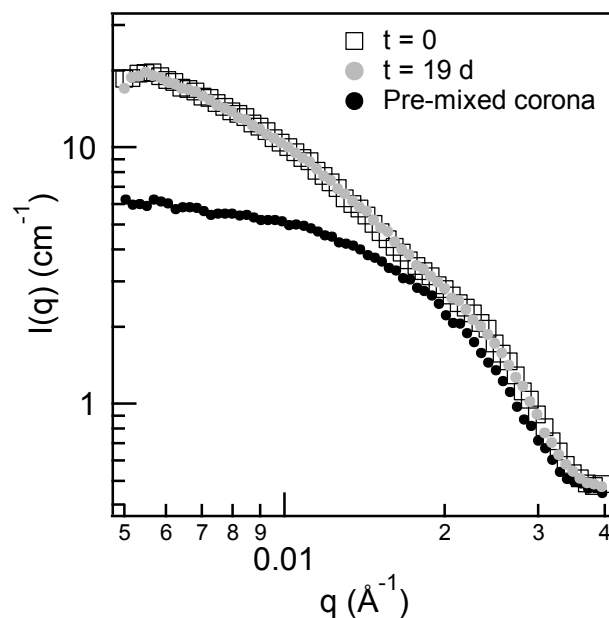


Figure A.3. SANS data showing negligible chain exchange in  $\text{H}_2\text{O}/\text{D}_2\text{O}$  under quiescent conditions. Negligible chain exchange occurred between PB-*h*PEO and PB-*d*PEO micelles up to 19 d (gray circles), as demonstrated by the overlap with the scattering curve immediately after combining equal solution volumes of pure PB-*h*PEO micelles and pure PB-*d*PEO micelles (open squares). The scattering curve for micelles containing randomly mixed PB-*h*PEO and PB-*d*PEO chains is shown for comparison (black circles).

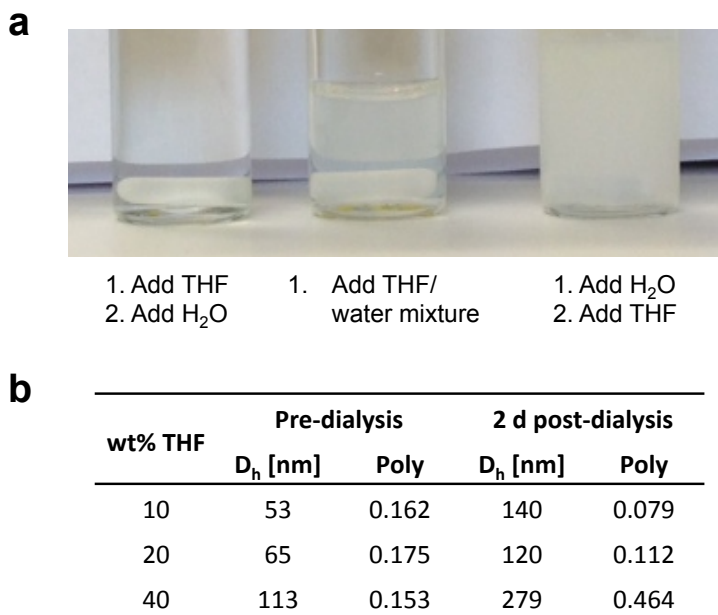


Figure A.4. (a) Image of PS-PEO solutions [ $M_n$  PS = 12.5 kg mol<sup>-1</sup>,  $M_n$  PEO = 35.6 kg mol<sup>-1</sup> PEO, 74 wt% PEO,  $\bar{D} = 1.08$ ] prepared in water/THF mixtures (10 wt% THF, 5 mg mL<sup>-1</sup>). The order in which the solvent was added to the dry polymer made a significant difference in the resulting solution assembly. Adding THF solvent first and then adding water (or adding the THF/water mixture together to the dry polymer) produced a clear micelle solution. Meanwhile, adding water first and then adding THF produced a cloudy solution. (b) DLS data for PS-PEO solutions prepared at various THF compositions (adding THF first and then adding water) prior to dialysis. Solutions were dialyzed into pure water for 24 h to remove THF cosolvent and then were measured using DLS after magnetic stirring at 200 rpm. Hydrodynamic diameters  $D_h$  and polydispersity parameters *Poly* were fit using the quadratic cumulant method. For each solution, a significant increase in  $D_h$  was found 2 d post-dialysis. All data was collected by Connor Hodges.

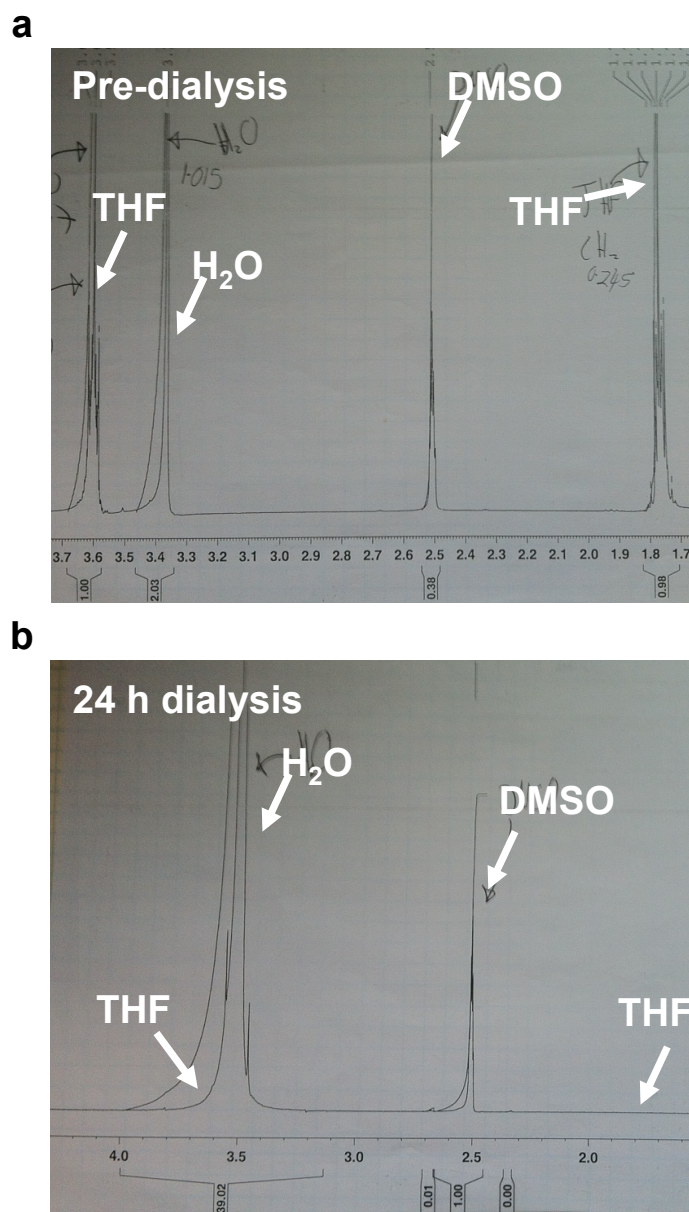


Figure A.5.  $^1\text{H}$  NMR data of PB-PEO micelle solutions in THF/water mixtures (a) prior to dialysis and (b) after 24 h dialysis to pure water. The disappearance of THF solvent peaks at  $\sim 3.6$  ppm and  $\sim 1.75$  ppm confirmed removal of THF cosolvent (60 wt% THF) after 24 h of dialysis to water. Samples of solutions were in deuterated DMSO for  $^1\text{H}$  NMR analysis. Data were collected and analyzed by Dr. Tom Smart.

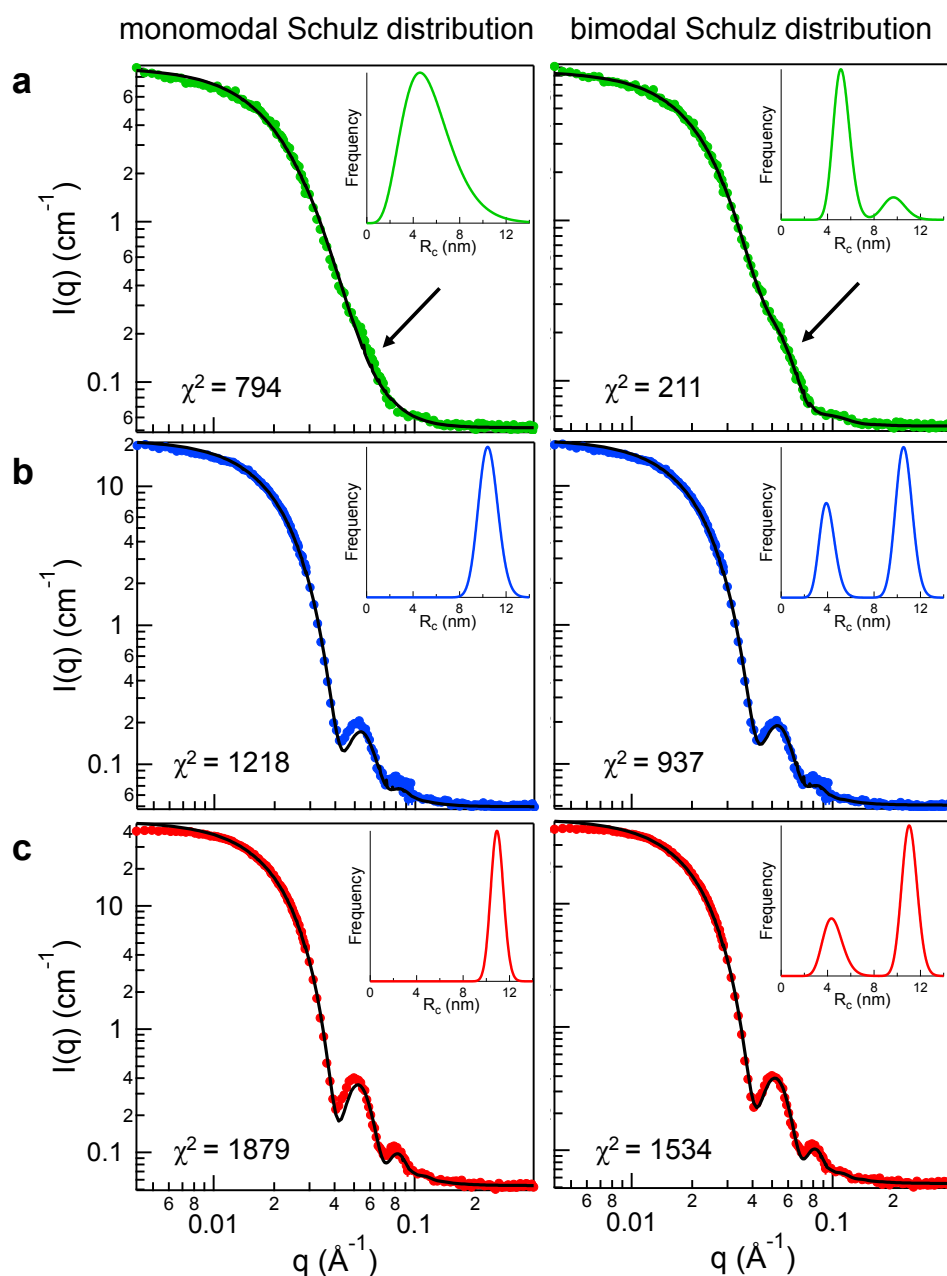


Figure A.6. Comparing the SANS data fits using monomodal (left column) and bimodal (right column) Schulz spheres at initial polymer concentrations of (a)  $2 \text{ mg mL}^{-1}$ , (b)  $5 \text{ mg mL}^{-1}$ , and (c)  $10 \text{ mg mL}^{-1}$  (see Figure 3.8). The bimodal core radii distribution consistently provided a better fit (black lines) to the experimental data (points). Insets show the number distribution of core radii. Figure reproduced with permission from *Nature Communications*, 5, 3599 (2014).

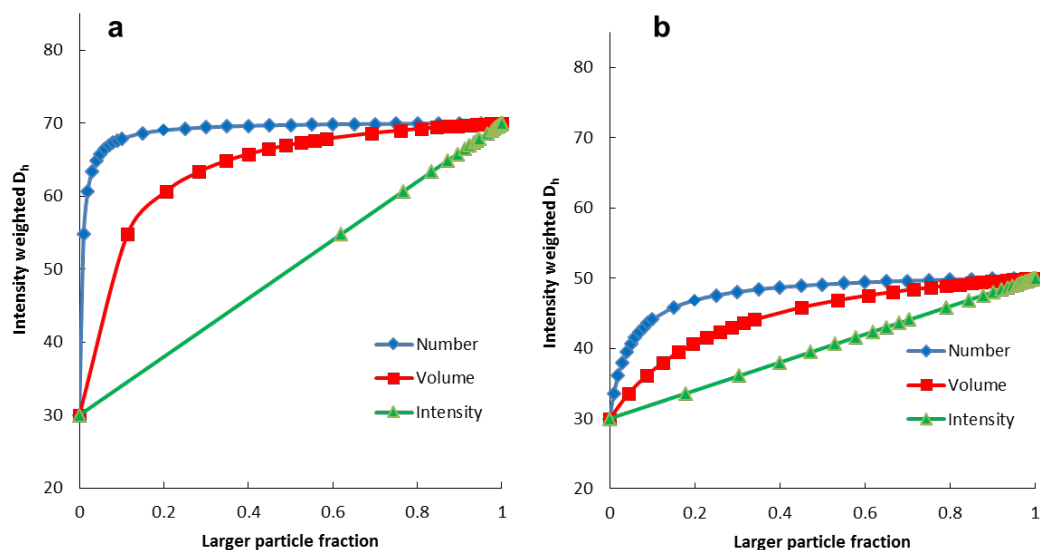


Figure A.7. Estimated intensity-weighted hydrodynamic diameters  $D_h$  for a bimodal mixture of spherical particles with diameters of (a) 30 nm and 70 nm, or (b) 30 nm and 50 nm. The x-axis represents the fraction of larger particles based on (blue) number fraction, (red) volume fraction, and (green) intensity fraction. The significant increase in the intensity-weighted  $D_h$  is demonstrated with only a relatively small increase in number fraction of larger particles ( $< 0.1$ ).

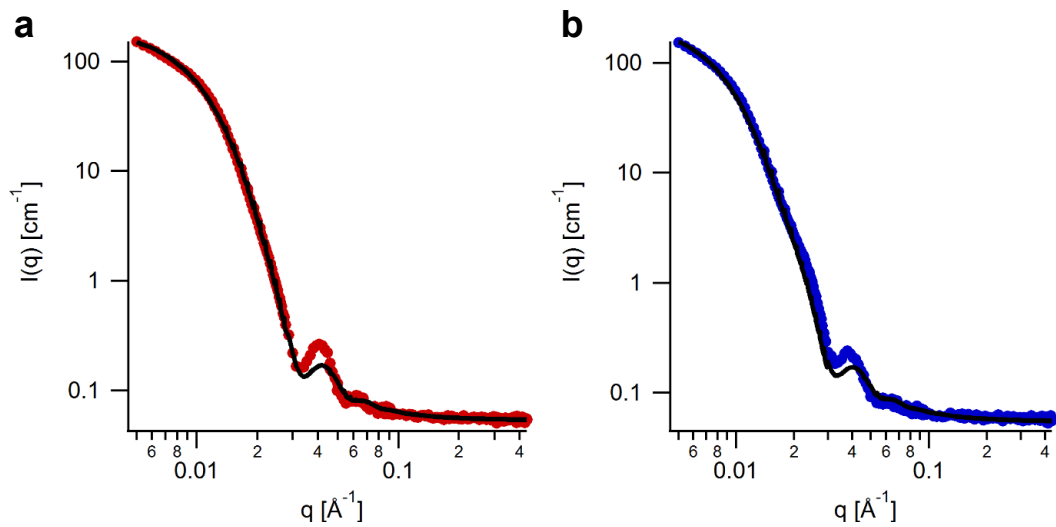


Figure A.8. SANS data (points) and fits (black lines) for PB-PEO micelles in  $\text{D}_2\text{O}$ . (a) The core-shell sphere fit to  $\text{B}_{81}\text{O}_{182}$  micelles gave  $R_c \sim 14$  and  $R_m \sim 35$ . (b) The core-shell sphere fit to  $\text{B}_{81}\text{O}_{257}$  micelles gave  $R_c \sim 15$  and  $R_m \sim 41$ .

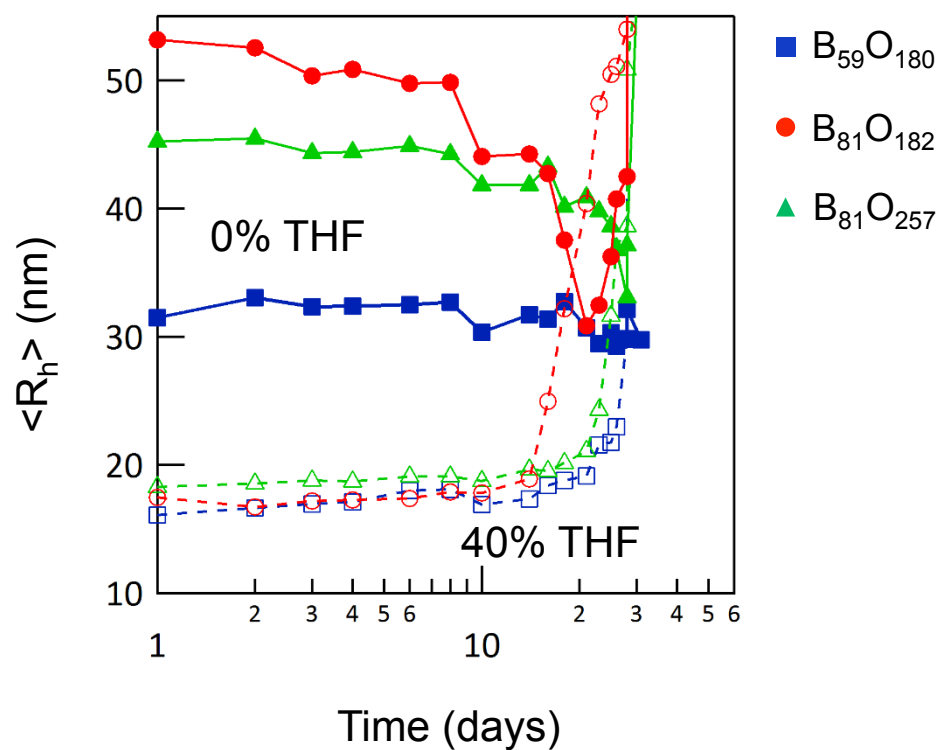


Figure A.9. Size evolution of PB-PEO micelles that were stirred at 40 °C after dialysis into water. Open symbols represent 40 wt% THF prior to dialysis. Closed symbols represent 0 wt% THF prior to dialysis. DLS on solutions containing  $B_{59}O_{180}$  (blue squares),  $B_{81}O_{182}$  (red circles), or  $B_{81}O_{257}$  (green triangles) demonstrated fairly consistent trends in micelle size relaxation in water (refer to Figure 4.3).

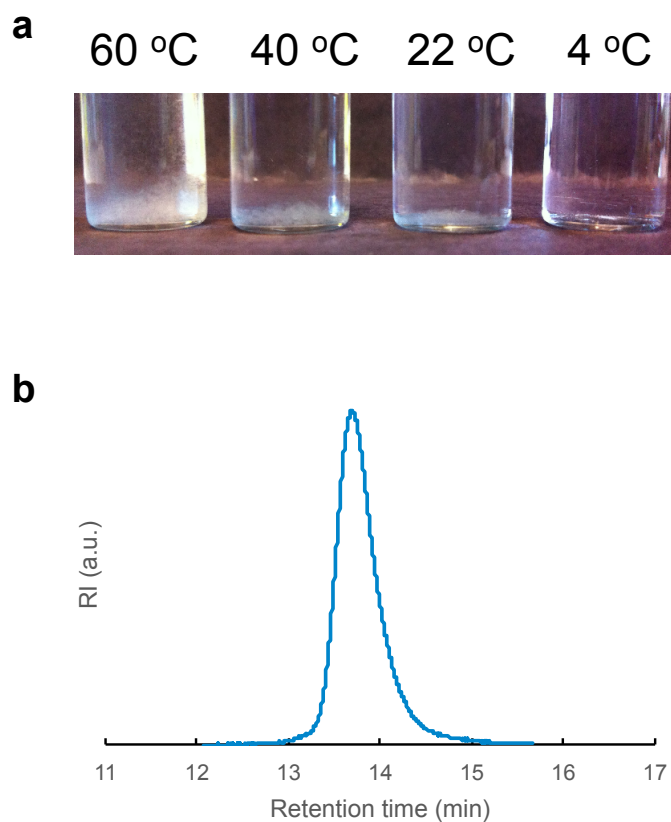


Figure A.10. (a) Images of  $B_{81}O_{182}$  polymer redissolved in THF after stirring at 60 °C, 40 °C, 22 °C, and 4 °C (40 wt% THF and 10 mg mL<sup>-1</sup> prior to dialysis into water). After the polymer precipitated in water at the specified temperature (see Figure 4.3), the visible precipitates in both water and THF suggested the PB had cross-linked or degraded to varying degrees at temperatures between 22-60 °C. (b) SEC of the  $B_{81}O_{182}$  redissolved in THF did not show cross-linking after agitation at 4 °C.

## **Appendix B**

### **ARTIFACTS IN CRYO-TEM**

Particle characterizations through cryo-TEM methods provide a more representative size and structure of solution assemblies compared to dry-state TEM methods. However, the sample preparation process and the incident electron beam commonly present artifacts within vitrified specimens for cryo-TEM analysis. Note that all images presented here were captured from samples prepared using the same blotting and vitrifying conditions, demonstrating the wide variability in artifacts produced from cryo-TEM techniques. The artifacts encountered during sample preparation and imaging of block polymer micelles are classified and discussed below. The main categories of artifacts include (B.1) ice thickness and size gradients, (B.2) particle packing and alignment, (B.3) sample contamination, (B.4) sample and background degradation, and (B.5) blotting effects.

#### **B.1 Ice Thickness and Size Gradients**

Figure B.1 demonstrates a biased particle size distribution as a result of differences in ice thickness (hyperquenched, amorphous water-ice). In general, larger particles tend to accumulate near the grid edge where the ice is thicker, while smaller particles tend to accumulate toward the grid center where the ice is thinner. The full size distribution both near the grid edge and toward the grid center can be better captured at lower magnification (Fig. B.1 left), although smaller particles can become

indistinguishable from the background when compared with images at higher magnifications (Fig. B.1 right).

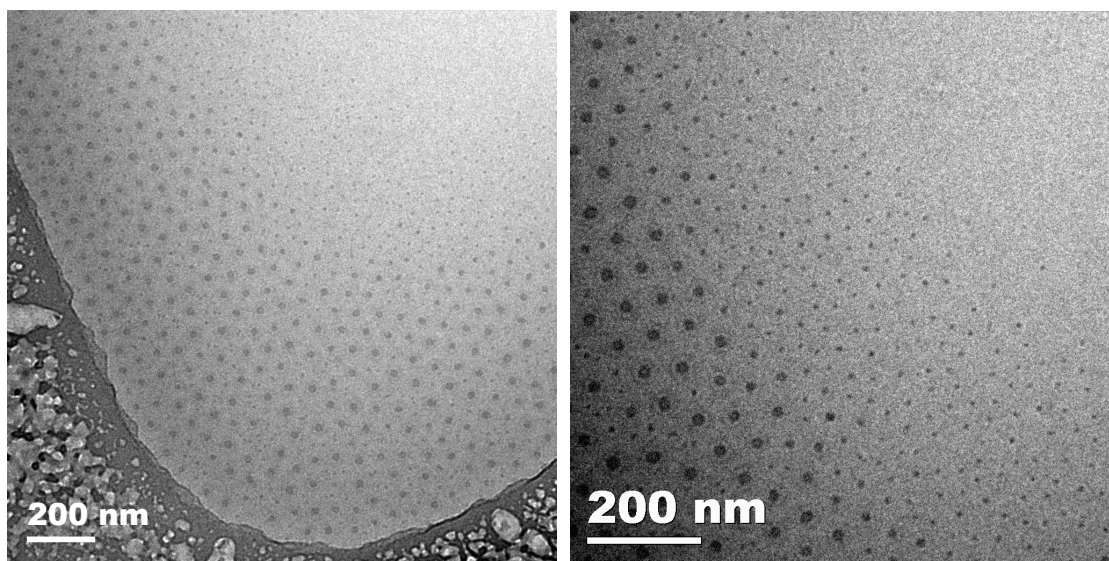


Figure B.1. Ice thickness and particle size gradients. Images at lower magnification (left) and higher magnification (right) of  $B_{59}O_{180}$  in water 4 d after dialysis (40 wt% THF,  $10 \text{ mg mL}^{-1}$  prior to dialysis into water).

One method to address the size gradient problem at higher magnification is to overlay a series of images. Figure B.2 shows a series of overlaid images taken at higher magnification. This route provides better resolution, combines data over a larger area, and captures the full particle gradient but takes additional time and effort to collect and overlay the sequence of images.

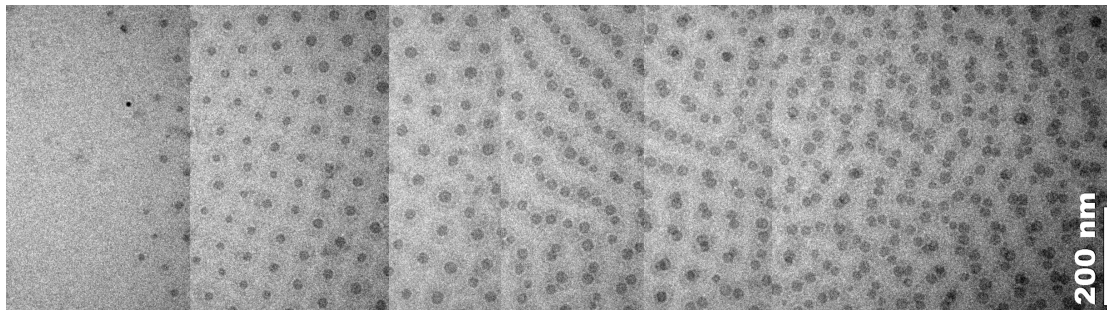


Figure B.2. Images overlaid at higher magnification. Images were cropped and overlaid for  $B_{59}O_{180}$  in water 7 d after dialysis (40 wt% THF and  $10 \text{ mg mL}^{-1}$  prior to dialysis into water).

Another challenging issue is that micelles of a select size can stack on top of the grid, likely due to capillary flow from gradients in the evaporation rate prior to vitrification. Figure B.3 demonstrates this problem with a cluster of larger micelles residing on top of the grid. Meanwhile, the grid opening shows a nearly monodispersed population of smaller micelles. Artifacts shown in Figure B.3 can effectively skew the apparent size distribution, even if the coordinates are chosen randomly.

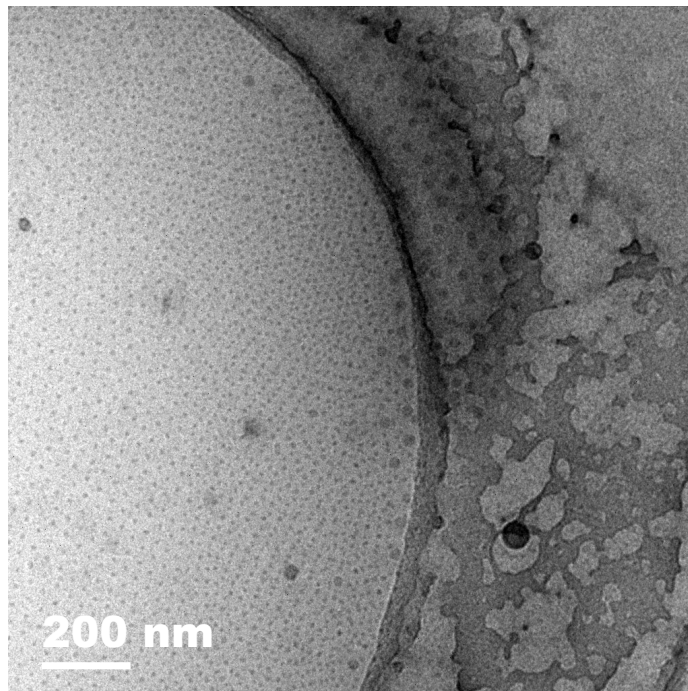


Figure B.3. Micelles clustering on top of TEM grid. Image of  $B_{81}O_{182}$  in water 2 d after dialysis (40 wt% THF and  $10 \text{ mg mL}^{-1}$  prior to dialysis into water).

## B.2 Particle Packing and Alignment

Thin layers of vitrified sample at higher micelle concentrations can lead to intriguing particle packing and alignment. Figure B.4 demonstrates the hexagonal packing produced by PB-PEO micelles trapped within a thin layer of solution prior to vitrification. The hydrophobic PB cores (darker circles) are stabilized and repelled by the surrounding PEO coronas (not visible from background contrast). If the micelles are given sufficient time to diffuse, rearrange, and relax within the thin liquid film prior to vitrification, the hexagonal packing can extend over longer length scales, as demonstrated in Figure B.4 (left). Near the edges of the grid where the ice is thicker, multiple layers of hexagonal packed micelles can be found (Figure B.5). In certain

cases, the hexagonal spacing between the packed micelles can vary, as demonstrated in Figure B.6. The two micelle layers have center-to-center distances in a 5:6 ratio.

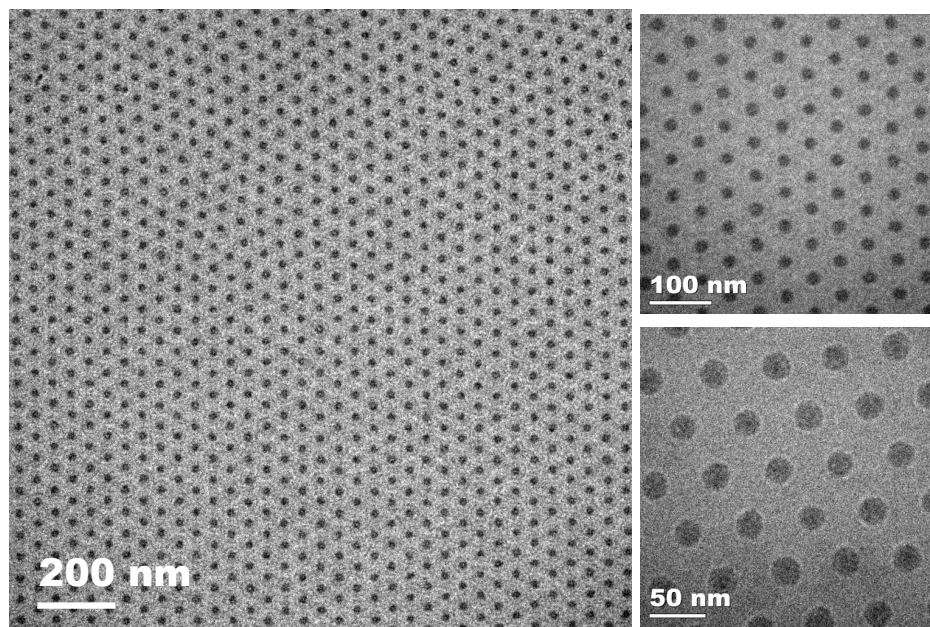


Figure B.4. Single layer of hexagonal packed  $B_{59}O_{180}$  micelles 16 d after dialysis (40 wt% THF and  $10 \text{ mg mL}^{-1}$  prior to dialysis into water).

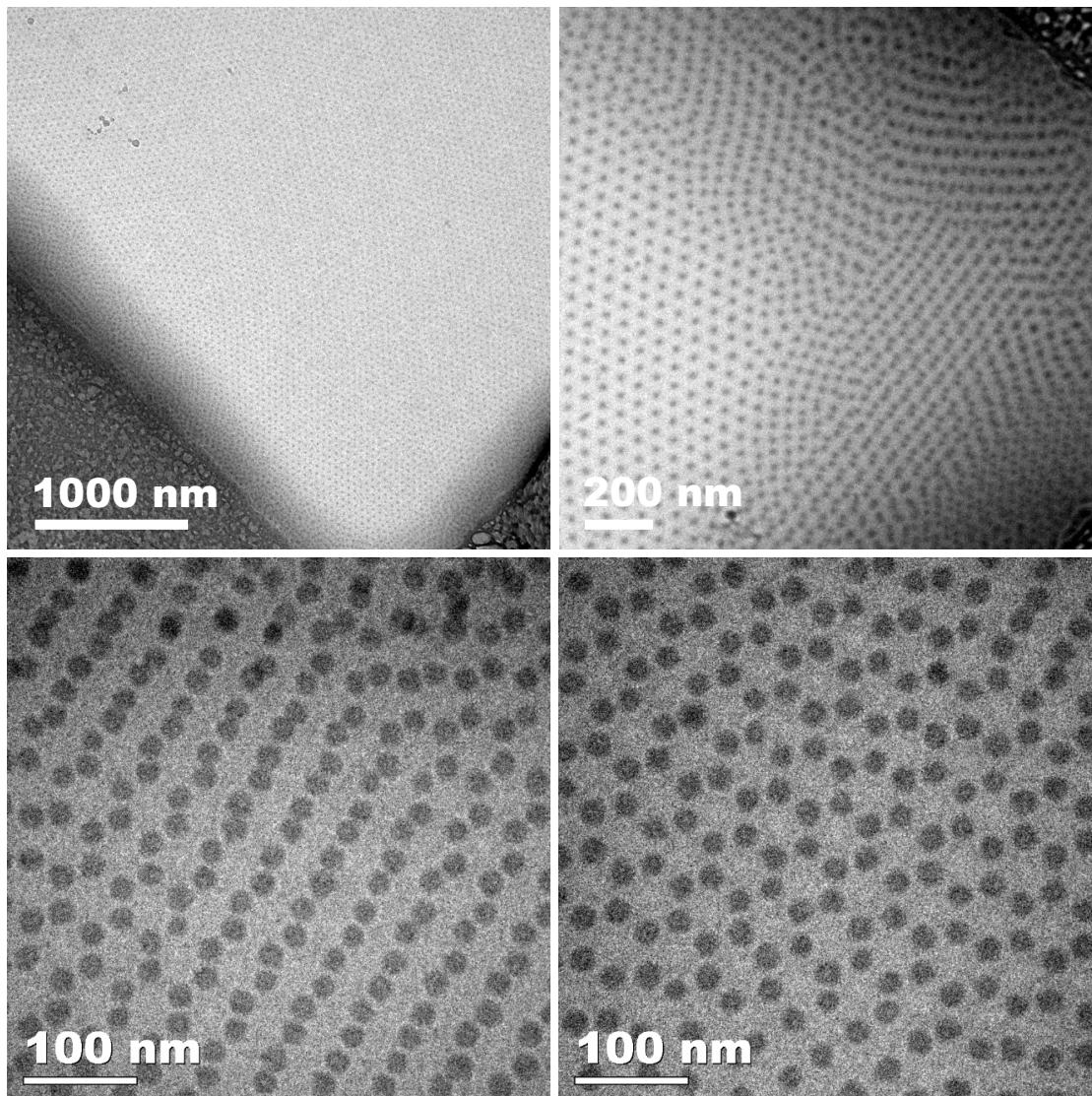


Figure B.5. Multiple layers of hexagonal packed  $B_{59}O_{180}$  micelles can occur near the grid edges with thicker ice (16 d after dialysis; 40 wt% THF and 10 mg  $mL^{-1}$  prior to dialysis into water).

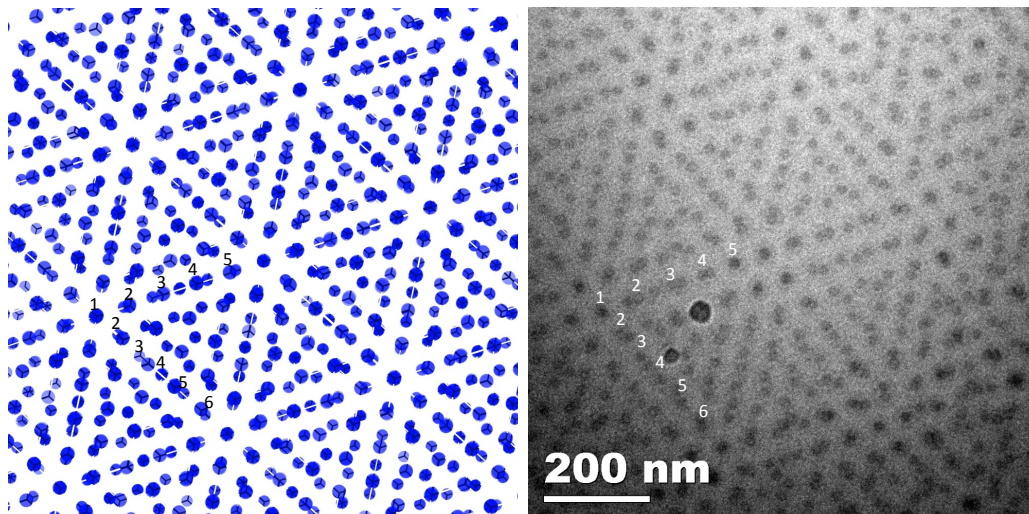


Figure B.6. Two layers of hexagonal packed micelles with spacing offset by 5:6 shown schematically (left) and in a real image (right).  $B_{59}O_{180}$  micelles 16 d after dialysis (40 wt% THF and  $10 \text{ mg mL}^{-1}$  prior to dialysis into water).

### B.3 Sample Contamination

During the vitrification process, the grid transfer process, and the sample probe transfer process, the TEM grid holding the vitrified solution will be exposed to contamination from liquid ethane, liquid nitrogen, and air, respectively. An example of this sample contamination is shown as the darker gray particles seen in Figure B.7. These irregular-shaped particles are either adhered solid ethane from exposure to liquid ethane (during the vitrification process), or they are adhered water-ice particles from exposure to air or liquid nitrogen (during the grid transfer and storage process). In normal preparation environments, some degree of particle contamination is unavoidable. However, contamination can be minimized during sample preparation by limiting the exposure of the vitrified sample to the surrounding air, liquid nitrogen, and liquid ethane. Grid locations in close proximity to major contaminated regions

(Figure B.7) are likely to be ruined, so it is best to check a new grid location or examine an entirely different grid.

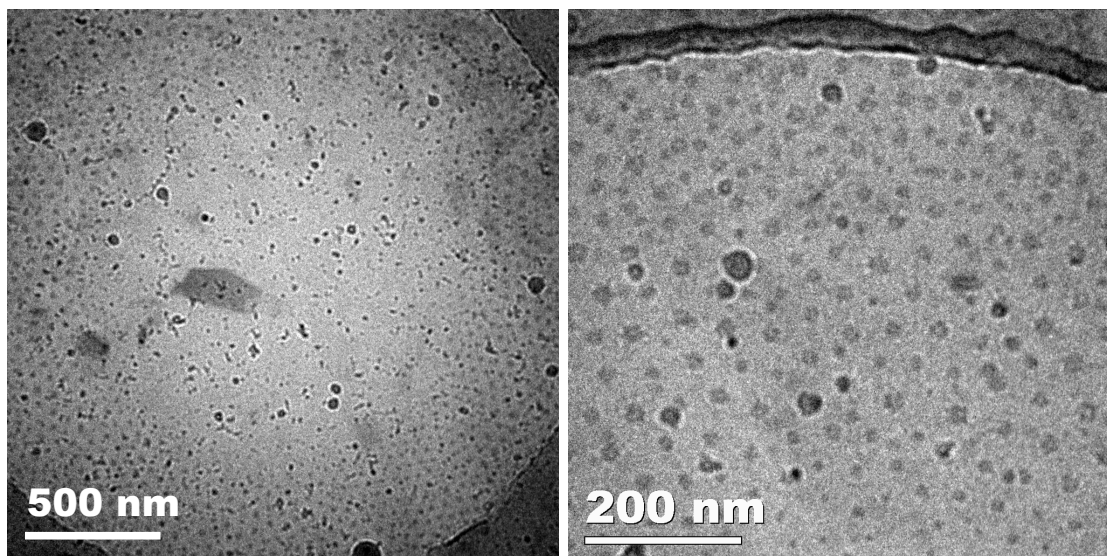


Figure B.7. Sample contamination (darker gray, irregular-shaped particles) on a TEM grid containing vitrified  $B_{59}O_{180}$  micelles 16 d after dialysis (40 wt% THF and  $2.4 \text{ mg mL}^{-1}$  prior to dialysis into water).

#### B.4 Sample and Background Degradation

Despite the very cold probe ( $-180 \text{ }^{\circ}\text{C}$  to  $-176 \text{ }^{\circ}\text{C}$ ), the sample will degrade and the vitrified background will sublime as the electron beam interacts with the sample. The effects of the electron beam and ice sublimation on PB-PEO micelles can be seen in Figure B.8. After prolonged exposure to the beam, the micelles deform in shape and begin to rupture (white spots around the dark PB core). For these particular PB-PEO micelles, there is an approximate time window of around 15-45 min (depending on the electron beam intensity) before the sample is noticeably ruined, as shown in Figure B.8 (a-c). In rare cases, large dark lines will rapidly ripple across as

waves, demonstrating significant sublimation of the amorphous water-ice background (Figure B.8d). For high resolution images of more delicate and smaller structures (e.g. protein or virus particles), the time limit before noticeable sample degradation will be significantly shorter.

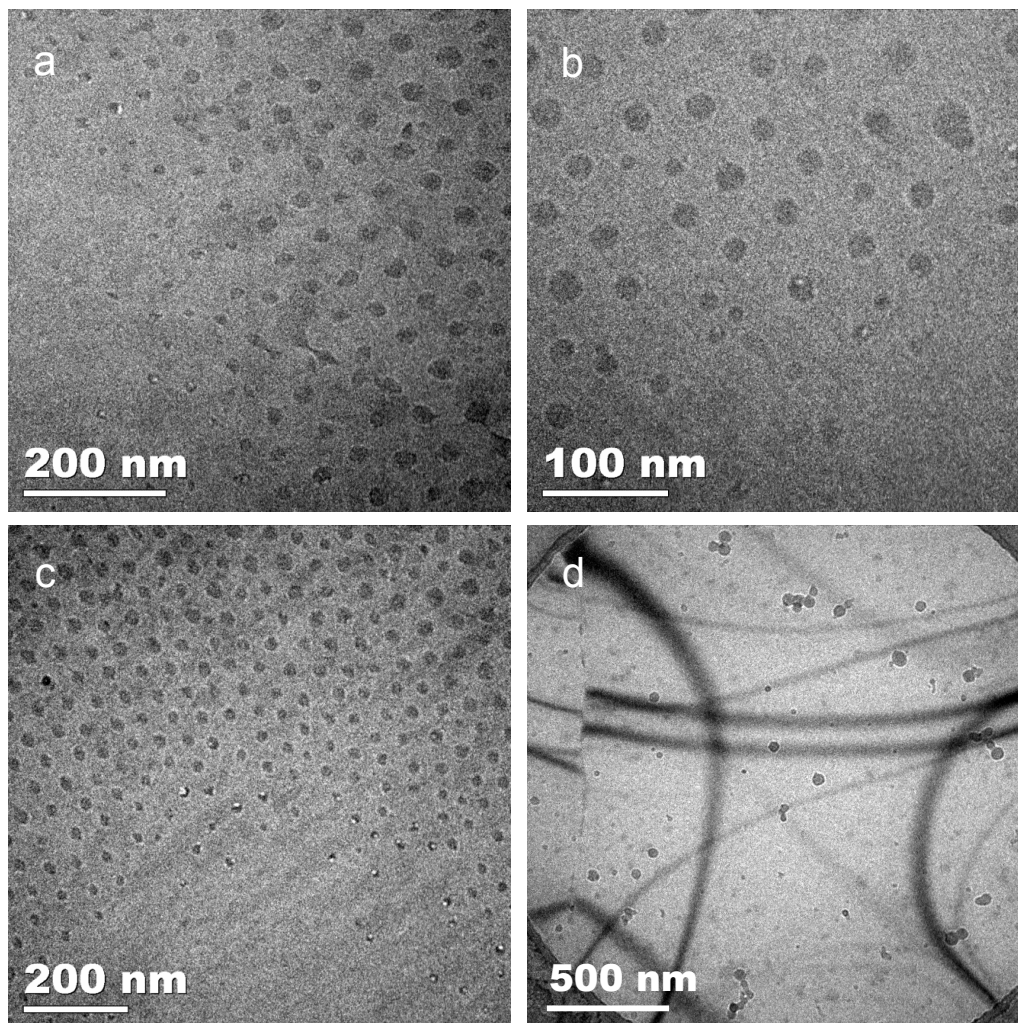


Figure B.8. (a-c) Sample degradation due to interactions with the electron beam and ice sublimation. (d) In rare cases, large black ripples appeared after rapid sublimation of the background ice. Sample solutions consisted of B<sub>59</sub>O<sub>180</sub> micelles 16 d after dialysis (40 wt% THF and 2.4 mg mL<sup>-1</sup> prior to dialysis into water).

## B.5 Blotting Effects

The blotting mechanism built into the FEI Vitrobot can occasionally supply enough force to transform the size or structure of the solution assembly (even at the lowest blot offset or blot force setting). Figure B.9 shows the presence of very large cylinder or lamellar structures within a well-characterized spherical micelle solution. It was assumed that the force of the blotting paper caused the structural rearrangement of spherical micelles into cylinders or lamellae; however, this was a rare occurrence for this sample. In general, blotting effects are more detrimental to vesicle structures that are prone to rupturing from mechanical stimuli.

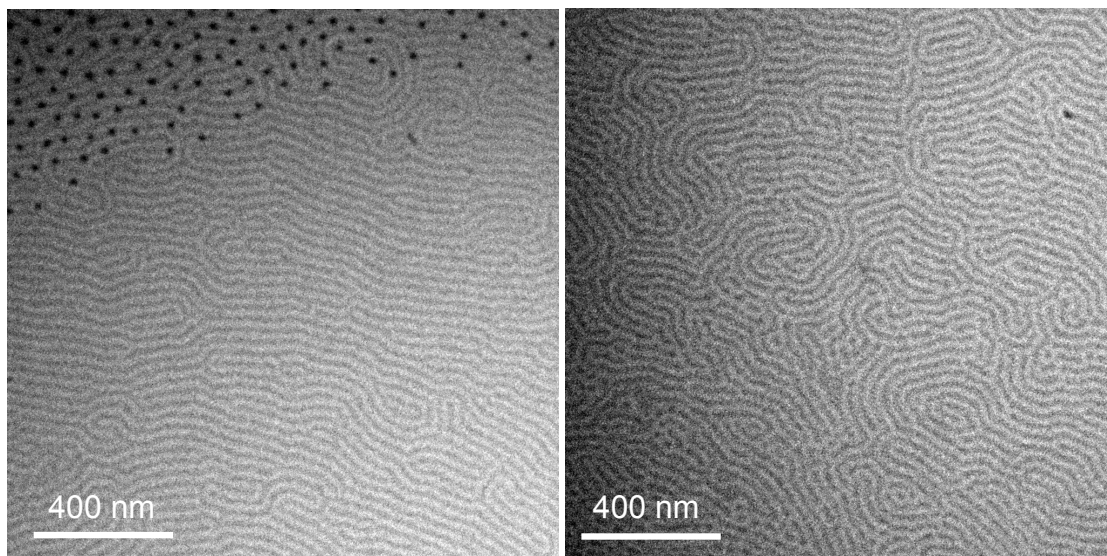


Figure B.9. Blotting effects likely caused the transition of spherical micelles into cylinder or lamellar structures (rare occurrence for this particular sample). Sample solutions consisted B<sub>59</sub>O<sub>180</sub> 10 d after dialysis (40 wt% THF and 10 mg mL<sup>-1</sup> prior to dialysis into water).

## Appendix C

### PERMISSION STATEMENTS

7/26/2014 Rightslink® by Copyright Clearance Center

Copyright Clearance Center **RightsLink®** Home Account Info Help Live Chat

ACS Publications **Title:** Structural Characterization of Amphiphilic Homopolymer Micelles Using Light Scattering, SANS, and Cryo-TEM **Logged in as:** Ryan Murphy **LOGOUT**

**Author:** Joseph P. Patterson, Elizabeth G. Kelley, Ryan P. Murphy, Adam O. Moughton, Mathew P. Robin, Annhelen Lu, Olivier Colombani, Christophe Chassenieux, David Cheung, Millicent O. Sullivan, Thomas H. Epps, III, and Rachel K. O'Reilly

**Publication:** Macromolecules  
**Publisher:** American Chemical Society  
**Date:** Aug 1, 2013  
Copyright © 2013, American Chemical Society

**PERMISSION/LICENSE IS GRANTED FOR YOUR ORDER AT NO CHARGE**

This type of permission/license, instead of the standard Terms & Conditions, is sent to you because no fee is being charged for your order. Please note the following:

- Permission is granted for your request in both print and electronic formats, and translations.
- If figures and/or tables were requested, they may be adapted or used in part.
- Please print this page for your records and send a copy of it to your publisher/graduate school.
- Appropriate credit for the requested material should be given as follows: "Reprinted (adapted) with permission from (COMPLETE REFERENCE CITATION). Copyright (YEAR) American Chemical Society." Insert appropriate information in place of the capitalized words.
- One-time permission is granted only for the use specified in your request. No additional uses are granted (such as derivative works or other editions). For any other uses, please submit a new request.

**BACK** **CLOSE WINDOW**

Copyright © 2014 Copyright Clearance Center, Inc. All Rights Reserved. [Privacy statement](#).  
Comments? We would like to hear from you. E-mail us at [customercare@copyright.com](mailto:customercare@copyright.com)

https://s100.copyright.com/AppDispatchServlet

1/1

Figure C.1. Permission statement for *Macromolecules*, 46, 6319-6325 (2013).



# RightsLink®

[Home](#)
[Account Info](#)
[Help](#)


**Title:** Size evolution of highly amphiphilic macromolecular solution assemblies via a distinct bimodal pathway

Logged in as:  
Ryan Murphy

[LOGOUT](#)

**Author:** Elizabeth G. Kelley, Ryan P. Murphy, Jonathan E. Seppala, Thomas P. Smart, Sarah D. Hann, Millicent O. Sullivan

**Publication:** Nature Communications

**Publisher:** Nature Publishing Group

**Date:** Apr 7, 2014

Copyright © 2014, Rights Managed by Nature Publishing Group

### Author Request

If you are the author of this content (or his/her designated agent) please read the following. If you are not the author of this content, please click the Back button and select an alternative [Requestor Type](#) to obtain a quick price or to place an order.

Ownership of copyright in the article remains with the Authors, and provided that, when reproducing the Contribution or extracts from it, the Authors acknowledge first and reference publication in the Journal, the Authors retain the following non-exclusive rights:

- a) To reproduce the Contribution in whole or in part in any printed volume (book or thesis) of which they are the author(s).
- b) They and any academic institution where they work at the time may reproduce the Contribution for the purpose of course teaching.
- c) To reuse figures or tables created by them and contained in the Contribution in other works created by them.
- d) To post a copy of the Contribution as accepted for publication after peer review (in Word or Text format) on the Author's own web site, or the Author's institutional repository, or the Author's funding body's archive, six months after publication of the printed or online edition of the Journal, provided that they also link to the Journal article on NPG's web site (eg through the DOI).

NPG encourages the self-archiving of the accepted version of your manuscript in your funding agency's or institution's repository, six months after publication. This policy complements the recently announced policies of the US National Institutes of Health, Wellcome Trust and other research funding bodies around the world. NPG recognises the efforts of funding bodies to increase access to the research they fund, and we strongly encourage authors to participate in such efforts.

Authors wishing to use the published version of their article for promotional use or on a web site must request in the normal way.

If you require further assistance please read NPG's online [author reuse guidelines](#).

For full paper portion: Authors of original research papers published by NPG are encouraged to submit the author's version of the accepted, peer-reviewed manuscript to their relevant funding body's archive, for release six months after publication. In addition, authors are encouraged to archive their version of the manuscript in their institution's repositories (as well as their personal Web sites), also six months after original publication.

v2.0

<https://s100.copyright.com/AppDispatchServlet#formTop>

1/2

Figure C.2. Permission statement for *Nature Communications*, 5, 3599 (2014).